

NASA CR-151922

CONTRACTOR REPORT

NAS 2-9215

JANUARY 1977

**LOW SPEED TESTS OF A FIXED  
GEOMETRY INLET FOR A TILT  
NACELLE V/STOL AIRPLANE**

(NASA-CR-151922) LOW SPEED TESTS OF A FIXED  
GEOMETRY INLET FOR A TILT NACELLE V/STOL  
AIRPLANE (Boeing Co., Seattle, Wash.) . 81 p  
HC A05/MF A01

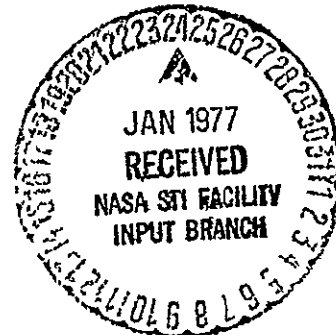
CSSL 01C

N77-18138

Unclas

G3/05 59675

By J Syberg and J L Koncsek  
Boeing Military Airplane Development  
Seattle, Washington 98124



1 Report No NASA CR-151922		2 Government Accession No		3 Recipient's Catalog No	
4 Title and Subtitle Low Speed Tests of a Fixed Geometry Inlet for a Tilt Nacelle V/STOL Airplane		5 Report Date Jan 1977			
		6 Performing Organization Code			
7 Author(s) J. Syberg and J. L. Koncsek		8 Performing Organization Report No D180-20276-1			
9 Performing Organization Name and Address  Boeing Military Airplane Development Seattle, WA 98124		10 Work Unit No			
		11 Contract or Grant No NAS 2-9215			
12 Sponsoring Agency Name and Address  National Aeronautical and Space Administration Washington D.C. Zip 20546		13 Type of Report and Period Covered Contractor Report			
		14 Sponsoring Agency Code			
15 Supplementary Notes					
16 Abstract  An experimental program was undertaken to develop an inlet for a tilt nacelle lift/cruise fan. The program was designed to support the proposed NASA/Navy V/STOL research technology airplane development. Test data were obtained with a 1/4 scale cold flow model of the inlet at freestream velocities from 0 to 77 m/s (150 knots) and angles of attack from 45° to 120°. A large scale model was tested with a high bypass ratio turbofan in the NASA/ARC 40 by 80-ft wind tunnel. The large scale test was cut short by mechanical failures. The limited amount of test results obtained prior to the failure indicates that a fixed geometry inlet is a viable concept for a tilt nacelle V/STOL application. Comparison of data obtained with the two models indicates that flow separation at high angles of attack and low airflow rates is strongly sensitive to Reynolds number and that the large scale model has a significantly improved range of separation-free operation.					
17 Key Words (Suggested by Author(s))  V/STOL Inlet                      Separation Boundary Layer                  Tilt Nacelle Angle of Attack			18 Distribution Statement		
19 Security Classif (of this report) Unclassified		20 Security Classif (of this page) Unclassified		21 No of Pages	
				22 Price*	

## CONTENTS

	Page
SUMMARY	1
INTRODUCTION	1-2
SYMBOLS AND ABBREVIATIONS	2-4
PROGRAM SCOPE AND OBJECTIVES	4-5
INLET DESIGN	6-8
TEST APPARATUS	8
Small Scale Model	8-9
Model Description and Instrumentation	8
Test Facility	8-9
Large Scale Model	9-14
Model Description	9
Instrumentation	10-11
Test Facilities	11
Data Reduction	12-14
Small Scale Model	12
Large Scale Model	12-14
TEST RESULTS	14-22
Small Scale Inlet Model	14-16
Static Test, Large Scale Model	16-17
Wind Tunnel Test, Large Scale Model	18-22
Inlet Performance and Separation Boundaries	18-20
Fan and Engine Operating Characteristics	20-21
Nacelle Forces	21-22
CONCLUDING REMARKS	22
REFERENCES	23

## LIST OF TABLES

	Page
1. Design Conditions	24
2 Force Data	25

## LIST OF FIGURES

	Page
1. V/STOL Inlet Low Speed Design Points	26
2. Effects of Flow Separation on Inlet Performance	27
3. LCF Inlet Model Schematic	28
4. Windward Cowl Wall Curvature	29
5. Cowl Lip Thickness Variation	30
6. Small Scale Model Fan Face Rake	31
7. Small Scale Inlet Model Installed in 9 by 9-ft Wind Tunnel	32
8. Nacelle Schematic	33
9. Nacelle Photograph	34
10. LCF Inlet Cowl Contours	35
11. Cowl Static Pressure Instrumentation	36
12. Fan Face Instrumentation	37
13. Fan Duct Instrumentation	38
14. Compressor Face Rake	39
15. Primary Nozzle Instrumentation	40
16. Temperature and Vibration Monitoring Locations	41
17. Static Test Installation (Photo)	42
18. Static Test Installation Schematic	43
19. Nacelle Installed in 40-by 80-ft Wind Tunnel (Photo)	44
20. Wind Tunnel Installation Schematic	45
21. Data Acquisition and Reduction System Diagram	46
22. 1/4 Scale LCF Inlet Test Matrix	47
23. Separation Boundaries for the 1/4 Scale LCF and QF2 Inlets	48
24. 1/4 Scale LCF Inlet Flow Calibration	49
25. 1/4 Scale LCF Inlet Recovery	50
26. 1/4 Scale LCF Inlet Distortion	51
27. 1/4 Scale Inlet Fan Face Total Pressure Maps, $\alpha = 45^\circ$ , $V_o = 72$ m/s	52
28. 1/4 Scale Inlet Fan Face Total Pressure Maps, $\alpha = 60^\circ$ , $V_o = 64$ m/s	53
29. 1/4 Scale Inlet Fan Face Total Pressure Maps, $\alpha = 75^\circ$ , $V_o = 54$ m/s	54
30. 1/4 Scale Inlet Fan Face Total Pressure Maps, $\alpha = 120^\circ$ , $V_o = 21$ m/s	55

	Page
31. Test Matrix for Static Testing	56
32. Inlet Airflow vs Turbine Speed and Fan Blade Angle	57
33. Comparison of Inlet Airflow Measurement Methods	58
34. Comparison of Cowl Static Pressure Distributions	59
35. Fan Thrust vs Engine Power with Ground Plane	60
36. Design and Test Conditions	61
37. LCF Inlet Performance, $V_0 = 21$ m/s	62
38. LCF Inlet Performance, $V_0 = 39$ m/s	63
39. Separation Boundaries for Small Scale Inlet	64
40. Empirical Separation Index	65
41. Experimental Separation Boundaries for Small Scale Inlet and Predicted Separation Boundaries using $\theta = 18.2^\circ$	66
42. Predicted Separation Boundaries for Large Scale Inlet, $\theta = 22.4^\circ$	67
43. Large Scale Inlet Separation Boundaries and Design Conditions	68
44. Experimental and Analytically Predicted Separation Points for Small and Large Scale Inlets	69
45. Comparison of Experimental Static Pressure Profiles and Computed Hi Profiles	70
46. Core Engine Compressor Face Performance	71
47. Fan Nozzle Total Pressure Profiles, $V_0 = 21$ m/s, $\alpha = 0^\circ$ and $90^\circ$	72
48. Fan Nozzle Total Pressure Profiles, $V_0 = 39$ m/s, $\alpha = 60^\circ$	73
49. Engine Torque vs Power Lever Angle	74
50. Nacelle Pitching Moment	75

## SUMMARY

A small scale model of an inlet designed for a Lift/Cruise - Fan propulsion system was tested in the Boeing 9-by 9-ft Low Speed Wind Tunnel. Inlet performance data were obtained at freestream velocities of 0 to 77 m/s (150 knots), angles of attack of  $45^{\circ}$  to  $120^{\circ}$ , and inlet airflow rates of  $73 \text{ kg/sm}^2$  ( $15 \text{ lb/sec ft}^2$ ) to  $210 \text{ kg/sm}^2$  ( $43 \text{ lb/sec ft}^2$ ). This test provided data on inlet flow separation and performance characteristics and defined an accurate airflow calibration for determining the flow rates in the subsequent large scale tests.

Static testing of the large scale nacelle was conducted at the Boeing engine test site near Tulalip, Washington. During the test all systems required for the wind tunnel test were operated and checked out. Static performance of the fan/engine system, with the LCF inlet and an extended fan nozzle installed, was in agreement with static performance previously obtained by Hamilton-Standard. A ground plane positioned as close as .9 m (3 ft) from the core nozzle exit plane was used to simulate vertical take-off and landing. No adverse effects on fan or engine performance were observed with the ground plane.

Testing of the large scale nacelle in the NASA-ARC 40-by 80-ft Wind Tunnel was only partially completed. The test was prematurely terminated due to a mechanical failure. Wind-on data were obtained at 21 m/s (40 knots) up to  $90^{\circ}$  angle of attack and at 39 m/s (75 knots) up to  $60^{\circ}$ . These data indicate a significant improvement in separation free operating range of the large scale inlet as compared to the small scale model. Analysis of the data indicates that the improvement observed on the large scale model can be accounted for by the favorable effect of the increased Reynolds number.

## INTRODUCTION

The development of V/STOL airplanes for both civilian and military applications requires propulsion data in technology areas where relatively little experimental work has been done to date. An asymmetric inlet design for a tilt-nacelle lift/cruise fan (LCF) propulsion system was developed by The Boeing Company to be tested in an experimental program funded by NASA-Ames Research Center under contract NAS2-9215. The objectives of the program were to determine the range of nacelle tilt angles, freestream velocities, and engine airflow ranges for which a fixed lip inlet can provide pressure recoveries and distortion levels that result in acceptable engine core/fan operating characteristics (stall tolerance) and fan blade stress levels.

A small scale (approximately 1/4 scale) inlet model was designed based on the results of internal research and development work conducted at Boeing. As part of the present contract, this small scale model was tested in the Boeing Company's 9- by 9-ft Low Speed Wind Tunnel. The results of the test were used to develop inlet flow rate calibrations, and to establish inlet performance characteristics at flow rates above the limits of the large scale installation described below.

A large scale (approximately 0.9 scale) model of the inlet for the proposed NASA/Navy V/STOL research technology airplane was fabricated to fit the existing Hamilton-Standard variable pitch Q-Fan. The fan has a 1.4 m (55 in) tip diameter and is driven by a Lycoming T-55-11A turbo-shaft engine. Appropriate cowlings, fairings, etc. were designed and fabricated to develop a nacelle suitable for wind tunnel testing. The complete nacelle was tested statically at the Boeing engine test site located near Tulalip, Washington. During the static test all systems and instrumentation required for wind tunnel testing were operated and checked out.

Following the static test the nacelle, the external fuel and oil systems, the model data system, and the computer used for data reduction were shipped to NASA Ames Research Center. Testing was conducted in the 40- by 80-ft Wind Tunnel. The planned test program was not completed due to a mechanical failure which resulted in partial destruction of the T-55 core engine and the Q-Fan gearbox. This incident is discussed in reference 1. The present report deals with the aerodynamic performance of the inlet/fan/engine installation based on the small scale results and the limited amount of data obtained in the large scale wind tunnel test.

#### SYMBOLS AND ABBREVIATIONS

A	Flow area
$A_{\text{FAN}}$	Fan face area = $1.206 \text{ m}^2$ ( $12.98 \text{ ft}^2$ )
AR	Flow area at fan nozzle rake = $1.064 \text{ m}^2$ ( $11.45 \text{ ft}^2$ )
$D_H$	Hilite diameter
DISC	Max-min total pressure differential at compressor face divided by average total pressure
DISF	Max-min total pressure differential at fan face divided by average total pressure
ET	Engine torque
$F_R$	Inlet ram drag



$F_X$	Force measured in tunnel streamwise direction
$F_Y$	Nacelle lift force measured in the tunnel horizontal plane perpendicular to the streamwise direction
$H$	Moment arm, $M_p/F_R$
$H_1$	Boundary layer shape factor
KN2	Power turbine corrected speed (rpm)
LCF	Lift/Cruise - Fan
$M_p$	Nacelle pitching moment referenced to intersection of engine centerline and hilite plane
$M_Z$	Nacelle pitching moment referenced to nacelle pivot point
N2	Power turbine speed (rpm)
$P_C, P_S$	Static pressure
$P_T$	Total pressure
$P_{To}$	Free stream total pressure
PCP	Prandtl static pressure on fan face rake
PLA	Power level angle
PM	Prandtl static pressure on fan nozzle rake
PTF	Total pressure on fan face rake
PTCA	Area weighted average total pressure at compressor face
PTFA	Area weighted average total pressure at fan face
PTM	Total pressure on fan nozzle rake
QF2	Axisymmetric inlet model tested previously
$R$	Radius
$R_C$	Radius of curvature
$R_{FAN}$	Fan tip radius = 0.699 m (27.5 in)

$R_H$	Hilite radius
$R_{MIN}$	Minimum distance from cowl to engine centerline in a given circumferential position
$S$	Surface distance along cowl wall measured from hilite
$T_T$	Total temperature
$TTM$	Total temperature on fan nozzle rake
$V_o$	Tunnel velocity
$V_o/V_H$	Inlet velocity ratio based on hilite area
$W1$	Fan face airflow calculated from WK1A
$W2$	Fan face airflow calculated from fan face rake total and static pressure measurements
$W3$	Sum of fan nozzle airflow calculated from fan nozzle rake data and core engine airflow calculated from compressor face rake data
$WK1A$	Fan face corrected airflow divided by fan face area, based on small scale model airflow calibration curve
$X$	Distance between core nozzle and ground plane
$\alpha$	Inlet angle of attack
$\beta$	Fan blade angle
$\theta$	Circumferential position
$\phi$	Empirical separation index
$+\Delta W$	Increasing inlet airflow
$-\Delta W$	Decreasing inlet airflow

#### PROGRAM SCOPE AND OBJECTIVES

On a tilting nacelle V/STOL airplane the inlet is exposed to much more demanding operating conditions at low speeds than on a conventional subsonic airplane. The combinations of freestream velocity and angle of attack are particularly severe during the landing transient as illustrated in figure 1. The main function of the inlet is to supply flow with low total pressure

distortion and high recovery to the fan since nacelle drag is generally not a major factor during these low speed maneuvers.

The primary source of distortion (localized total pressure loss) in a subsonic inlet is flow separation. At high airflow rates (near choking conditions) local pockets of supersonic flow tend to develop on the inlet cowl. Total pressure is lost when the flow, through shocks, decelerates to subsonic speeds. More importantly, when the shock waves, or adverse pressure gradients, become sufficiently strong (in the absence of boundary layer control) the flow separates away from the cowl leading to increases in distortion and reductions in recovery. We shall refer to this flow phenomenon as a "+ $\Delta W$  separation," since for a given freestream velocity and angle of attack it occurs as the airflow increases beyond a limiting value. When the inlet is separated in the + $\Delta W$  mode the distortion increases rapidly with increasing airflow.

For the present program another type of separation, which we shall call a "- $\Delta W$  separation" is more significant. At a given freestream velocity and angle of attack the - $\Delta W$  separation occurs when the airflow is decreased below a limiting value. This seems to be contradictory to the fact that the adverse pressure gradients in the inlet decrease with decreasing airflow. However, the local boundary layer Reynolds number is also decreasing with decreasing airflow making the boundary layer more sensitive to an adverse pressure gradient. Apparently, the adverse change in Reynolds number can, under certain free stream conditions, dominate the favorable change in pressure gradient such that the inlet boundary layer eventually separates. This hypothesis has been supported by boundary layer analysis of experimental surface pressure gradients for various inlet airflows.

The effects of the two types of separation on inlet performance are shown schematically in figure 2. One measure often used as an indicator of the severity of separation is distortion. It is most simply defined as the difference between the maximum and minimum total pressures at the fan face divided by the average total pressure at the same station. When separated flow is present at the fan face, the minimum total pressure is approximately equal to the local static pressure. Low airflow rates imply a small difference between the total and static pressures. Thus for a - $\Delta W$  separation the distortion tends to be relatively low. It follows that if the separation can be restricted to very low airflow rates, the fan performance may not be significantly degraded and the blade stresses may be acceptable while operating with separated flow in the inlet since the distortion will be low.

As stated in the Introduction, the objectives of the program were to determine the limits of operating conditions where a fixed lip inlet can provide recoveries and distortion levels that are compatible with fan and core engine operating characteristics. Specific goals for the present program were established from analysis of estimated mission requirements for the multipurpose NASA/Navy V/STOL airplane. The design goals were formulated as a set of operating conditions where the objectives of high recovery and low distortion were to be met. These design conditions are listed in table 1.

## INLET DESIGN

Prior to the present NASA-sponsored test program, an analytical/experimental design effort was undertaken by The Boeing Company to define a fixed-geometry inlet for the 1041-133 multi-purpose V/STOL airplane. Several axisymmetric inlet models were designed and tested to determine the inlet geometry required for good performance at the severe angle-of-attack conditions expected to be encountered during approach and landing. The results of these tests indicated that very high contraction ratios (inlet area/throat area) are needed to provide attached inlet flow throughout the operating envelope of the V/STOL airplane. High contraction ratio inlets tend to have a low critical Mach number (early drag rise) and thus limit the airplane cruise speed. In selecting the optimum inlet geometry the proper trade must be made between low speed angle-of-attack capability and cruise speed.

From the axisymmetric model tests and preliminary cruise drag analyses it became evident that completely separation-free operation throughout the low speed/high angle-of-attack design envelope could not be obtained with an inlet that had a drag rise Mach number above .75, as initially desired. One of the models tested, called QF2, appeared to provide a reasonable compromise between the conflicting design requirements, as described below

- (1) The analytically predicted drag rise point occurs between Mach .65 and .70 for the axisymmetric QF2 inlet. By designing the inlet with a reduced lip thickness on the upper part of the inlet, i.e., an asymmetric lip, it should be possible to significantly increase the drag rise Mach number. (The drag rise condition was said to occur when the drag produced by the external normal shock wave is equal to approximately 10% of the total fan cowl drag; which includes external skin friction, pressure drag, and wave drag )
- (2) The wind tunnel test results indicated that flow separation was present in the inlet only at conditions simulating low power settings (when the airplane is not thrust critical). Because of the low airflow the distortion was relatively low and was not considered to be a problem for fan operation. Another consideration was that separation would be delayed on a full scale inlet as compared to the 1/4 scale model due to the higher Reynolds number. Thus the full scale inlet was expected to have a larger range of operation with attached flow.

The design work for the present contract therefore consisted of developing an asymmetric inlet that would maintain the excellent low speed/high angle-of-attack capabilities of the QF2 inlet but would increase the potential cruise flight Mach number by reducing the overall inlet contraction ratio. This study resulted in a rather unique inlet design as described in the following paragraphs.

The LCF inlet model is shown schematically in figure 3. The lower cowl lip is rather thick as compared to the upper lip. The fundamental effect of increasing the angle-of-attack (or increasing the freestream velocity at angle-of-attack) on the inlet is to increase the pressure gradients along the windward (lower) cowl surface. In contrast the leeward (upper) cowl pressure gradients at angle-of-attack are less severe than during static operation due to the concentration of the captured flow near the windward lip. Since boundary layer separation is induced by adverse pressure gradients, the low speed design point for the leeward cowl is static operation at maximum airflow (i.e., maximum adverse gradients). The static performance of various existing inlets were reviewed to determine the geometry requirements for the upper cowl. The lip design developed from this study has a local contraction ratio  $(R_H/R_{TH})^2$  of 1.3.

At a given operating condition the cowl pressure gradients are basically determined by the wall curvature. A thick cowl is necessary on the windward side to minimize the pressure gradients by minimizing the local flow turning. The curvature distribution of the windward cowl is plotted against surface distance in figure 4. This distribution was developed for the 1/4 scale QF2 model and is the result of several iterations of the contour. The goal of the design was to keep the radius of curvature as high as possible at the hiltite and avoid sudden changes in curvature along the surface.

The LCF inlet is based on the QF2 model and incorporates the following design features

Throat area. - The need for a large contraction ratio required that the throat area be minimized. The throat was sized for a one-dimensional Mach number of .7 at maximum airflow. This value was derived from analysis of performance data from existing inlets.

Inlet length. - Computer simulations of high airflow cases with headwind were made for several axisymmetric diffuser contours. In the analysis the goal was to keep the boundary layer shape factor low, thus allowing for profile deterioration anticipated at angle-of-attack. The final inlet design has a length to diameter ratio  $(L/D_{FAN})$  of .82.

Nacelle fineness ratio. - Computer analyses of cruise cases were made using axisymmetric models to determine the maximum fineness ratio  $(D_H/D_{MAX})$  compatible with the airplane requirements. The calculations indicated that  $D_H/D_{MAX}$  should be kept below .85. This was used as the limiting value for the axisymmetric inlet. The asymmetric LCF design has a fineness ratio of .83.

The asymmetric LCF inlet was developed by blending a QF2 type lower cowl into a more conventional upper cowl. In order to facilitate fabrication and to keep close control on the contours, the cowl was designed with circular cross sections (normal to the fan centerline) at all stations.

This lofting procedure also ensures smooth wall curvature distributions in all directions along the cowl surface. The resulting lip thickness distribution is shown in figure 5. Note that at  $180^\circ$  the LCF cowl is slightly thicker than the QF2 cowl. The increased thickness was considered necessary to compensate for the asymmetry, since the goal was to at least equal the QF2 low speed performance.

Some additional features of the design are as follows. As the lip becomes thinner (going from the lower,  $180^\circ$ , contour to the upper,  $0^\circ$ , contour) the minimum cowl radius moves forward as indicated in figure 3. The result is that the diffuser wall becomes less steep along the same path. Also as the lip becomes thinner, the design of the external cowl can be developed more easily with smooth wall curvature distribution.

## TEST APPARATUS

### Small Scale Model

Model Description and Instrumentation.—The model is a .273 scale geometrically accurate representation of the large scale LCF inlet. Instrumentation for the wind tunnel test consisted of cowl surface static pressure taps, fan face total and static pressure rakes, and the inlet flow metering venturi assembly.

The  $1/4$  scale model fan face rake instrumentation is illustrated in figure 6. The rake has four arms; each arm contains 20 total pressure probes and one Prandtl static probe. At each test point data were recorded with the rake positioned as shown in figure 6, as well as with the rake rotated  $45^\circ$  from the position shown. Thus the fan face total pressure array was defined by 160 measured values.

The surface static pressure instrumentation for the small scale model is similar to the large scale inlet instrumentation and is therefore presented in connection with the description of the large scale model.

Test Facility—Testing of the  $1/4$  scale model was conducted in the Boeing 9- by 9-ft B Low Speed Wind Tunnel. The tunnel test section has the dimensions of 2.74 m by 2.74 m (9 ft. by 9 ft.), and a nominal speed range of 0 to 90 m/s (0 to 175 knots) the wind tunnel airflow is driven by a turbo-prop engine located downstream of the test section. Ambient air enters the tunnel through a bellmouth and is exhausted downstream of the turbo-prop. A turbo-jet engine is located outside the wind tunnel and is connected to the inlet model by a duct passing through the test section floor. The model airflow is varied by varying the turbo-jet power setting. The airflow rate is measured by a calibrated venturi meter installed in the duct between the model and the engine.

Model angle-of-attack variation is achieved by interchanging wedge shaped duct segments which carry the inlet flow and also act as support for the model. A typical installation is shown in figure 7. The model support system contains a remotely controlled mechanism for rotating the fan face rake assembly.

### Large Scale Model

Model Description.—The nacelle contains the asymmetric inlet, a variable pitch fan, and a turboshaft core engine as shown schematically in figure 8. Appropriate cowlings and fairings were designed and fabricated to assemble the hardware into a wind tunnel test article. Photographs of the complete nacelle are shown in figure 9.

The major dimensions of the LCF inlet are as follows

inlet diameter, $D_H$	= 1.469 m (57.826 in)
throat diameter, $D_H$	= 1.200 m (47.236 in)
fan face diameter, $D_{FF}$	= 1.397 m (55 in)
inlet length, $L_{FF}$	= 1.143 m (45.011 in)

The inlet contour coordinates are listed in figure 10. Note, that the inlet designed for the Q-Fan installation is slightly smaller than the proposed NAVY V/STOL Demonstrator inlet which has a fan tip diameter of 1.575 m (62 in.).

The Hamilton-Standard Q-Fan demonstrator is a 1.397 m (55 in), 13 bladed, variable pitch fan which utilizes a Lycoming T55-L-11A, 2800 kW (3750 hp) gas turbine as the core engine. The fan has a 17:1 bypass ratio and is driven through a 4.75:1 gear reduction to a maximum speed of 3365 rpm. Reference 2 contains further details of the Q-fan/T-55 propulsion unit.

The primary supporting structure for the nacelle is contained in the fan duct cowling. This supporting ring houses the fan exit guide vanes. The vanes in turn support the fan/engine mounting structure. The fan duct support ring also provides the structural interface for attachment of the inlet and the fan exit nozzle, and for mounting the nacelle on the wind tunnel pylon. A detailed description of the test article is given in reference 1.

Instrumentation.—The instrumentation is divided into two groups based on its primary function, namely. (1) Model performance and (2) Fan/engine operation and health. The model performance data includes all parameters that are to be recorded and processed off-line.

Inlet Instrumentation, - The inlet cowl is provided with 18 surface static pressure taps at the top ( $0^{\circ}$ ), 18 taps at the bottom ( $180^{\circ}$ ) and one tap at each side ( $90^{\circ}$  and  $270^{\circ}$ ). Seven additional surface taps are distributed circumferentially at the fan face rake station. Model coordinates for these 45 surface static taps are listed in figure 11. The locations of the static taps on the small scale model are also shown in this figure.

The fan face rake has 7 arms spaced  $51.43^{\circ}$  apart starting at  $180^{\circ}$ . Each rake arm is provided with 10 steady state total pressure probes. A Prandtl static probe is located midway between the two innermost pressure probes on each rake arm. The probe radii (referenced to the fan centerline) are listed in figure 12. The rake arm at  $180^{\circ}$  also contains 3 close coupled dynamic pressure transducers. These are mounted side by side with three of the steady state probes. The outermost dynamic probe was used to detect flow separation in the inlet, while the inner probes were used to monitor the turbulence level in and near the flow entering the core engine.

Fan Duct Instrumentation, - The fan duct contains two instrumentation rakes on diametrically opposite sides near the exit plane of the nozzle. Each rake contains 10 total pressure probes, 3 total temperature sensors, and 2 static pressure probes. The fan duct rakes are defined in figure 13.

Engine Instrumentation, - The core engine contains performance instrumentation just upstream of the compressor and in the diffusing exhaust nozzle.

The compressor face instrumentation consists of eight total pressure rakes. Each rake contains six total pressure probes and one static pressure tap. The third probe (from the outer end) on three of the rakes is a high response (Kulite) total pressure sensor. The compressor face rake is shown in figure 14. A temperature probe is located at  $180^{\circ}$  near the cowl at the same station.

The engine nozzle contains a five probe total pressure rake and a five probe total temperature rake as shown in figure 15. Four surface static pressure taps are located on the nozzle cowl.

Fan/Engine Operation and Health, - Both the fan and core engine are instrumented with various operational and health monitoring systems. In most cases, critical parameters have redundant and/or extra sensors. Continuous automatic monitoring, with preset over/under limit switches, of the critical parameters is provided to either shut the system down or give an audible or visual warning when any of these present limits are violated.

Parameters recorded on the data system to define the basic system condition are fan blade angle ( $\beta$ ), power lever angle,  $N_1$ ,  $N_2$ , TT7, torque and fan pressure ratio. Monitored instrumentation for the engine consists of fuel pressure, oil pressure, temperature, contamination, and level, EGT, RPM's, and RPM overspeed protection. The fan system also contains meters for lube oil pressure, flow and temperature, fan speed and several "chip detectors" for monitoring metallic particles in the gear box/drive system.



Fire and Safety, - In addition to the above instrumentation, the fan/engine system contains sensors to monitor temperatures and vibration levels. The temperatures are mainly to detect fire or local over-temperature operating conditions and the vibration meters to monitor structural integrity, and operation of the rotating machinery. Figure 16 shows the general locations of the various sensors. The temperature sensors were monitored on API meters (6) and the accelerometers (8) on vibration/displacement meters. Each meter is equipped with a preset upper (maximum) limit trip which will trigger an alarm system when exceeded. The extra and/or redundant temperatures were monitored on a direct reading Doric meter. To assure operation of the fan system within the structural design envelope, three of the thirteen blades have been strain gaged. The output of these gages was monitored and recorded continuously during testing. Three Kulite transducers at the engine compressor face were also continuously monitored to detect any higher-than-normal pressure fluctuations entering the core engine at certain test points.

Test Facilities—Static testing of the nacelle was conducted at the Boeing Company's engine test site located near Tulalip, Washington. Wind tunnel testing was conducted in the NASA-ARC 40-by 80-ft Wind Tunnel at Moffett Field, California.

The purpose of the static test was to provide an operational checkout of all nacelle systems and instrumentation required during the wind tunnel test, and to evaluate ground effects on the propulsion system performance. Figure 17 shows the nacelle mounted on the static test rig. A schematic of the installation, including the ground plane simulation is shown in figure 18.

Figure 19 shows the model installed in the 40- by 80-ft wind tunnel. The nacelle was mounted on a single, hollow column strut approximately 3.8 m (150 in) from the wind tunnel floor. The strut in turn was attached to the NASA floor mounted semispan model turntable. The turntable is located on the wind tunnel vertical centerline. The semispan turntable, strut and nacelle were "on balance" for measuring model forces. A large fairing or "wind shield," off balance, protected the turntable and strut surfaces from the wind tunnel aerodynamic forces.

The nacelle was yawed in the horizontal plane by means of the tunnel turntable to simulate operation at the various inlet angles of attack. The inlet top/ bottom ( $0^{\circ}/180^{\circ}$ ) plane was located on a wind tunnel horizontal plane, see figure 20.

## DATA REDUCTION

Small Scale Model.—The data acquisition and reduction system used for the small scale model in the Boeing 9- by 9-ft tunnel has been developed through numerous test programs. On-line data is available from several X-Y plotters and digital volt meters located near the test operator's desk. For this test a close-coupled high response transducer mounted on the fan face rake was displayed on a X-Y plotter against tunnel speed to accurately define the point of inlet separation.

Off-line data is processed on a PDP8-E computer located in the tunnel control room. Off-line data is thus available within minutes of a test run. The basic computer program, which calculates the standard inlet parameters, was modified to provide special calculations for this program. These included various calculations of the throat static pressures to help define a suitable airflow calibration parameter as well as the special inlet recovery PTFA described below.

The small and large scale models used different fan face instrumentation (see figures 6 and 12). On the small scale model the fan face total pressure array was defined by 160 measured values compared to 70 on the large scale inlet. To provide a better base for direct comparison of the two inlets a special inlet recovery calculation was made for the small scale inlet. This calculation, which was used for the test results presented in this report, is based on 80 measurements using probes located close to the radial locations of the large scale probes. It should be noted that the difference in recovery between the "all-probes" calculation and the "selected-probes" calculation in most cases is less than  $0.001 P_{T0}$ .

Large Scale Model.—The data acquisition and reduction system used in the 40- by 80-ft wind tunnel is diagrammed in figure 21. With the exception of items relating to the wind tunnel, the identical system was used in the static test at Tulalip.

On-line data, - Certain parameters were displayed on-line to monitor nacelle performance and engine "health." Some of these are described below.

Three X-Y plotters were used to detect flow separation in the inlet. One plotter had the average of 4 static pressures near the inlet throat (PAV) as the abscissa and the root mean square (RMS) average of the outermost fan face dynamic pressure (PDF1) as the ordinate. The inlet corrected airflow rate had been calibrated against PAV in the small scale test, and the location of PDF1 had been selected to provide a positive indication of flow separation in the inlet. This plotter could be used to make an accurate determination of the airflow rate where separation occurred for a given angle of attack and freestream velocity.

Another plotter had the same RMS as the ordinate and the model angle of attack as the abscissa. This was to be used for defining the separation angle-of-attack at constant freestream velocity and inlet airflow. A third plotter was connected to a special scan-valve which could be stepped from the control console to construct a total pressure profile of the windward ( $180^\circ$ ) fan face rake.

The instantaneous pressures from all six dynamic pressure transducers (including PDF1) were displayed on individual cathode ray tubes. These signals were also processed on-line by RMS meters.

Various fan and engine parameters were recorded on tape. These included fan blade stress levels, fan blade angle, engine torque, and power turbine speed (N2), see reference 1.

Off-line Data, - The engine operating parameters and data from the instrumentation shown in figures 11 through 15 were recorded on punched paper tape by the Boeing Standard Digital Data System (SDDS), see figure 21. The wind tunnel parameters and force balance readings were also recorded on paper tape by the Wind Tunnel Data Systems. All data stored on paper tape were processed with an on-site PDP8 computer assigned to the present test. Thus turn-around time was less than one hour for off-line tabulated data and for selected machine plots of the data.

When testing a complete nacelle it is difficult to measure the inlet airflow accurately. To obtain a reliable reading, the airflow was calculated by three independent methods. The first of these was based on calibration of the small scale model. This is considered to be the most accurate method of measuring the airflow. However, it is not valid when large separations are present in the inlet. For the second method of calculation the fan face is divided into 70 area increments, each centered on one of the fan face rake total pressure probes. The local static pressure was interpolated for each total probe (extrapolated for the innermost probe on each rake) from the nearest cowl static and Prandtl static pressure values. Using these values and the tunnel total temperature the airflow was calculated for each area increment. Summation of the flow increments provided the second inlet airflow calculation. The fan duct exit and compressor inlet airflows were calculated similarly from the respective rake instrumentation readings. When added together these provided a third independently calculated airflow measurement.

The calculation procedure for additional parameters discussed under "Test Results" are described below.

Fan face recovery (PTFA) area weighted average total pressure at the fan face divided by the tunnel total pressure. Recovery values were similarly calculated for the compressor face rakes (PTCA) and the fan duct exit rakes (PTMA).

Fan face distortion (DISF) the difference between the maximum and minimum of all total pressure readings at the fan face divided by the area weighted average total pressure. Distortion was similarly calculated for the compressor face rakes (DISC)

## TEST RESULTS

### Small Scale Inlet Model

The small scale inlet model was tested in the Boeing 9- by 9-foot wind tunnel at angles of attack ranging from  $45^{\circ}$  to  $120^{\circ}$  and tunnel velocities from 0 to 77 m/s (150 knots). The test conditions and corresponding run numbers are identified in figure 22.

The primary objective of the scale model test was to validate the asymmetric inlet design, i.e., demonstrate that the flow separation boundaries for the asymmetric inlet are similar to those obtained previously on a high-contraction-ratio axisymmetric inlet model designated QF2 (see "Inlet Design"). Figure 23 shows that this objective was met. The  $-\Delta W$  separation boundaries for the asymmetric LCF inlet are nearly identical to the QF2 inlet boundaries indicating that the inlet angle-of-attack capability has not been degraded by reducing the overall contraction ratio (hilt area divided by throat area) from 1.73 to 1.50. (Note in figure 23 that increasing the inlet airflow increases the separation-free operating range. In other words, when operating at a given freestream condition, the inlet will be separated below a certain airflow and attached above that airflow.)

Another objective of the small scale test was to develop inlet mass-flow calibration curves as a function of inlet angle of attack and tunnel velocity in preparation for the full scale test. For this purpose the model was provided with static pressure taps at the minimum cowl radii at  $0^{\circ}$ ,  $90^{\circ}$ , and  $180^{\circ}$ . A mass flow coefficient,  $C_{DT}$ , was defined as the ratio of the flow passing through the minimum area of the inlet to the ideal maximum flow through the same area at freestream total pressure and temperature. The actual flow was measured downstream of the inlet with a calibrated venturi flow meter. When plotted against an average of the static pressures the massflow coefficient was found to be independent of inlet angle of attack or freestream velocity when the inlet airflow was attached. The resulting calibration curve is shown in figure 24. This curve was later used for determining the inlet flow during the large scale test. Note that when the small scale inlet was operated with large regions of separated flow the data shifted away from this curve as a function of angle of attack and freestream velocity. Thus, the calibration curve in figure 24 is valid only when the inlet flow is fully attached or when a small separation is present downstream of the throat but becomes invalid when the point of separation moves upstream of the inlet throat.

Part of the airflow data from the small scale inlet test were lost due to a malfunction in the venturi pressure measurements. These airflows were recalculated using the calibration curve in figure 24.

A third objective of the small scale test program was to obtain preliminary performance data for the design goal operating conditions defined in table 1. These conditions were developed from a preliminary analysis of the NAVY V/STOL mission requirements. The results are presented in figure 25 - 30.

The fan face recovery and distortion versus inlet airflow are shown in figures 25 and 26, respectively, for the various design conditions tested. As described in the "Inlet Design" section, the most severe condition for the thin (leeward) side of the cowl is ground static operation at maximum airflow. The maximum fan face corrected airflow for the V/STOL inlet is  $204 \text{ kg/sm}^2$  ( $41.7 \text{ lb/sec ft}^2$ ). At this airflow the inlet recovery is 0.998 and the distortion less than 0.01 thus validating the thin lip design.

During the design angle-of-attack operating conditions boundary layer separation is present at the lower airflows. At  $\alpha = 60^\circ$ ,  $V_0 = 64 \text{ m/s}$  (125 knots) and at  $\alpha = 75^\circ$ ,  $V_0 = 54 \text{ m/s}$  (105 knots) the inlet is separated through most of the design airflow range. For these cases a significant improvement can be achieved by a slight reduction in the design freestream velocity as indicated on figure 25. It is interesting to note that the recovery loss associated with the inlet separation is a function of the airflow at which separation takes place and that the recovery is nearly constant in the separated airflow range.

The distortion values presented in figure 26 are calculated using the customary procedure of ignoring pressures that are located less than 2.5 cm (1 inch) full scale from the cowl wall. During angle-of-attack operation the distortion exhibits an interesting trend. As the inlet airflow is reduced towards the point of separation the distortion increases slightly indicating a thickening of the cowl boundary layer prior to the inlet separation. This observation agrees with analytical predictions of the cowl boundary layer development. In the separated airflow range the distortion is highest near the point of separation and decreases as the airflow is further reduced.

Fan face total pressure maps for  $\alpha = 45^\circ$ ,  $60^\circ$ , and  $75^\circ$  are shown in figures 27-29 for conditions within or near the design airflow ranges. Maps are included only for conditions where the inlet flow is either separated or close to the point of separation since for attached points all of the probes read 100% recovery except those immersed in the cowl boundary layer. The extent of the separated region grows rapidly when the airflow is reduced below the initial separation value. The flow pattern also appears more distorted if the separation takes place at a relatively high inlet airflow as may be seen by comparing map no. 4 in figure 28 with map no. 2 in figure 27. The two maps were recorded at approximately the same inlet airflows but at significantly different freestream conditions. The  $\alpha = 60^\circ$ ,  $V = 64$

m/s (125 knots) in figure 28 is the more severe condition of the two and therefore causes separation at a higher inlet airflow. The result is a more severe distortion pattern and lower recovery throughout the separated airflow range compared with the less severe freestream condition in figure 27.

The inlet recovery and distortion plots in figures 25 and 26 indicate that there is no apparent separation within the design airflow ranges at  $\alpha = 90^\circ$ ,  $V_0 = 39$  m/s (75 knots) and  $\alpha = 120^\circ$ ,  $V_0 = 21$  m/s (40 knots). However, the fan face maps for the  $\alpha = 120^\circ$  condition, figure 30, show that a small total pressure loss occurs near the sides of the inlet, i.e., at the  $90^\circ$  and  $270^\circ$  circumferential positions. This type of flow pattern was also present under similar freestream conditions on the axisymmetric QF2 inlet and is thus not associated with the asymmetric contours of the LCF inlet. The flow phenomenon causing this total pressure loss is not understood at the present but the effect it has on the overall inlet recovery and distortion appears to be negligible. It should be noted that during the small scale testing no attempt was made to simulate the effect of fan suction on the inlet flow field. Thus the above fan face maps are not necessarily representative of the distortion patterns that the fan will see, but merely provide a preliminary indication of the type of flow that can be expected in the inlet.

#### Static Test, Large Scale Model

Following the large scale design/fabrication phase of the program the engine/ nacelle unit with associated control and data systems was set up, checked out, and tested statically at the Boeing engine test site, Tulalip, Washington. The primary purpose of the static test was to checkout and operate all systems and instrumentation prior to entry in the NASA Ames 40-by 80-ft wind tunnel.

During the static test the engine was operated through its entire range of power at various fan blade angles to provide a complete map of the fan operating characteristics and to establish a baseline performance for comparison with the subsequent wind tunnel test results. The effect of a ground plane on the fan/engine operation and performance during simulated vertical takeoff and landing was also evaluated during the testing at Tulalip. A summary of the test points obtained in the static test is presented in figure 31.

The corrected inlet airflow,  $WK1A$ , is shown in figure 32 versus corrected power-turbine speed,  $KN2$ , at various fan blade angles. The maximum inlet airflow is approximately  $170 \text{ kg/sm}^2$  ( $35 \text{ lb/sec ft}^2$ ). This result agrees with previous test results from the Q-fan/engine assembly. The results also show that it is necessary to vary both  $\beta$  and  $KN2$  to cover the desired inlet airflow range of about  $75 - 170 \text{ kg/sm}^2$  ( $15-35 \text{ lb/sec ft}^2$ ) in the wind tunnel test.

The inlet airflow, WK1A, plotted in figure 32 is based on the airflow calibration curve, figure 24, established during the small scale test. As described in the "Data Reduction" section two additional methods are available for calculating the inlet airflow, namely W2 (based on fan face rakes) and W3 (based on fan nozzle rakes plus core engine compressor face rakes). A comparison of the three methods is presented in figure 33. Above 90 kg/s (about 200 lb/sec), W3 is approximately 3% higher than W1 while W2 is about 4% lower than W1. Below 90 kg/s, both W2 and W3 are slightly higher than W1 possibly because W1 is less accurate at the very low airflows, see figure 24. Based on the results shown in figure 33 it is concluded that all three methods provide a reasonably accurate measurement of the inlet airflow (within  $\pm 4\%$ ). The most accurate airflow is considered to be W1, and thus WK1A, since it is based on a direct calibration of a geometrically similar model. This airflow will therefore be used in the analysis of the large scale inlet data.

For the proposed NAVY V/STOL aircraft the variable pitch fan feature is used as the primary means for controlling and adjusting the thrust (and thus the inlet airflow) while the fan rpm is constant. With the present test set-up it is more convenient to change fan rpm (through a power lever angle change) while maintaining a fixed blade angle. It was therefore of interest to determine if the inlet flow field is sensitive to the method with which the airflow is controlled. The  $0^\circ$  and  $180^\circ$  cowl static pressure distributions are shown in figure 34 for two data points recorded at the same inlet airflow but at different combinations of  $\beta$  and KN2. These pressure distributions as well as the fan face average static pressures (see table in figure 34) indicate that the inlet flow field is independent of the  $\beta$ /KN2 settings as long as the corrected inlet airflow is unchanged. This means that a variation in inlet airflow by means of varying the fan blade angle at constant KN2 can be accurately simulated by changing KN2 at constant blade angle. This information was used to establish an efficient wind tunnel test plan.

During the initial phase of vertical takeoff and final phase of vertical landing the engine core nozzle comes in close proximity to the ground, which could create some operational problems due to back pressure and distortion in the diffusing core nozzle. This effect was evaluated during the static test as illustrated in figure 31. The engine was operated from ground idle to maximum power with the ground plane positioned at 2.13 m (7 ft.), 1.52 m (5 ft.), and 0.91 m (3 ft.) from the core exit plane. These distances correspond to 3.75, 2.68, and 1.60 core exit diameters. The main conclusion from these tests is that the ground effect is negligible. Only small increases in turbine interstage temperature, TT7, were observed as the ground plane was moved closer and closer to the core exit. Figure 35 shows the calculated fan thrust versus corrected engine power with and without ground plane. There is no evidence of any significant effect from the ground plane.

## Wind Tunnel Test, Large Scale Model

As described in reference 1, mechanical failures in the T55/Q-fan propulsion unit twice interrupted the 40 x 80 foot wind tunnel test program. The first failure occurred before any angle-of-attack data had been obtained. On the second wind tunnel entry a limited amount of data had been obtained at angle-of-attack conditions when the unit failed. These results are presented in the following sections.

Inlet Performance and Separation Boundaries.—The test conditions that were completed prior to the failure as well as the design conditions are shown in figure 36. The failure occurred only one run away from the first design condition to be tested.

Fan face recovery and distortion data for the wind-on test conditions are presented in figures 37 and 38. The inlet recovery is nearly insensitive to angle-of-attack (above 0.997 at all conditions tested). The distortion increases with angle-of-attack as a result of a thickening boundary layer on the windward cowl. If the outer 2.5 cm (one inch) of the boundary layer is ignored, as is typical for certification distortion, the maximum distortion measured, 0.075 at  $\alpha = 60^\circ$ ,  $V_0 = 39$  m/s (75 knots), WKIA = 167 kg/sm<sup>2</sup> (34.2 lb/sec. ft<sup>2</sup>), drops to only 0.016.

As indicated on figure 38, inlet separation was observed at  $\alpha = 60^\circ$ ,  $V_0 = 39$  m/s (75 knots) when the fan face corrected airflow was reduced below about 69 kg/sm<sup>2</sup> (14.0 lb/sec. ft<sup>2</sup>). One data point was recorded at 67.9 kg/sm<sup>2</sup> (13.9 lb/sec. ft<sup>2</sup>) and there was no indication of high fan blade stress levels or increased compressor face distortion. The steady state fan face rake data was lost for this data point due to faulty scanivalves but the on-line 180° fan face rake profile clearly indicated separation extending from the cowl to about midway between the cowl and the spinner. In addition, the kulite probe located closest to the cowl on the 180° fan face rake shows a slight increase in turbulence level thus verifying the on-line observation.

One of the test objectives was to establish the flow separation boundaries for the large scale inlet. Only one separation point was found during the brief testing period. However, similar boundaries have already been established on the small scale model and it appears possible to use this information to extrapolate the large scale single-point data. Figure 39 shows the separation boundaries for the small scale model and the single point for the large scale inlet. Based on the small scale model results, an empirical expression was derived which nearly collapses the separation boundaries into a single value

$$\tan \phi = \frac{V_0 \sin \alpha}{V_{TH} + V_0 \cos \alpha}$$

where

$V_0$  = tunnel freestream velocity  
 $V_{TH}$  = inlet throat velocity (one-dimensional)  
 $\alpha$  = inlet angle of attack.



The physical definition of  $\phi$  is depicted in figure 40.

Figure 41 compares the experimental results with the empirical boundaries obtained for a  $\phi$ -value of 18.2°. A remarkably good agreement is evident at fan face corrected airflow levels of 73, 98, 122 and 146 kg/sm<sup>2</sup> (15, 20, 25 and 30 lb/sec ft<sup>2</sup>), whereas the empirical prediction is optimistic at 171 kg/sm<sup>2</sup> (35 lb/sec ft<sup>2</sup>). Since the small scale separation boundaries thus can be closely simulated by a single value of  $\phi$ , at least up to about 146 kg/sm<sup>2</sup> (30 lb/sec ft<sup>2</sup>), it is reasonable to derive the  $\phi$ -value for the single separation point recorded in the large scale inlet test and calculate the corresponding large scale separation boundaries. The results are shown in figure 42. The empirically predicted separation boundaries for the large scale inlet are significantly improved over those for the small scale model.

The inlet design conditions and the corresponding fan face corrected airflow ranges are shown in figure 43 with the predicted separation boundaries. The worst case appears to be at  $\alpha = 75^\circ$ ,  $V_0 = 54$  m/s (105 knots). Here the design airflow varies from 103 to 176 kg/sm<sup>2</sup> (21 to 36 lb/sec ft<sup>2</sup>) while the inlet is predicted to separate below 122 kg/sm<sup>2</sup> (25 lb/sec ft<sup>2</sup>). Data from the small scale inlet indicates that when inlet separation takes place at or below 122 kg/sm<sup>2</sup> (25 lb/sec ft<sup>2</sup>), the associated fan face total pressure distortion is less than 10%.

The empirical correlation established from the small scale model test results has been applied to the large scale inlet to predict the separation boundaries using a single data point. It was assumed that the laws that control separation in the small scale inlet also apply to the large scale inlet, i.e., that separation occurs as a result of boundary layer profile deterioration in the adverse pressure gradients along the cowl lip and diffuser, and that the higher Reynolds number is the sole reason for the improved separation boundaries for the large scale inlet. If the uniform flow suction created by the fan at the diffuser exit plane significantly changes the upstream flow field and thus the point of separation, the assumption of a constant  $\phi$  value for the entire airflow range (70 - 150 kg/sm<sup>2</sup>) is probably not valid. However, the results of an analytical study indicate that the effects of the higher Reynolds number are sufficient to account for the improvement observed at  $\alpha = 60^\circ$ ,  $V_0 = 38.6$  m/s (75 knots).

The study involved analysis of the experimentally determined cowl static pressure distributions with a finite difference type, compressible flow boundary layer computer program. The pressure distributions were input as though the flowfield were axisymmetric, whereas the actual flow is three dimensional. This procedure has been applied successfully in similar studies previously. The analysis was conducted for a series of large scale test points recorded at  $V_0 = 38.6$  m/s (75 knots),  $\alpha = 60^\circ$  to determine the effect of inlet airflow rate on the boundary layer development. The computer program was run at Reynolds numbers corresponding to full scale and

0 273 scale model dimensions at each point. The program recognizes separation when the calculated local skin friction coefficient becomes zero. The separation points predicted in this manner are compared with the experimental separation points in figure 44. The figure shows the maximum value of the computed profile shape factor,  $H_1$ , as a function of fan face corrected airflow. As the airflow decreases the shape factor increases indicating a deteriorating boundary layer profile. Separation is predicted at  $WKIA = 72 \text{ kg/sm}^2$  ( $14.9 \text{ lb/sec ft}^2$ ) for the large scale inlet and  $102 \text{ kg/sm}^2$  ( $20.9 \text{ lb/sec ft}^2$ ) for the small scale inlet. These airflow levels are compared with the airflow levels where the inlets were considered to be separated as judged from on-line indications in the wind tunnel, and review of off-line data. The predicted points appear to be slightly conservative. Detailed analysis of the small scale experimental data, prompted by the results of the boundary layer computations, indicated that small pockets of separated flow were in fact present at the conditions where separation was predicted for the small scale inlet. These separations, however, did not cause a significant increase in distortion, thus revision of the previously developed separation boundaries is not considered necessary. The main conclusions from this figure is that the boundary layer analysis provides a theoretical explanation for the observed difference between small and large scale models. It is further indicated that if the static pressure profile along the cowl wall is known the analysis predicts the point of separation with reasonable accuracy.

The objective of the above study was to evaluate the influence of model scale on flow separation. The large scale experimental pressure distributions were used for analyzing both the large and small scale models in order to isolate the Reynolds number effect.

Experimental cowl pressure distributions obtained with the two models at similar test conditions are plotted in the upper part of figure 45. As expected, the two profiles are nearly identical. However, the boundary layer analysis predicts a lower peak  $H_1$  value when using the small scale data as shown in the lower part of figure 45. This effect is evidently due to the minor difference in static pressure at station 1.48, rather than the more noticeable difference near the hilite. In the previous analysis the separation points would have been predicted at slightly lower airflows, using the small scale data, but the basic difference (between small and large scale) due to Reynolds number would have been obtained as well.

Fan and Engine Operating Characteristics.—One of the test objectives was to determine if the performance of the fan/ engine installation would be significantly influenced by the severe angle-of-attack conditions required for V/STOL aircraft operation. Possible adverse effects include increased compressor face distortion due to inlet separation as well as fan and core nozzle flow separations due to the strong crosswind at the exits. An analysis of the test results with that objective in mind is presented in this section.

The compressor face total pressure recovery and distortion levels for several freestream conditions are presented in figure 46. The results

indicate a rather large scatter in recovery ( $\pm 0.5\%$ ). However, the distortion is not affected by the angle-of-attack changes. The small inlet separation present at the low airflow point at  $\alpha = 60^\circ$  (see "Inlet Performance and Separation Boundaries") does not influence the compressor face flow.

The fan nozzle rake profiles for two different massflow levels at a low and a high angle of attack condition are shown in figure 47. The profiles for the leeward ( $0^\circ$ ) and windward ( $180^\circ$ ) sides are quite similar, especially at the low airflow condition, and there is no apparent difference in profile shape between the  $0^\circ$  and  $90^\circ$  angle-of-attack conditions

Figure 48 shows the fan nozzle rake profiles for a series of inlet airflows at  $V_0 = 39$  m/s (75 knots) and  $\alpha = 60^\circ$ . Again there is no indication of crosswind-induced flow separation or profile distortion. The data point shown with solid symbols was recorded with a boundary layer separation present in the inlet. The peculiar profile shape near the fan cowl at  $180^\circ$  is probably a remnant of the total pressure profile upstream of the fan. From figures 47 and 48 it is concluded that the two high angle-of-attack conditions tested,  $\alpha = 90^\circ$  at  $V_0 = 21$  m/s (40 knots) and  $\alpha = 60^\circ$  at  $V_0 = 39$  m/s (75 knots), did not significantly change the flow characteristics through the fan nozzle.

The effect of the crosswind on the core exit nozzle is examined in figure 49. Here the engine torque is plotted against power lever angle for various forward speed and angle-of-attack conditions. If the crosswind has an adverse effect on the core nozzle flow the engine torque for a given power lever angle should decrease. Since the data points fall on a single curve it is concluded that the core nozzle performance is insensitive to crosswind within the range of conditions tested.

Nacelle Forces.—Nacelle forces and moments were measured with a six-component balance system connected to the 40- by 80-foot wind tunnel semispan turntable. The purpose of the force measurements was primarily to determine the effects of inlet separation on fan thrust at various airflow levels. Since separation was observed only at a very low power setting it is not possible to make this evaluation.

For flight control purposes it is necessary to establish the various forces and moments acting on the nacelle during low speed maneuvering. To aid in this work, the measured forces in the streamwise and lift directions as well as the nacelle pitching moments are tabulated in table 2 for various inlet massflows and freestream conditions. The calculated inlet velocity ratio ( $V_0/V_H$ ) and ram drag ( $F_R$ ) are included in the table.

An analysis of the pitching moment data is presented in figure 50. Since the fan nozzle total pressure profiles have been shown to be symmetrical and independent of angle-of-attack (see previous section), it can be assumed that the gross thrust does not contribute to the pitching moment, i.e., the

thrust vector acts along the engine centerline. The effect of the external flow on the moment can also be assumed to be negligible at these low forward speeds. Thus, the pitching moment is simply a result of the offset,  $H$ , of the captured streamtube from the pitching moment reference center, which in this analysis has been transferred to the center of the hilite-plane. The figure shows that the centerline of the capture streamtube moves upwards when (1) the inlet airflow is reduced (increasing  $V_0/V_H$ ), (2) the angle-of-attack is increased, and - to a smaller extent - (3) the forward speed is reduced.

### CONCLUDING REMARKS

An asymmetric inlet was designed to provide high performance during low speed operation at high angles of attack. The design features a thick lip on the windward side and a relatively thin lip on the leeward side of the inlet. The overall contraction ratio, defined as the hilite area divided by the minimum area, is 1.50 for the asymmetric inlet lip.

A small scale model of the inlet was tested with an open duct flow suction system in a low speed wind tunnel. The test results validated the asymmetric design concept and provided valuable data for the planning and preparation of the subsequent large scale wind tunnel test.

The large scale inlet model was tested with a high bypass ratio turbofan in the NASA Ames Research Center 40- by 80-ft wind tunnel. Although the test was cut short by a mechanical failure, it is concluded that the performance of the large scale inlet is significantly improved over that of the small scale model. To reach this conclusion an empirical correlation established for the small scale inlet was applied to the limited test results for the large scale inlet. With this method it is predicted that within the design envelope boundary layer separations should occur only at low airflows on the large scale inlet. Thus, the distortion and fan blade stress levels associated with the separation should be relatively small.

Boundary layer analysis of the experimental surface static pressure distributions indicates that the observed difference in aerodynamic performance simply is a result of the difference in Reynolds number. Furthermore, the good agreement between the analytical predictions and the experimental results implies that the inlet separation can be predicted if the static pressure profiles along the cowl wall are known.

## REFERENCES

1. Shain, W. M., "Test Data Report - Low Speed Wind Tunnel Test of a Full Scale Fixed Geometry Inlet with Engine at High Angles of Attack," NASA CR-151927, November 1976.
2. Demers, W. J , et al, "Testing of the Hamilton Standard Q-Fan Demonstrator (Lycoming T55-L-11A Core Engine)," NASA CR-121265, March 1973.

TABLE 1, - DESIGN CONDITIONS

Forward Speed $V_o$ (m/s)	Angle of Attack $\alpha$	Airflow Range WK1A (kg/sm <sup>2</sup> )
72	45 <sup>0</sup>	73 - 146
64	60 <sup>0</sup>	78 - 151
54	75 <sup>0</sup>	103 - 176
39	90 <sup>0</sup>	127 - 205
21	120 <sup>0</sup>	132 - 205

$V_o$ (m/s)	$\alpha$	$WK1A_2$ (kg/sm <sup>2</sup> )	$V_o/V_H$	RAM DRAG $F_R$ (NEWTON)	STREAMWISE FORCE $F_X$ (NEWTON)	LIFT FORCE $F_Y$ (NEWTON)	PITCHING MOMENT $M_Z$ (Nm)
20.3	0°	166	.214	3944	-23766	13	-199
		152	.235	3754	-19367	-142	-190
		136	.263	3256	-15372	-120	-107
		117	305	2845	-10835	-151	-151
		93	386	2215	-6405	-151	-125
		69	522	1630	-3661	-142	-54
	45°	151	.237	3578	-12103	17071	7567
		117	307	2801	-6187	10502	6091
		69	.520	1677	-1352	4791	4186
38.9	0°	150	.238	3538	5369	23330	11190
		109	.328	2611	4586	12374	8068
		69	.524	1648	3679	5943	5435
	20°	164	.419	7419	-19949	-325	-686
		146	.473	6606	-14812	-396	-521
		133	.518	6170	-11734	-391	-506
		111	.622	5127	-7157	-307	-384
		77	.896	3559	-2696	-298	-300
		58	1.193	2674	-1059	-316	-335
	45°	164	.420	7553	-17894	10907	7813
		146	.473	6743	-13219	8909	7284
		131	.528	6013	-9972	7495	6643
		109	.636	4966	-5720	5547	5728
		76	.904	3465	-1846	3639	4520
		59	1.164	2686	-529	2931	3980
	60°	149	.465	6722	-6579	18993	15031
		111	.625	4987	-1121	11809	11568
		60	1.154	2639	2308	5987	7607
	60°	167	.406	7725	-1926	27965	20271
		151	.452	6976	-249	23477	18333
		137	.498	6261	1228	19776	16833
		118	.576	5479	2829	15426	14606
		102	.670	4627	3937	11738	12483
		79	.860	3578	4595	8941	10570
		68	1.011	3100	5017	7637	9633

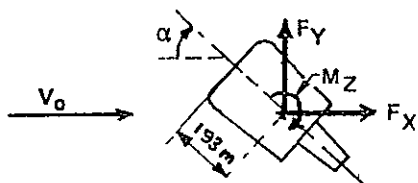


Table 2. Force Data

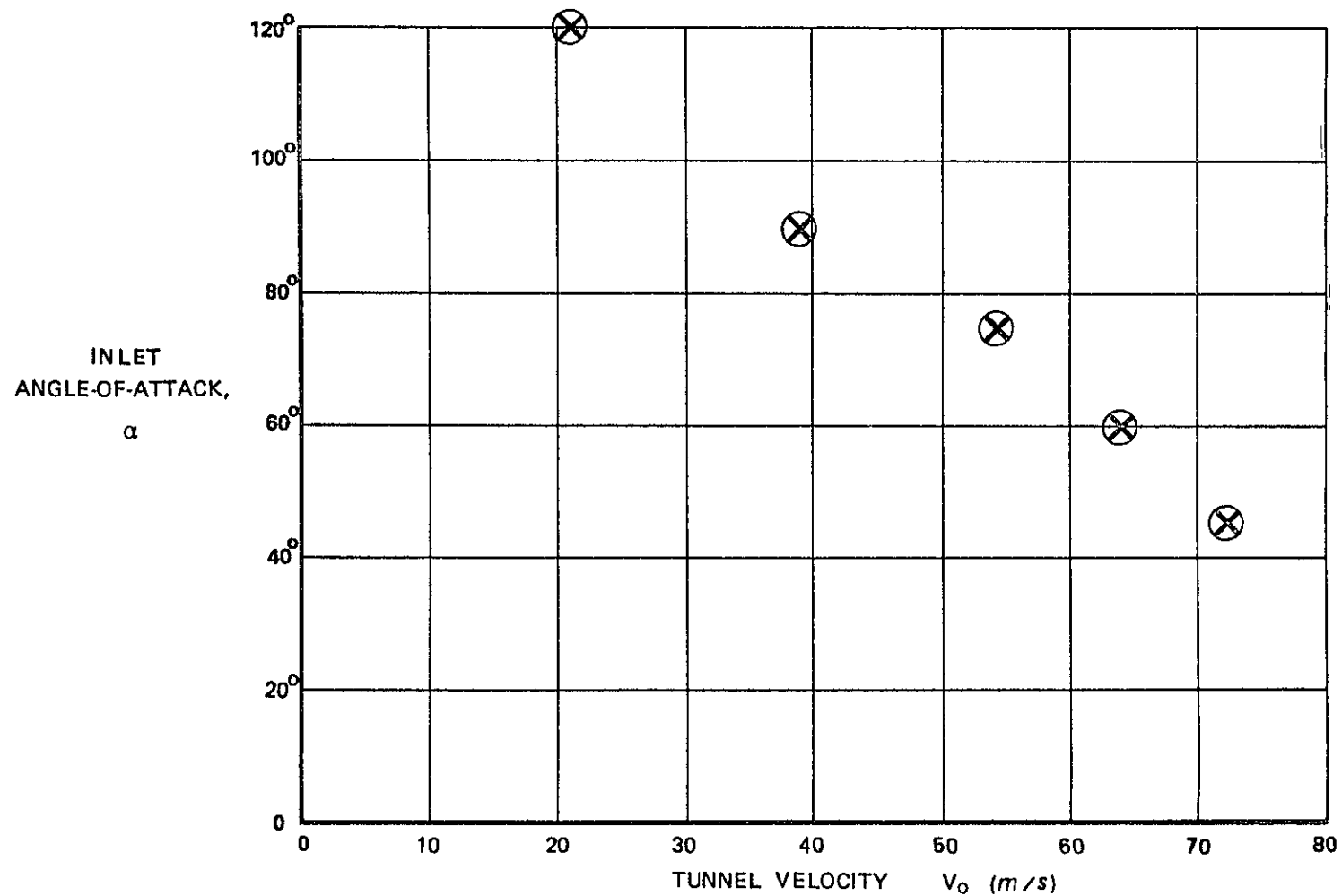


Figure 1 V/STOL Inlet Low Speed Design Points



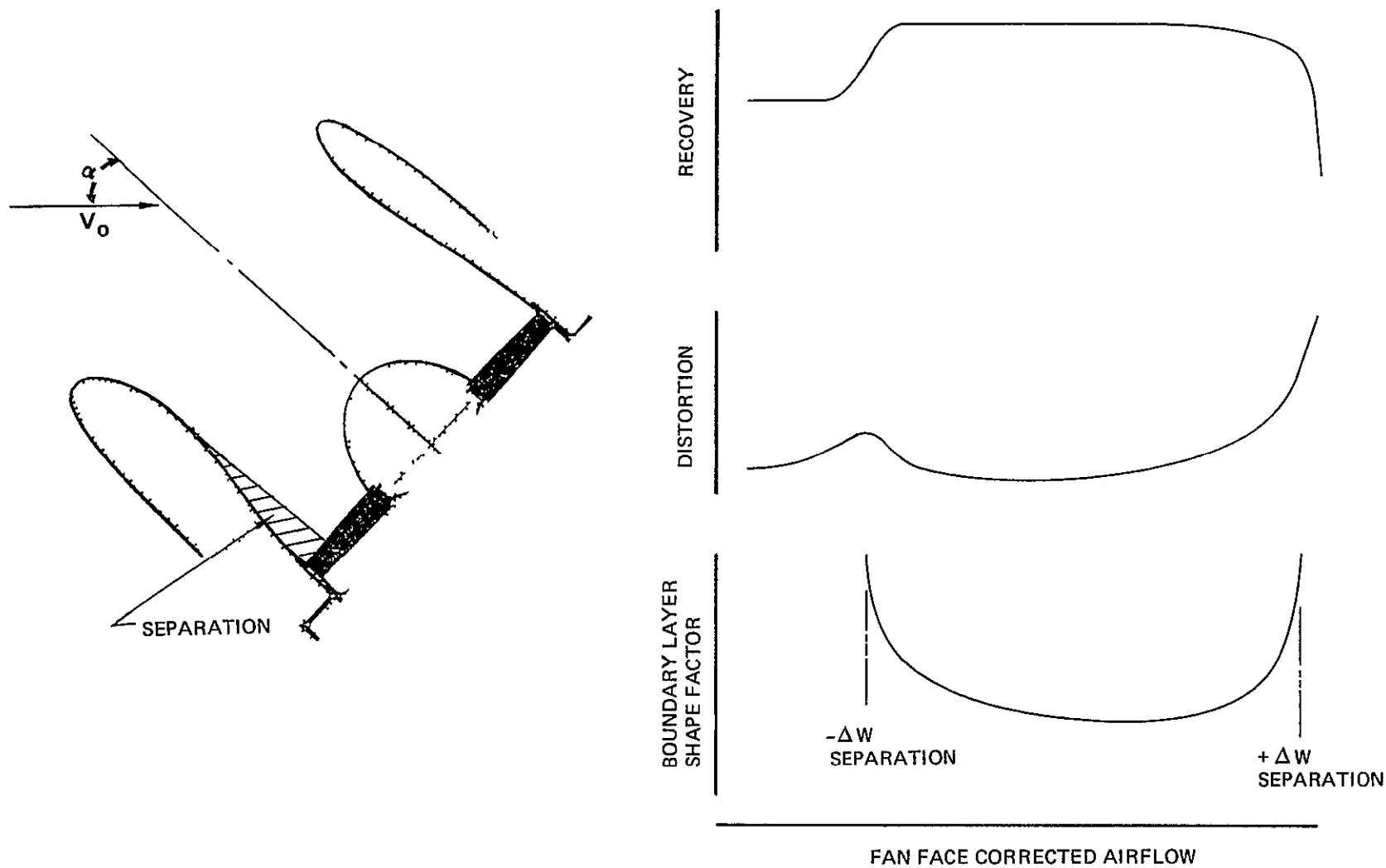


Figure 2 Effects of Flow Separation on Inlet Performance

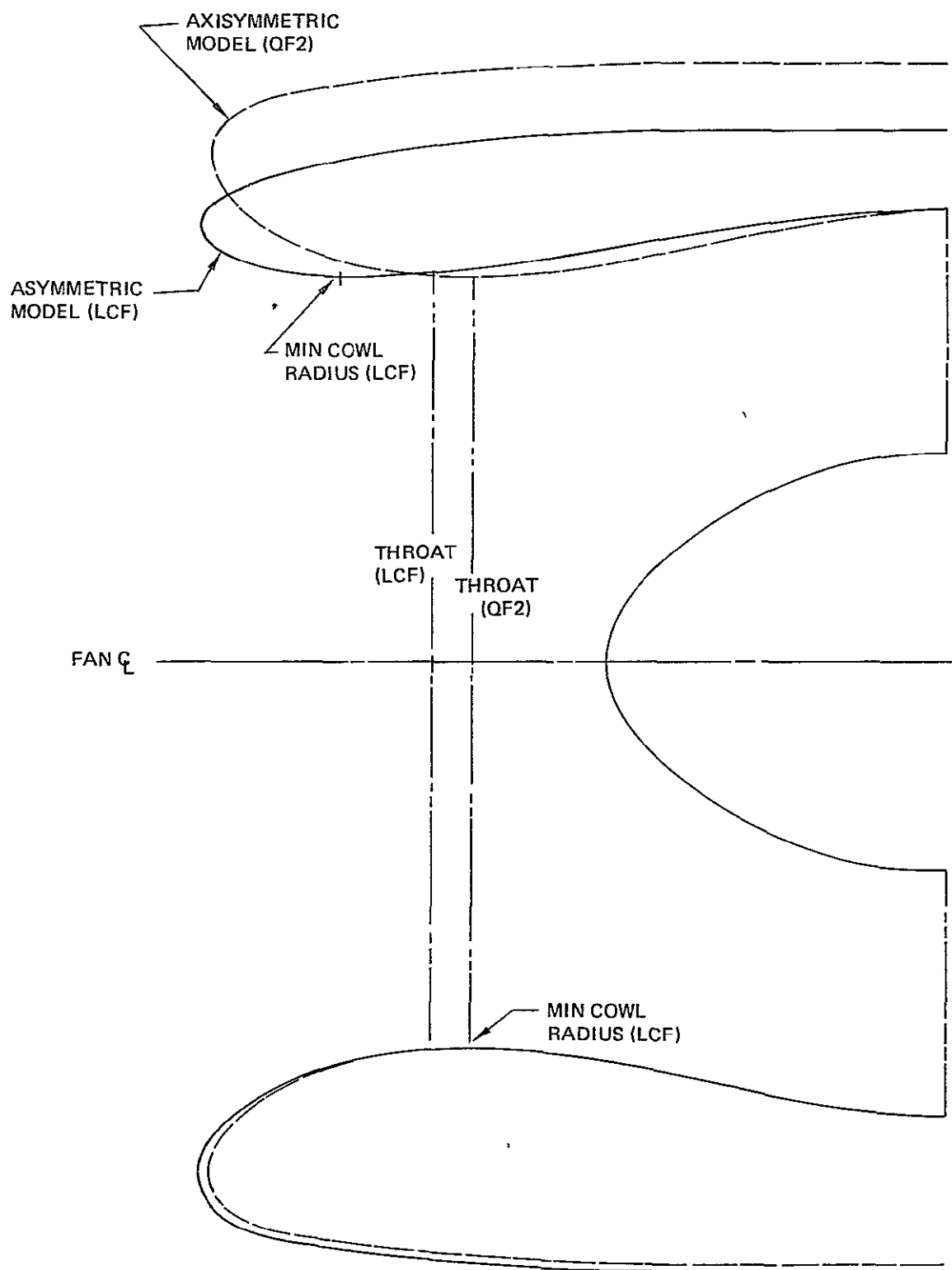


Figure 3. LCF Inlet Schematic

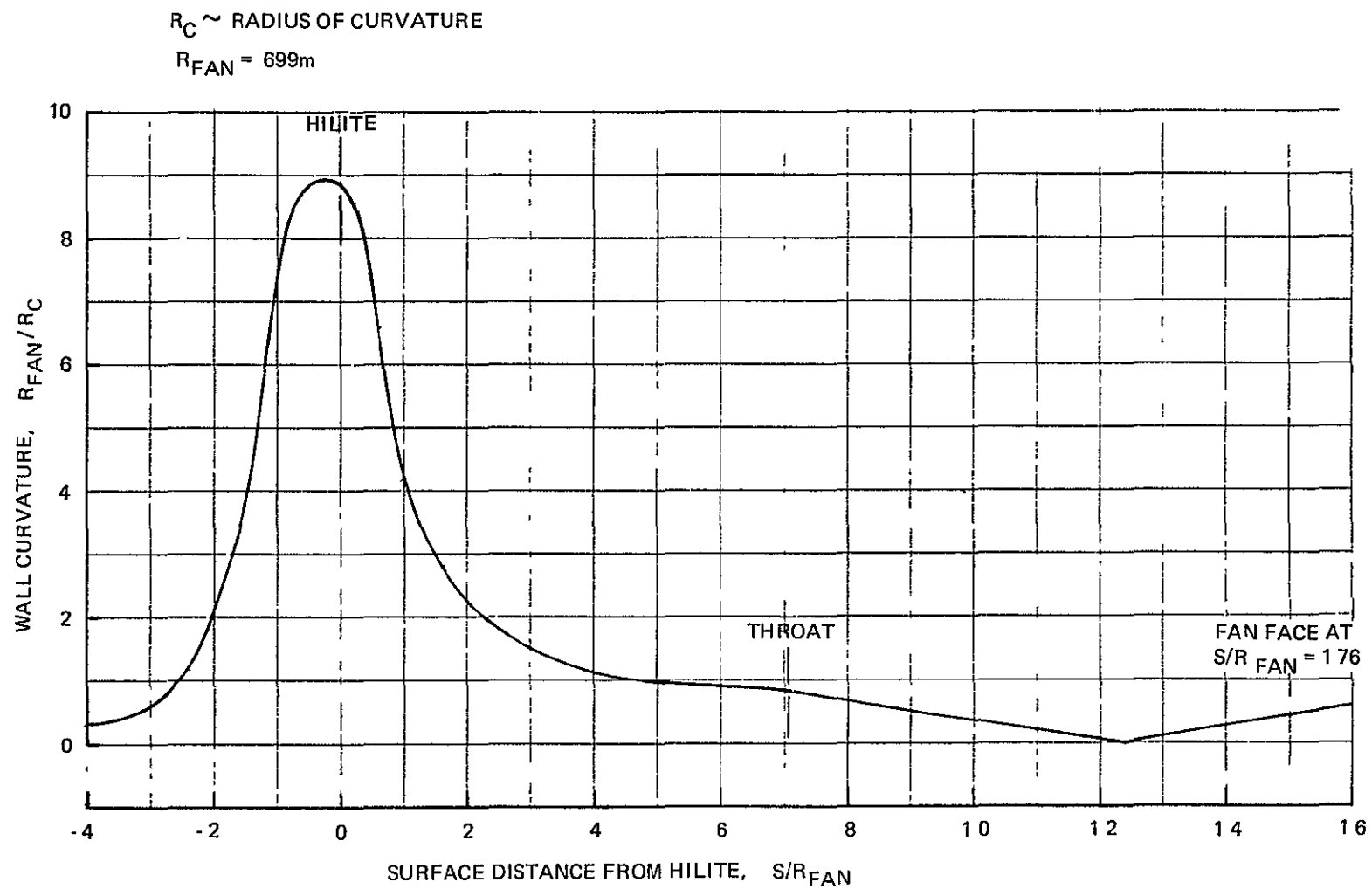


Figure 4 Windward Cowl Wall Curvature

R ~ RADIUS REFERENCED TO FAN CENTERLINE

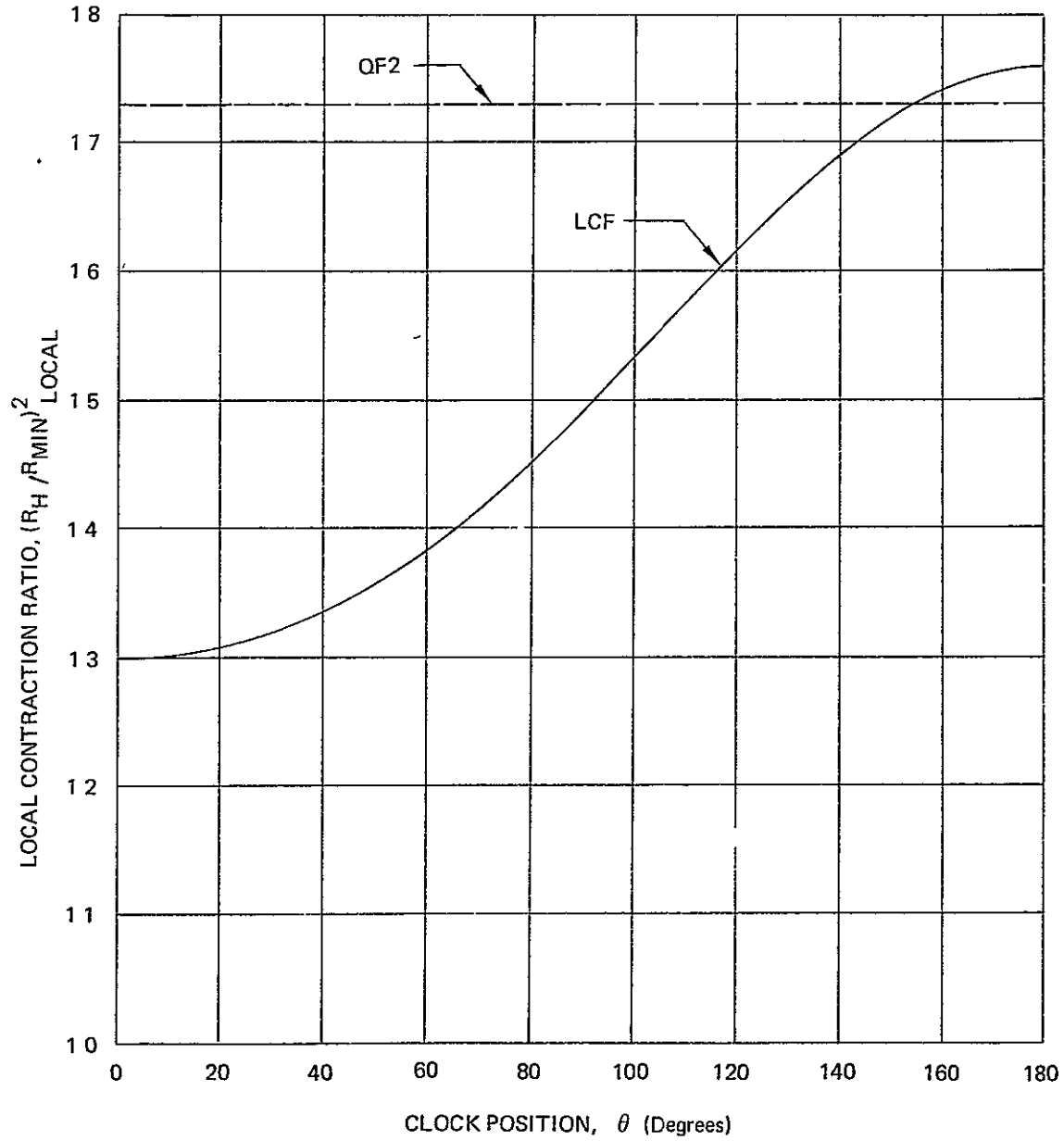


Figure 5 Cowl Lip Thickness Variation

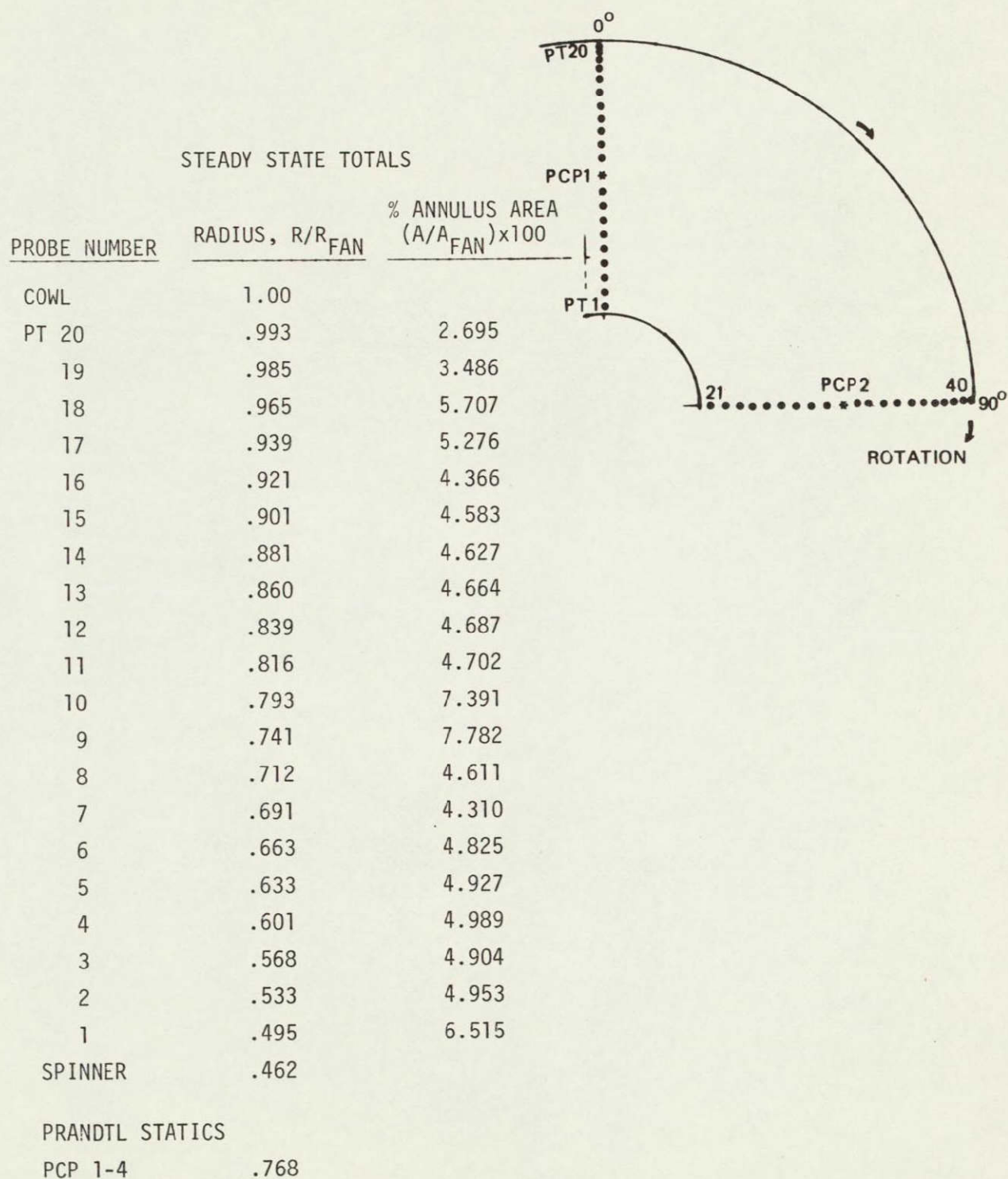


Figure 6. Small Scale Model Fan Face Rake

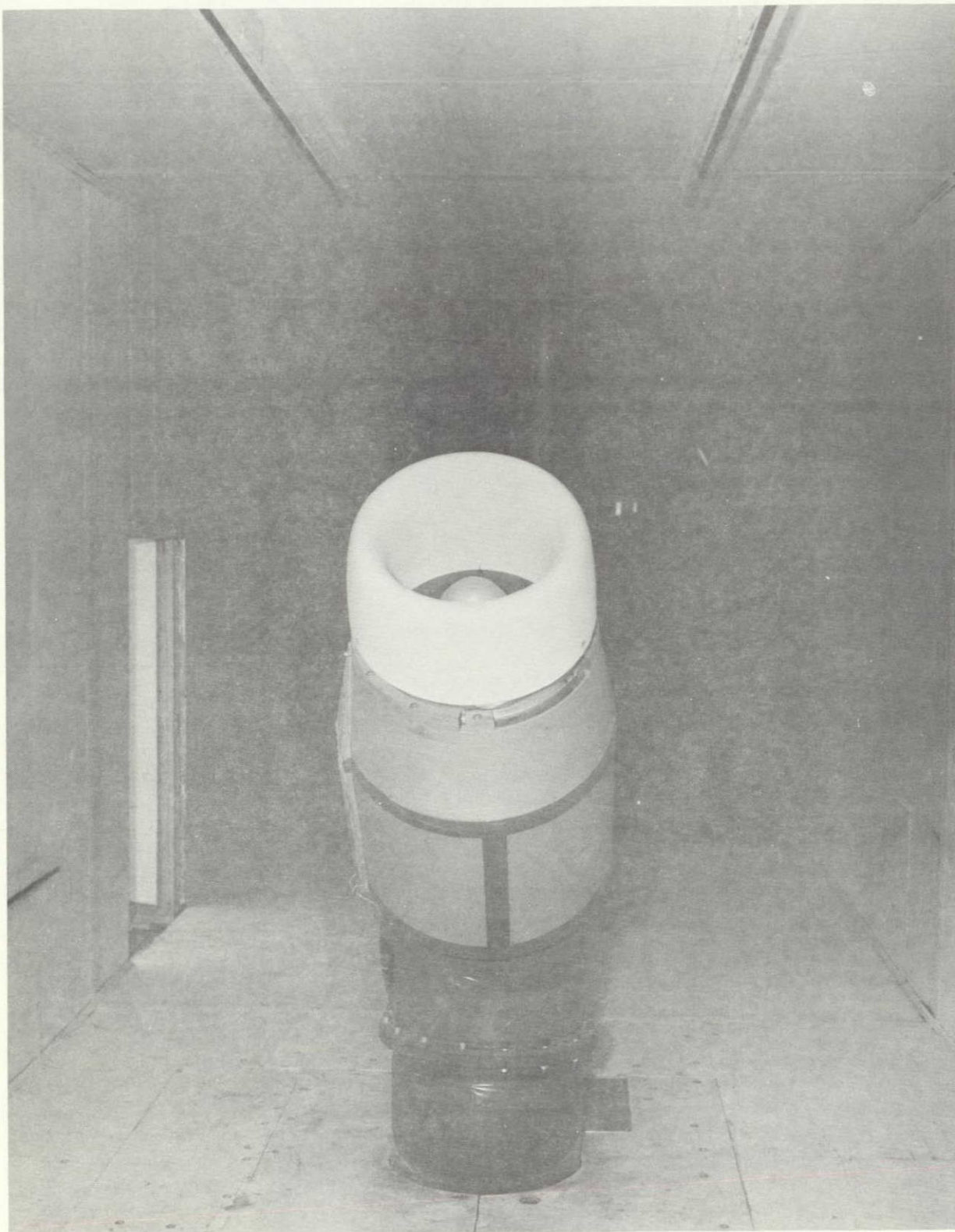


Figure 7. Small Scale Inlet Model Installed in 9- by 9-ft Wind Tunnel



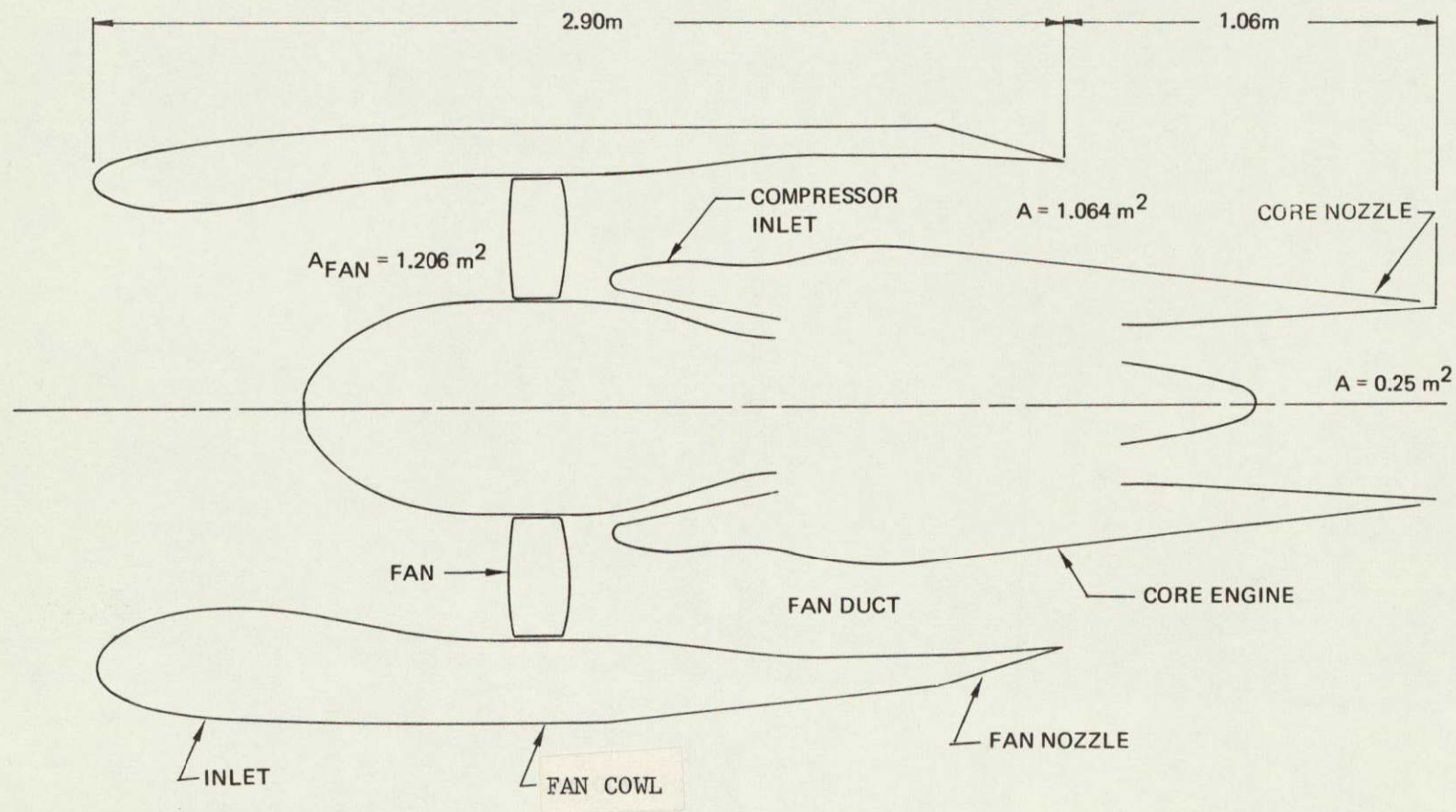


Figure 8. Nacelle Schematic

ORIGINAL PAGE IS  
OF POOR QUALITY

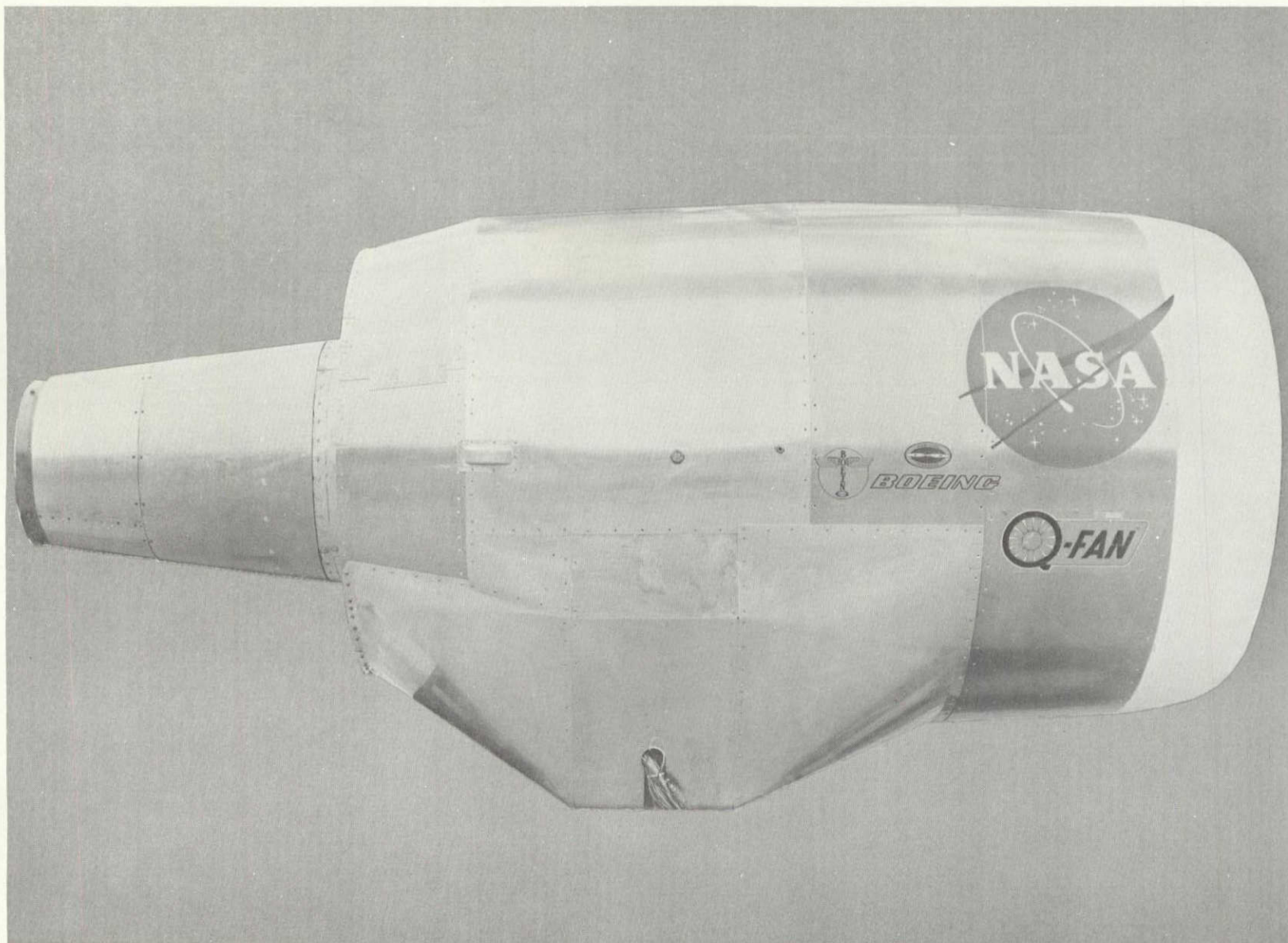
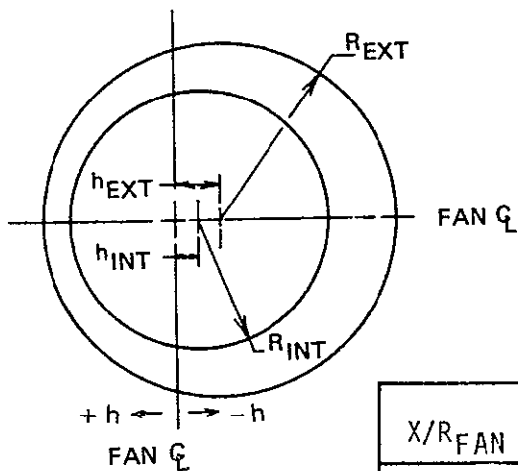


Figure 9. Nacelle Photograph





$$R_{FAN} = .6985 \text{ m}, \quad X = 0 \text{ at } h_{11ite}$$

HAMILTON STANDARD SPINNER CONTOURS	
$X/R_{FAN}$	$R/R_{FAN}$
.8863	0
.8877	.0222
.8892	.0306
.8921	.0431
.8936	.0479
.9008	.0680
.9154	.0992
.9299	.1247
.9590	.1668
.9954	.2092
1.0317	.2434
1.1045	.2997
1.1772	.3452
1.2499	.3819
1.3227	.4115
1.3954	.4339
1.4681	.4496
1.5408	.4597
1.6136	.4618
1.6368	.4618

	EXTERNAL COWL		INTERNAL COWL	
$X/R_{FAN}$	$R_{EXT}/R_{FAN}$	$h_{EXT}/R_{FAN}$	$R_{INT}/R_{FAN}$	$h_{INT}/R_{FAN}$
0	1.0514	-.0759	1.0514	-.0759
.0025	1.0700	-.0845	1.0316	-.0752
.0082	1.0848	-.0883	1.0160	-.0719
.0157	1.0971	-.0913	1.0023	-.0687
.0346	1.1172	-.0951	.9793	-.0632
.0535	1.1308	-.0968	.9622	-.0585
.0817	1.1460	-.0978	.9425	-.0528
.1100	1.1576	-.0978	.9269	-.0476
.1384	1.1672	-.0973	.9140	-.0429
.1667	1.1751	-.0964	.9032	-.0384
.2232	1.1882	-.0943	.8864	-.0301
.2799	1.1977	-.0925	.8748	-.0221
.3364	1.2084	-.0909	.8671	-.0144
.3931	1.2165	-.0896	.8622	-.0077
.4497	1.2237	-.0885	.8595	-.0019
.5063	1.2300	-.0875	.8588	.0031
.5629	1.2357	-.0867	.8601	.0073
.6195	1.2406	-.0860	.8632	.0106
.6761	1.2449	-.0855	.8680	.0131
.7327	1.2487	-.0849	.8742	.0148
.7839	1.2519	-.0845	.8816	.0158
.8459	1.2545	-.0842	.8901	.0162
.9091	1.2585	-.0837	.9093	.0155
1.0723	1.2605	-.0834	.9301	.0132
1.1463	1.2609	-.0833	.9439	.0112
1.1640			.9471	.0107
1.1640			.9659	.0073
1.1640			.9819	.0041
1.1640			.9937	.0015
1.1640			.9996	.0001
1.1640			1.0000	.0000

Figure 10 LCF Inlet Cowl Contours

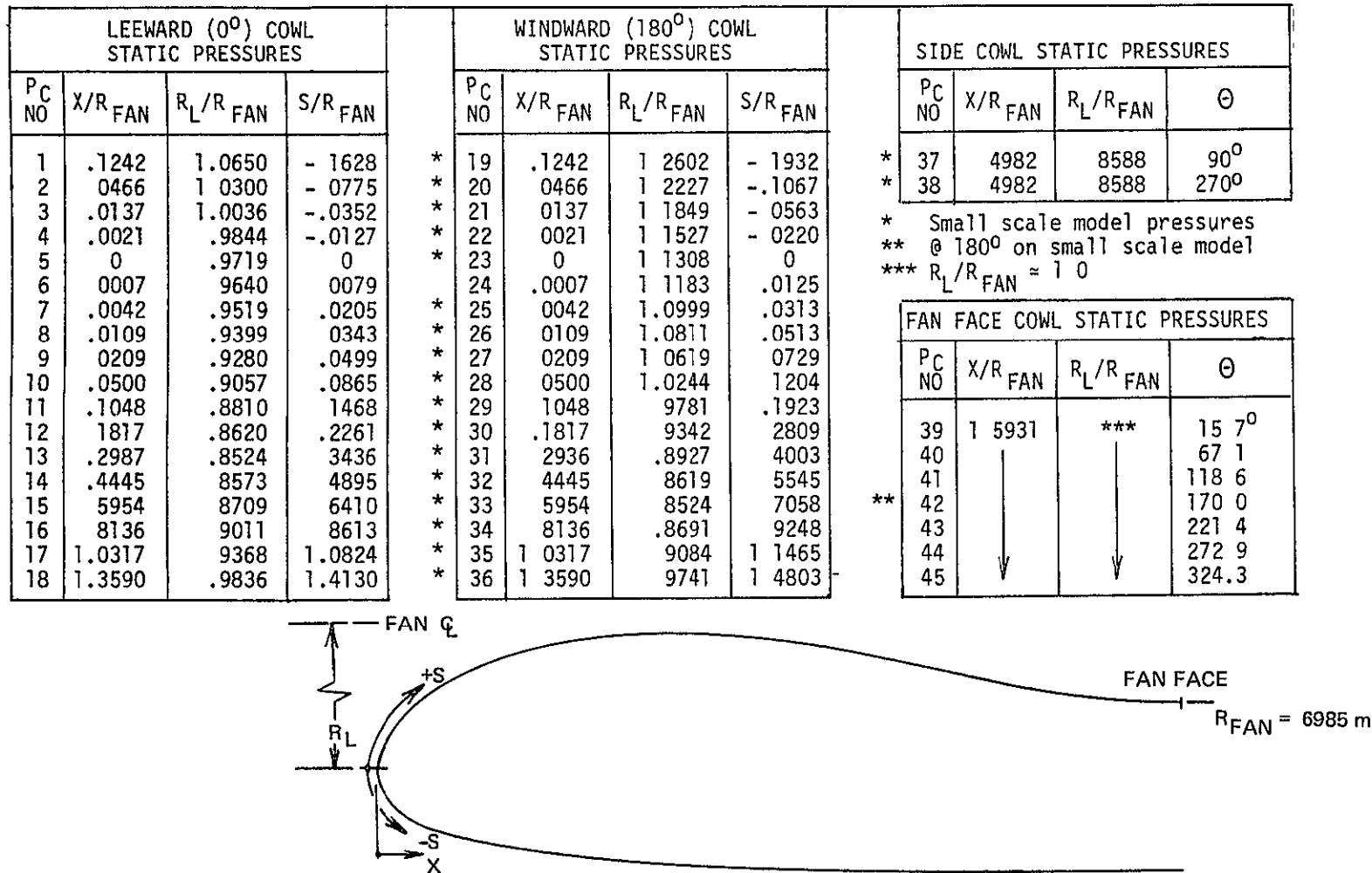


Figure 11 Cowl Static Pressure Instrumentation

# FAN FACE RAKE PROBE COORDINATES AND NUMBERING

	RAKE 1	RAKE 2	RAKE 3	RAKE 4	RAKE 5	RAKE 6	RAKE 7	RING RADIUS R/R <sub>FAN</sub>	% AREA FOR RING
RING 1	PTF 1	PTF 11	PTF 21	PTF 31	PTF 41	PTF 51	PTF 61	9901	5%
RING 2	2	12	22	32	42	52	62	.9700	5%
RING 3	3	13	23	33	43	53	63	.9286	15%
RING 4	4	14	24	34 <sup>1</sup>	44	54	64	8627	15%
RING 5	5	15	25	35	45	55	65	7914	15%
RING 6	6	16	26	36	46	56	66	7129	15%
RING 7	7	17	27	37	47	57	67	.6247	15%
RING 8	8	18	28	38	48	58	68	5582	5%
RING 9	9	19	29	39 <sup>2</sup>	49	59	69	5218	5%
	PP1	PP2	PP3	PP4	PP5	PP6	PP7	.5017	--
RING 10	10	20	30	40 <sup>3</sup>	50	60	70	4813	5%
RAKE ANGLE (deg)	25.7	77.1	128.6	180.0	213.4	282.3	334.3		

- 1 PDF 1 }  
2 PDF 2 } Dynamic total pressure probe mounted side by side with steady state probe  
3 PDF 3 }

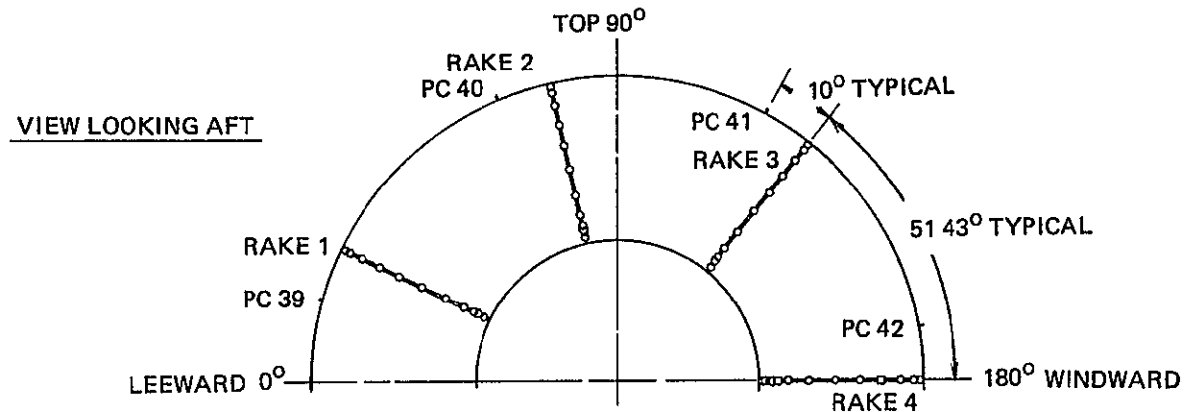


Figure 12 Fan Face Instrumentation

0° PROBES	180° PROBES	RADIUS R/R <sub>FAN</sub>	ΔA/AR
NOZZLE WALL	NOZZLE WALL	1.0676	
PM1	PM3	1.0640	
PTM1	PTM11	1.0447	142
PTM2	PTM12	.9964	134
TTM1	TTM4	.9738	
PTM3	PTM13	.9513	121
PTM4	PTM14	.9084	.110
PTM5	PTM15	.8676	.100
PTM6	PTM16	.8287	.091
TTM2	TTM5	.8102	
PTM7	PTM17	.7916	.083
PTM8	PTM18	.7556	.077
PTM9	PTM19	.7211	.071
TTM3	TTM6	.7044	
PTM10	PTM20	.6876	.073
PM2	PM4	.6767	
CORE CASE	CORE CASE	.6676	

ΔA. Area assigned to total pressure probe

AR. Flow area at rake face = 1.064 m<sup>2</sup>

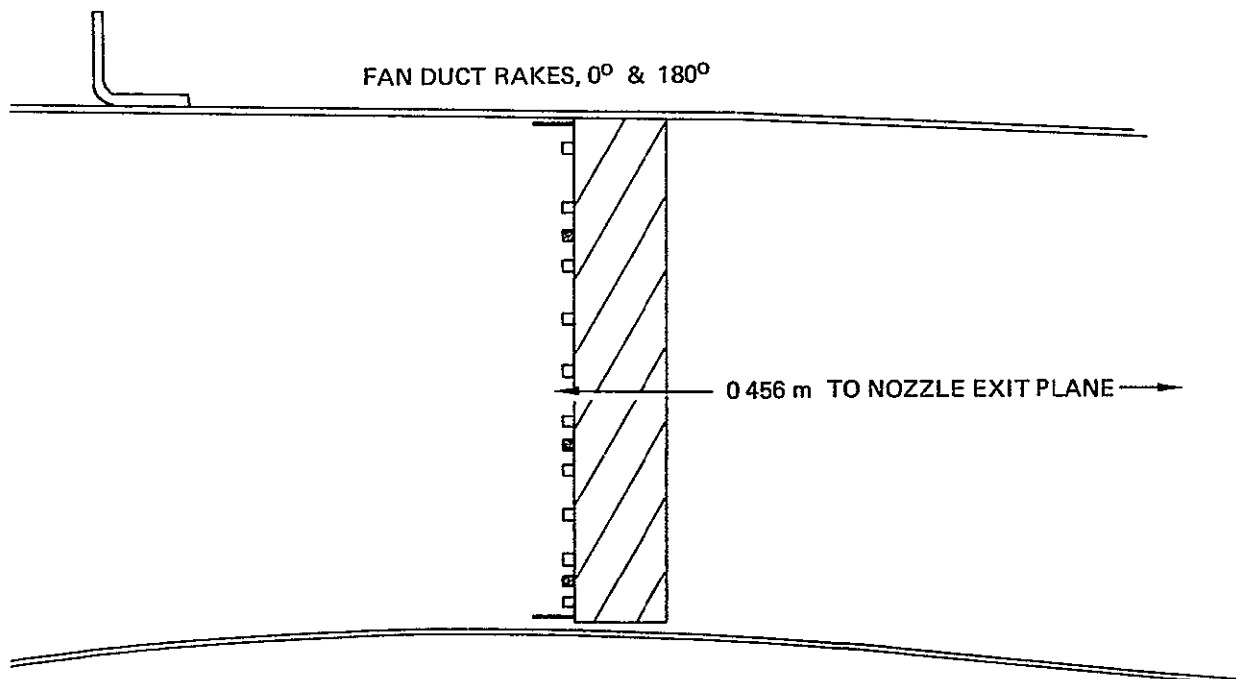


Figure 13. Fan Duct Instrumentation

VIEW LOOKING FROM FRONT TO REAR

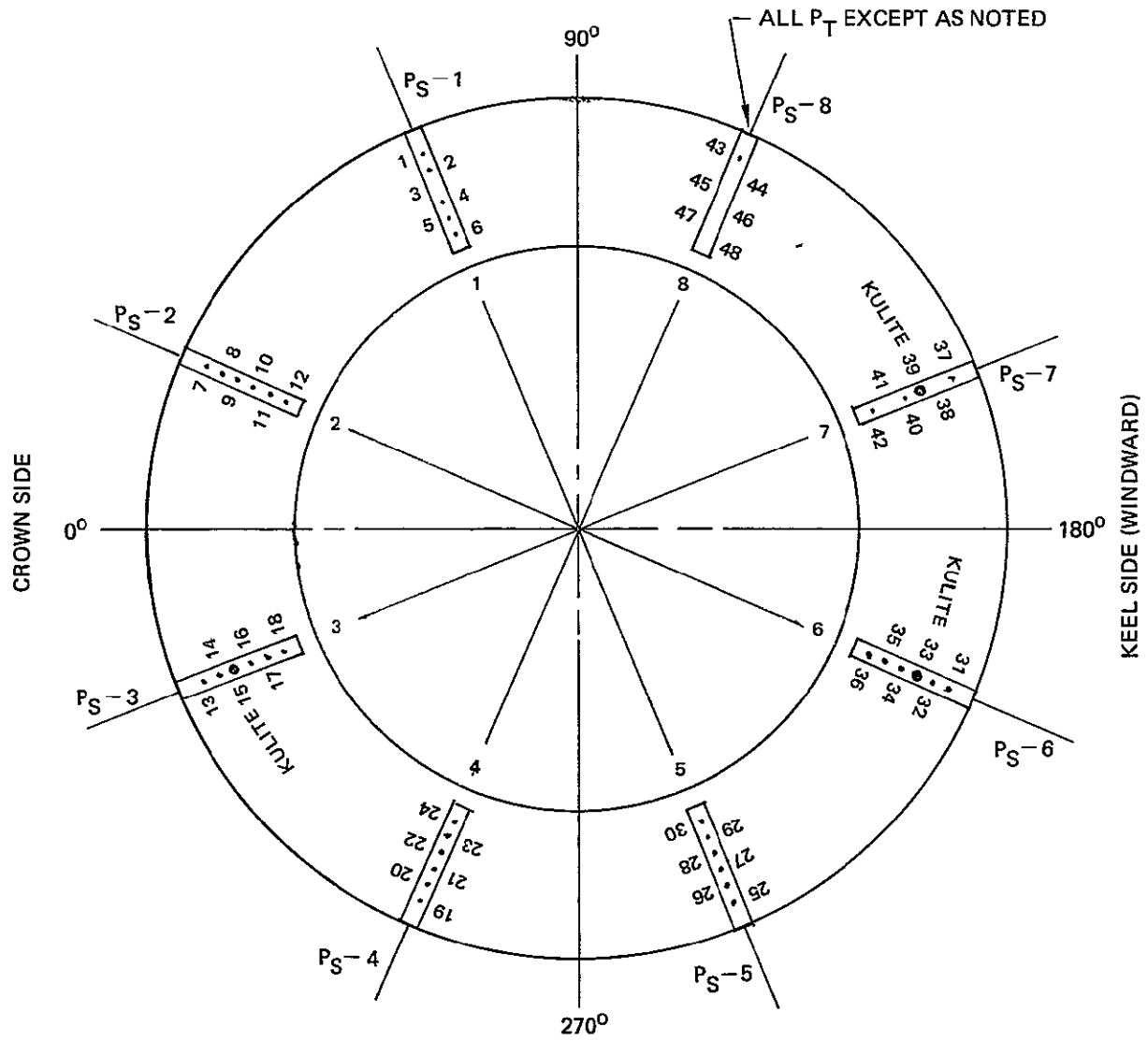


Figure 14 Compressor Face Instrumentation

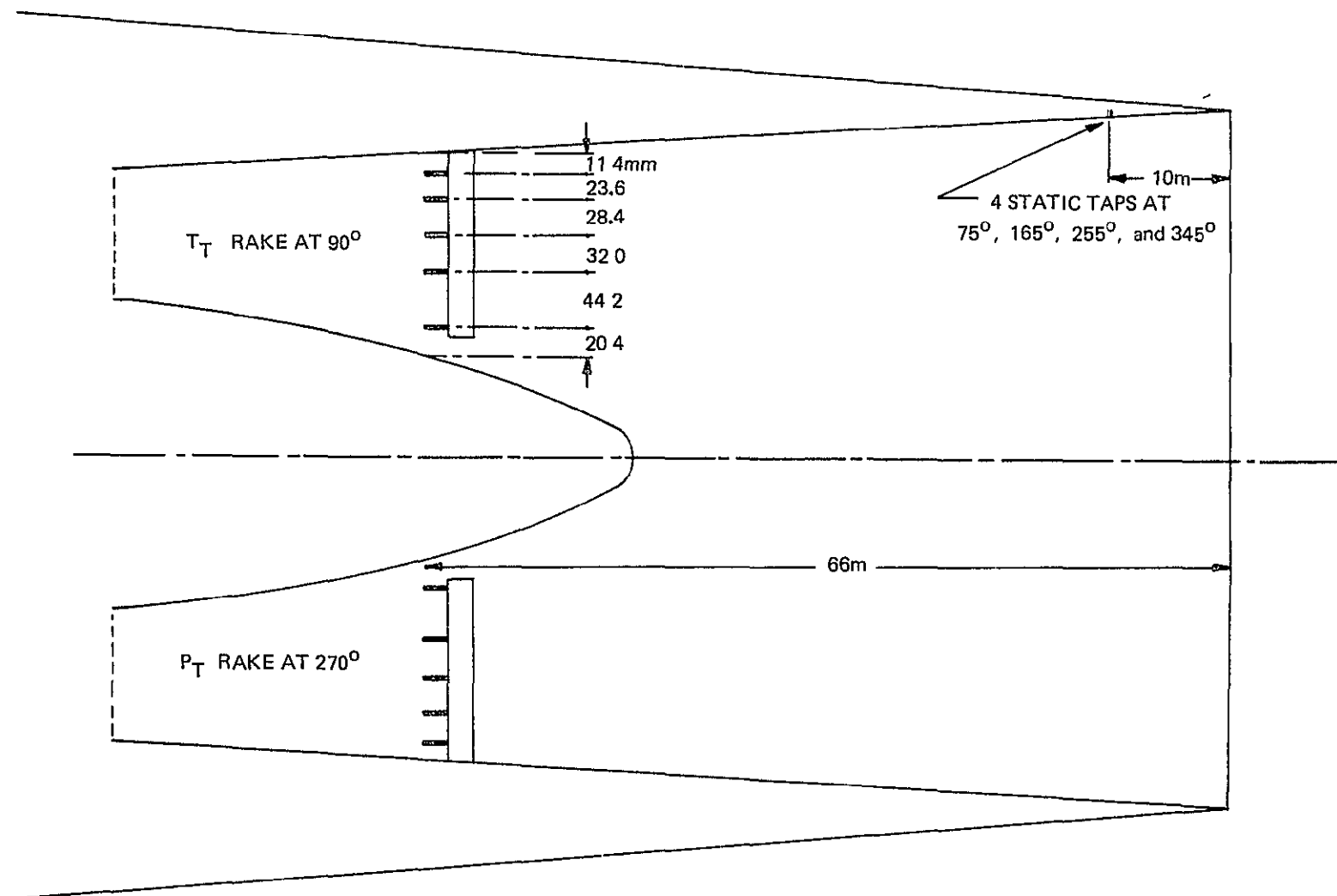


Figure 15 Primary Nozzle Instrumentation

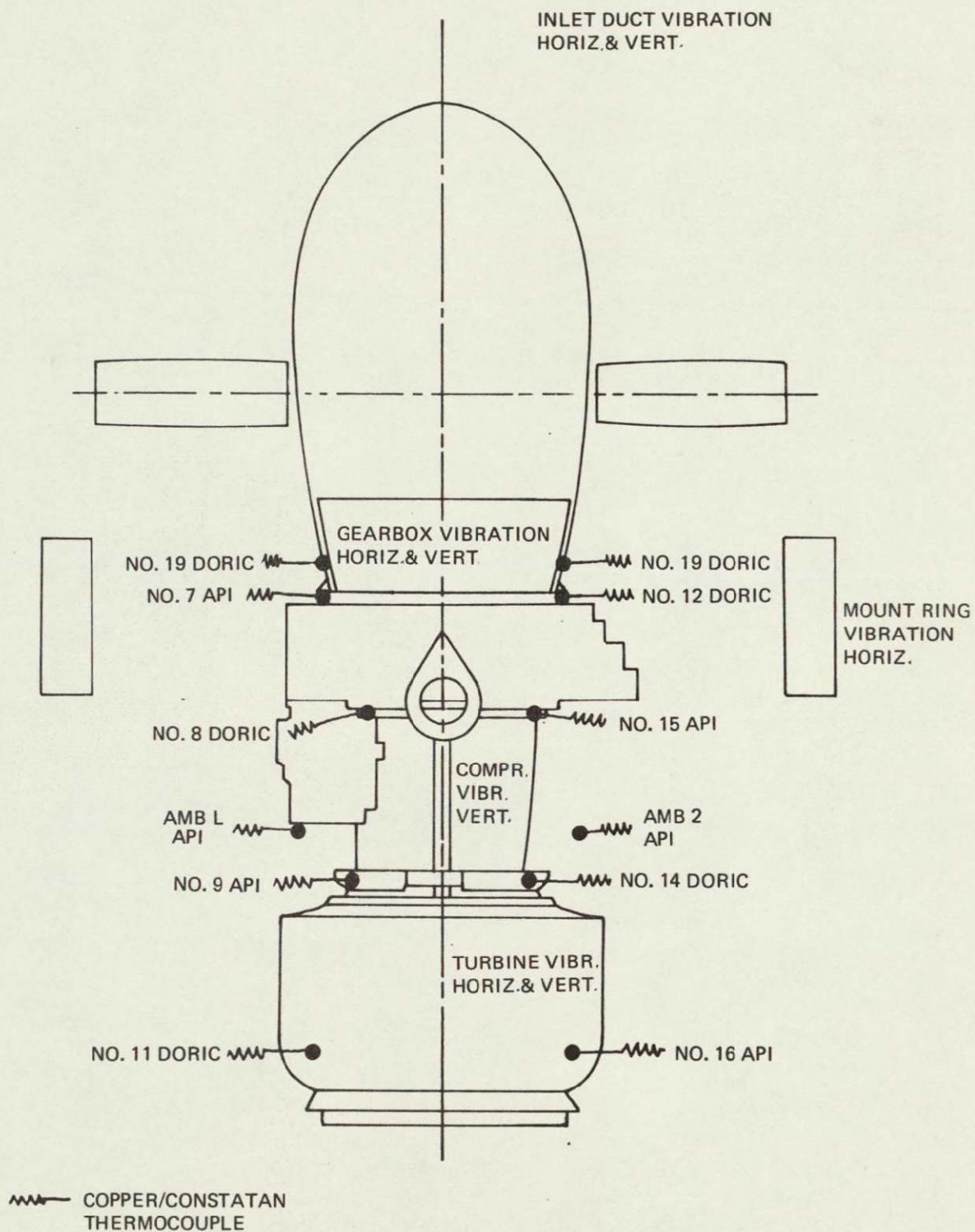


Figure 16. Temperature and Vibration Monitoring Locations



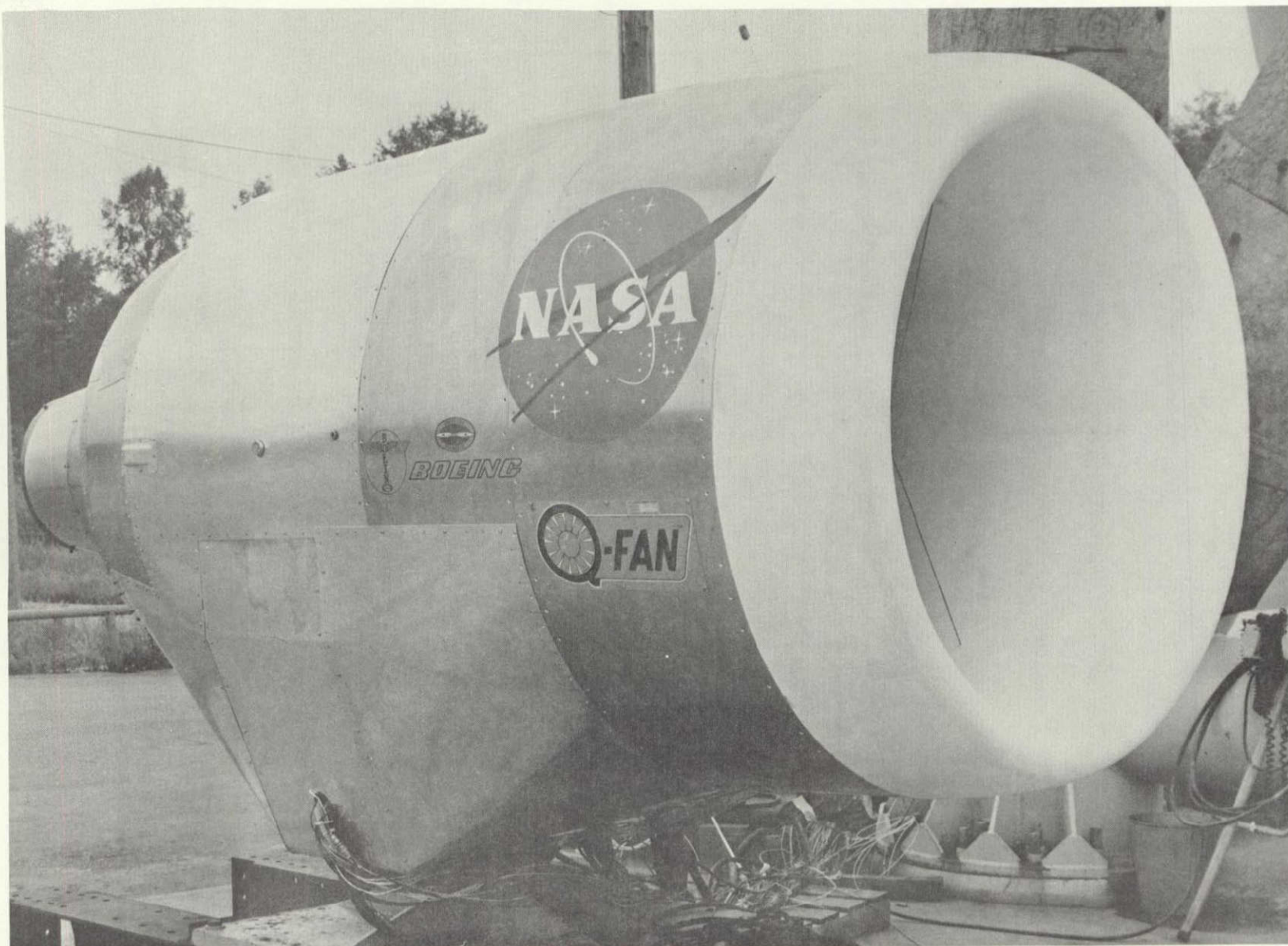


Figure 17. Static Test Installation



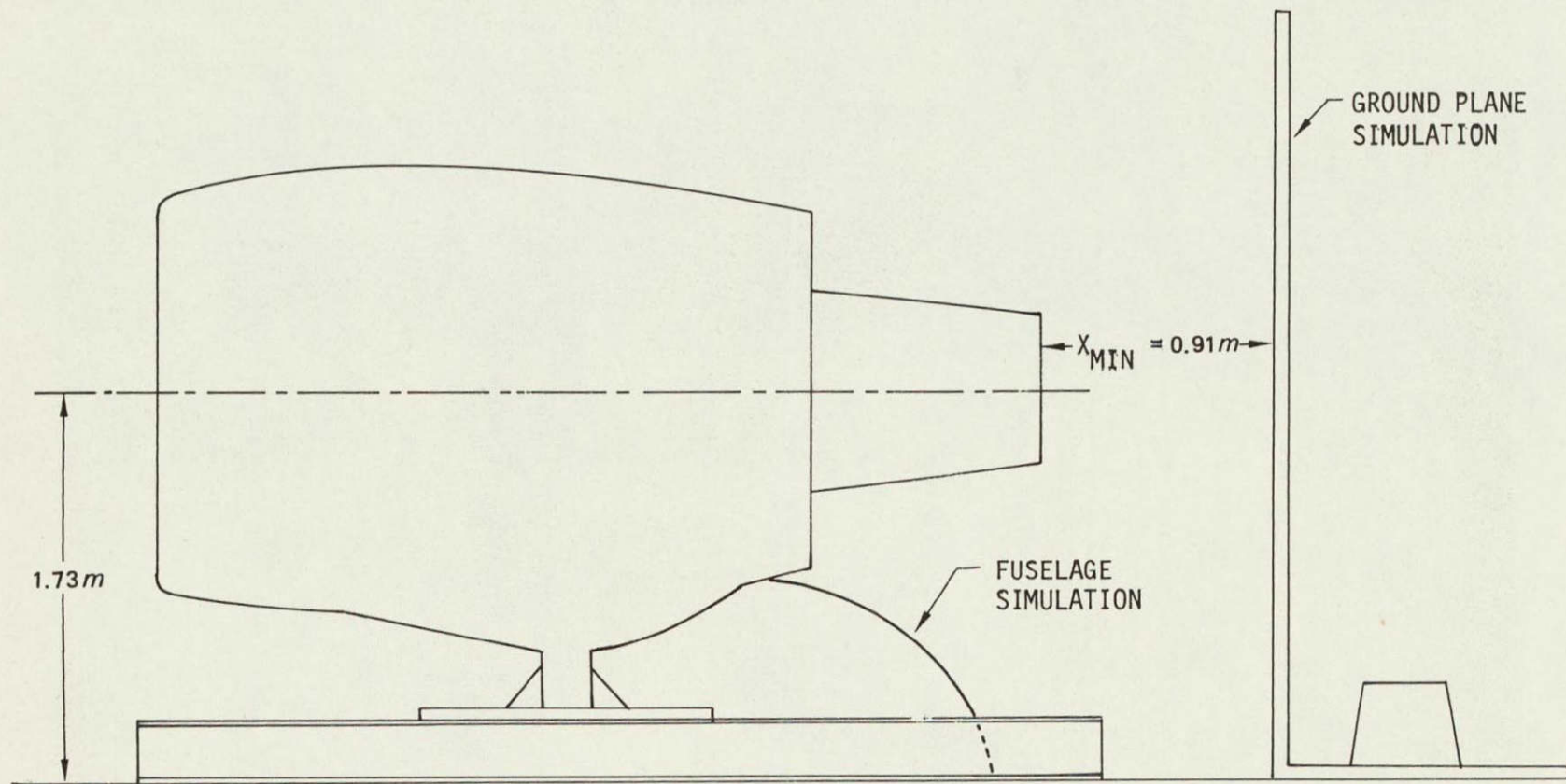


Figure 18. Static Test Installation Schematic

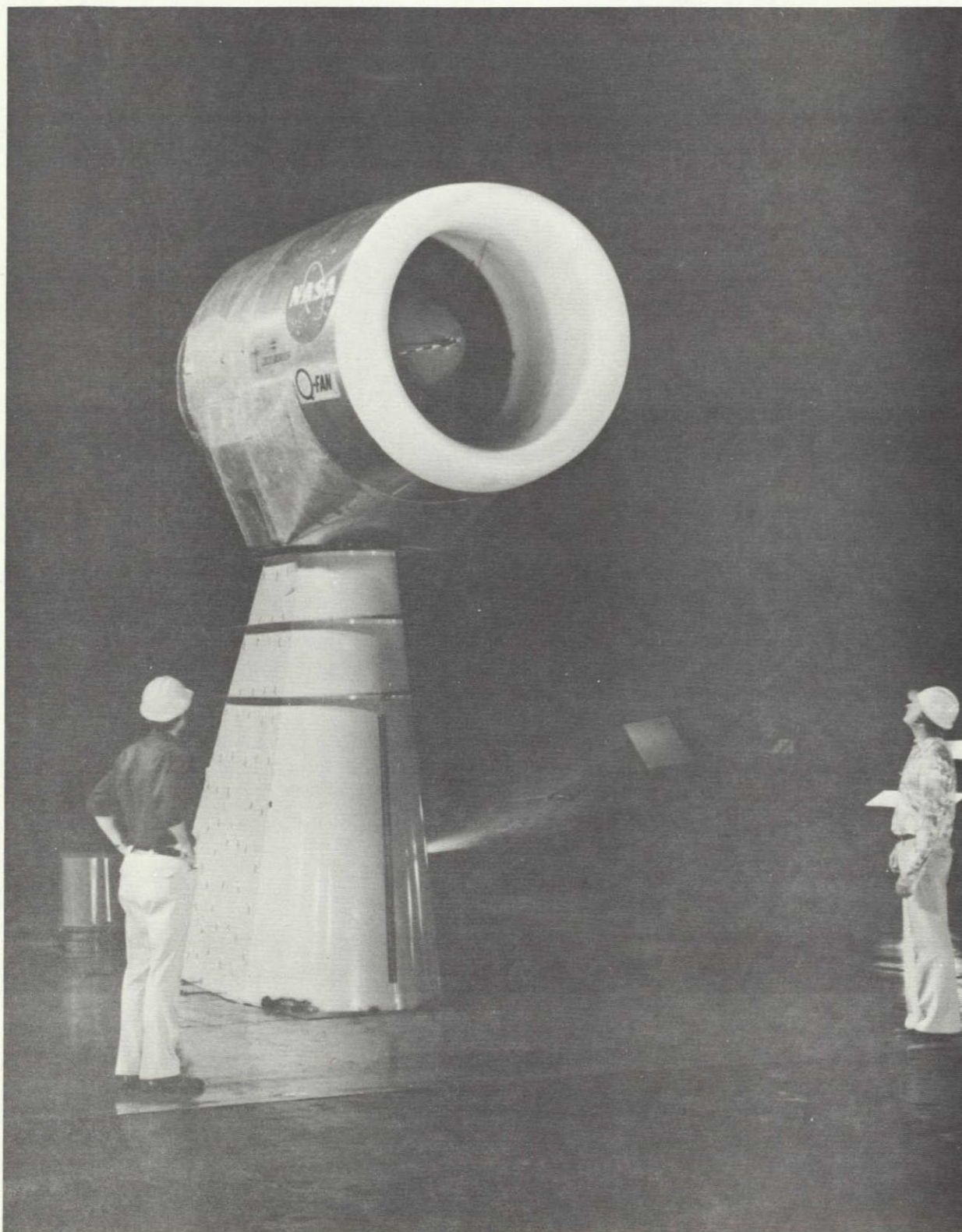


Figure 19. Nacelle Installed in 40- by 80-ft Wind Tunnel

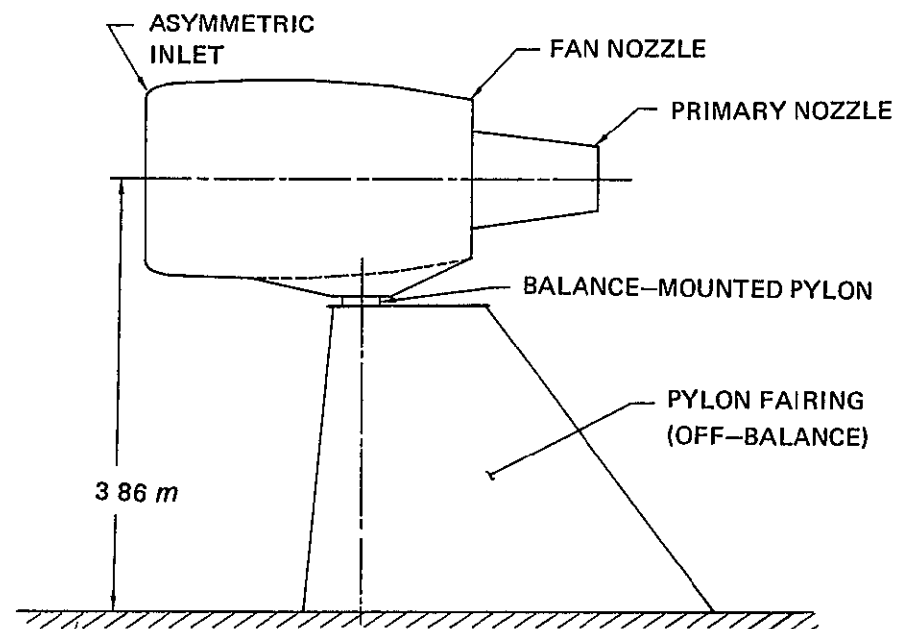
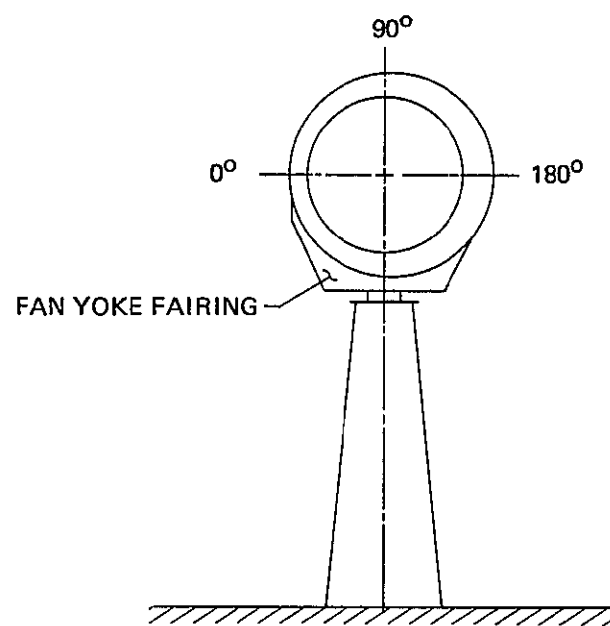


Figure 20 Wind Tunnel Installation Schematic

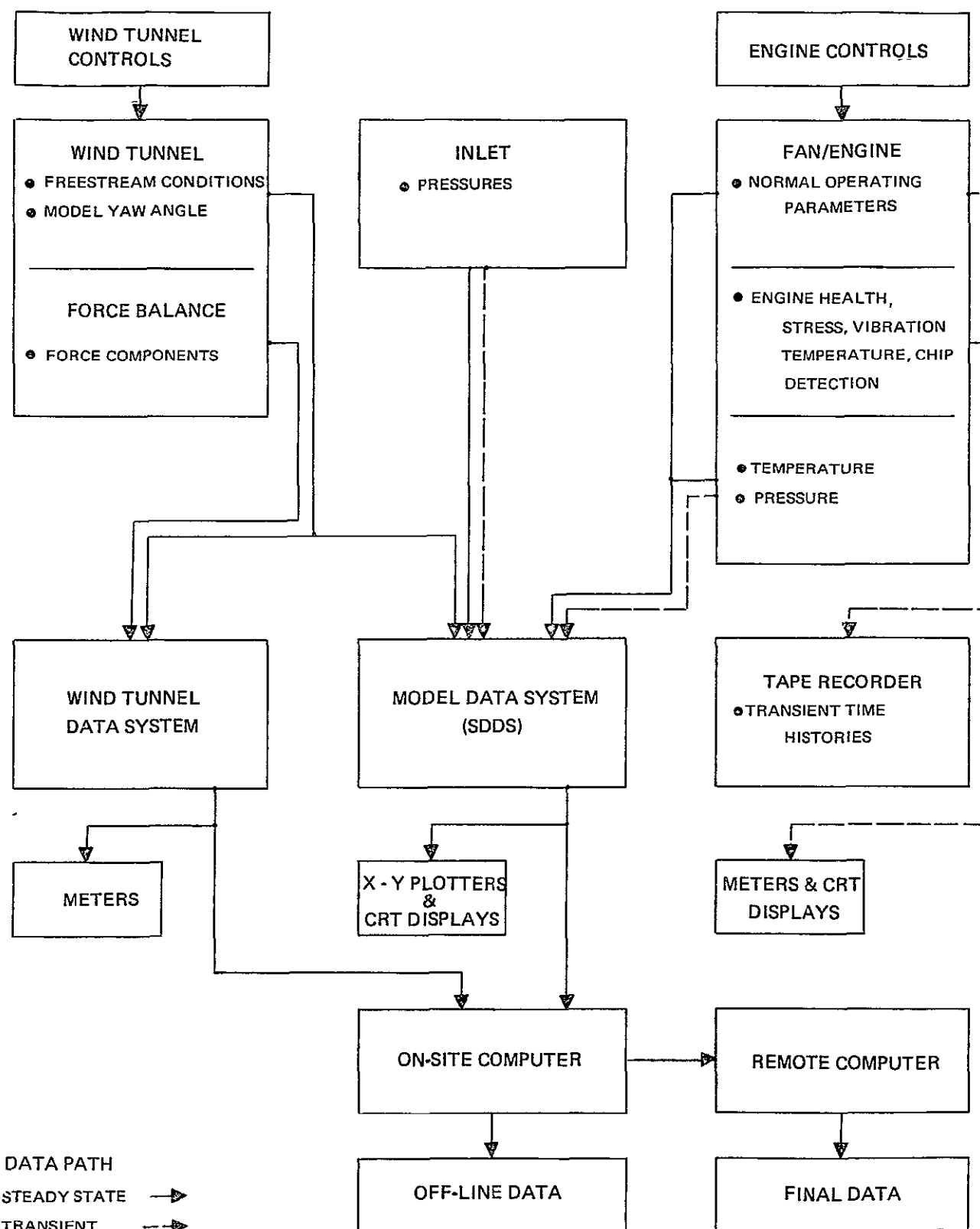


Figure 21. Data Acquisition and Reduction System Diagram

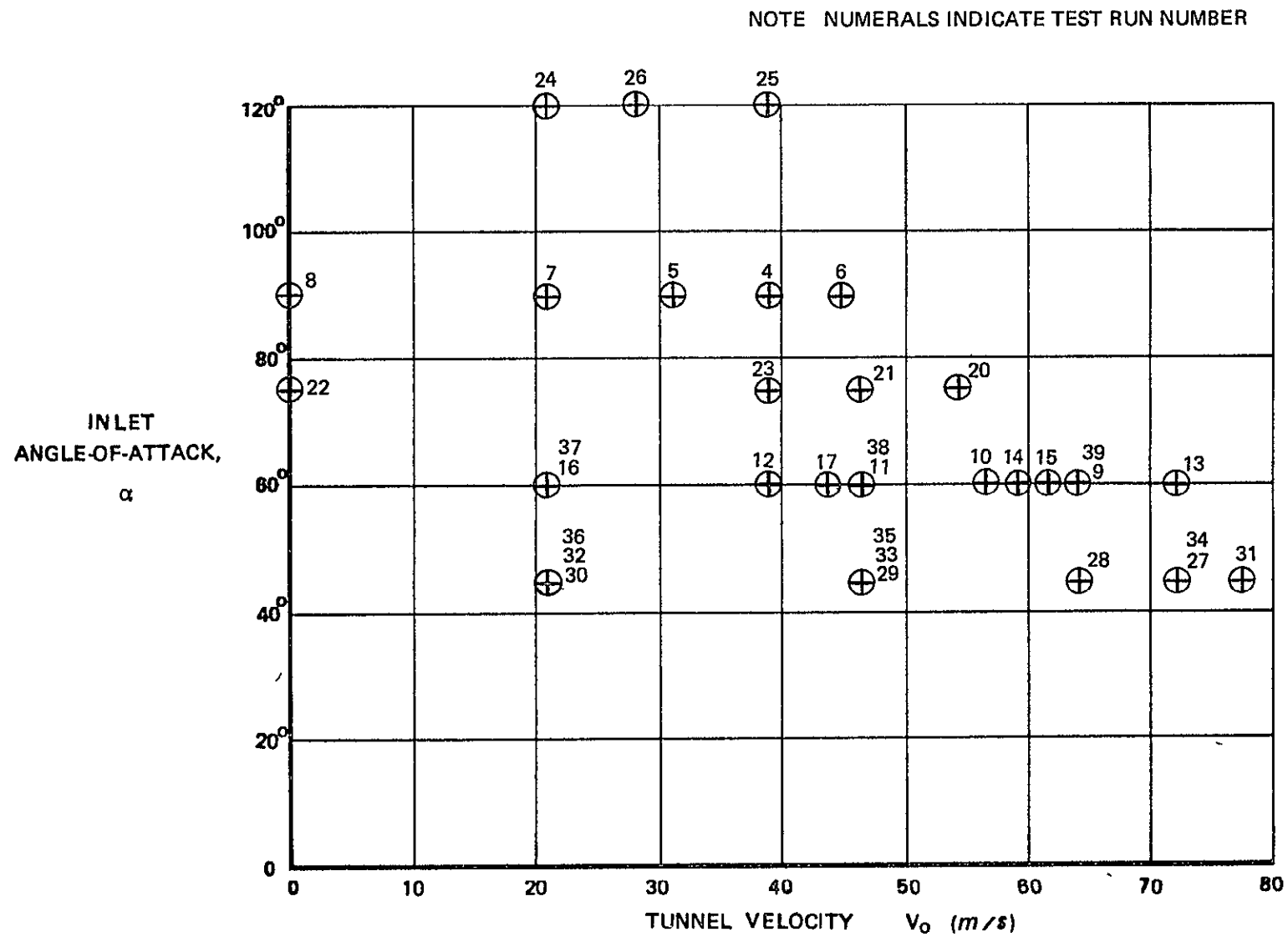


Figure 22.  $\frac{1}{4}$  Scale LCF Inlet Test Matrix

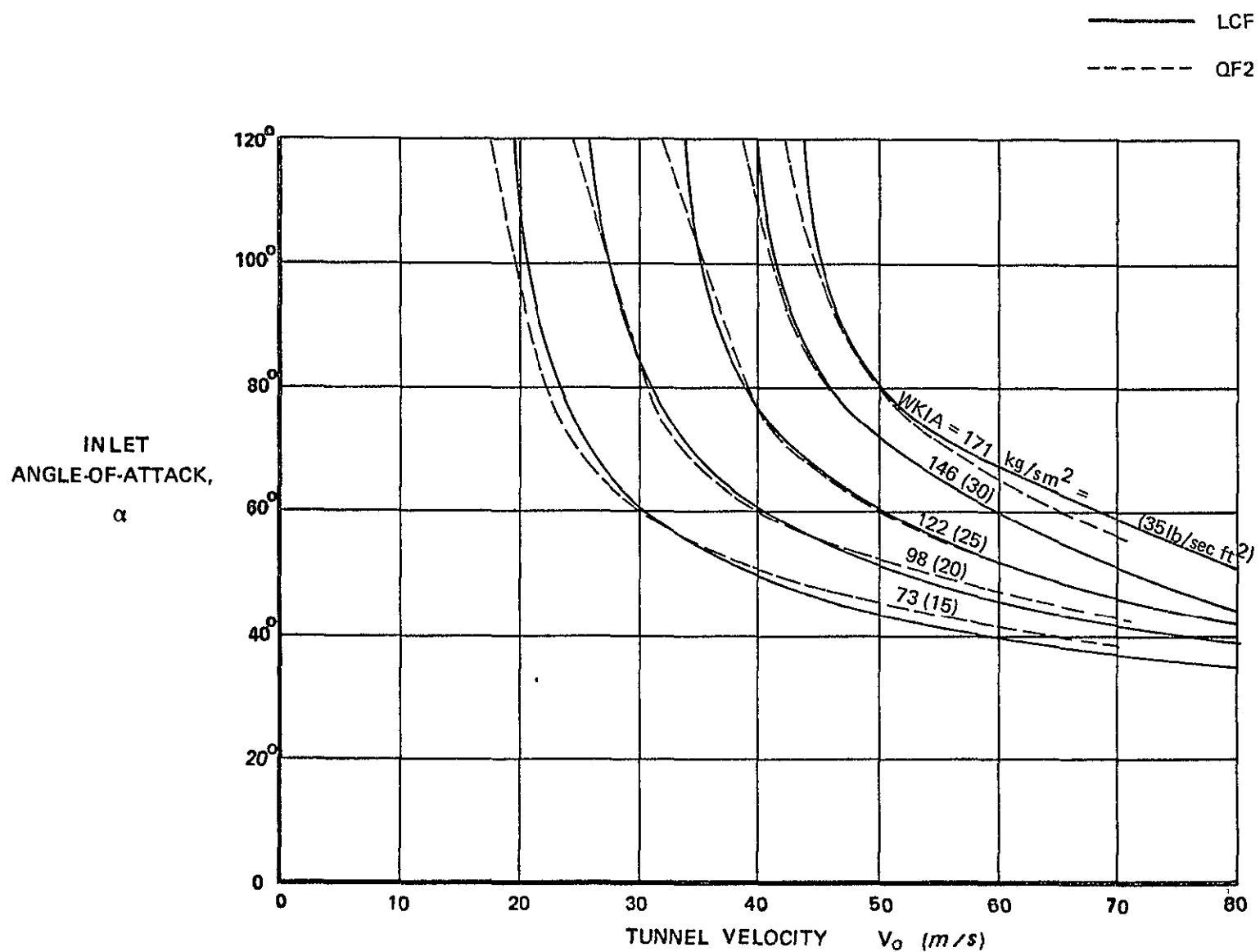


Figure 23 Separation Boundaries for the 1/4 Scale LCF and QF2 Inlets

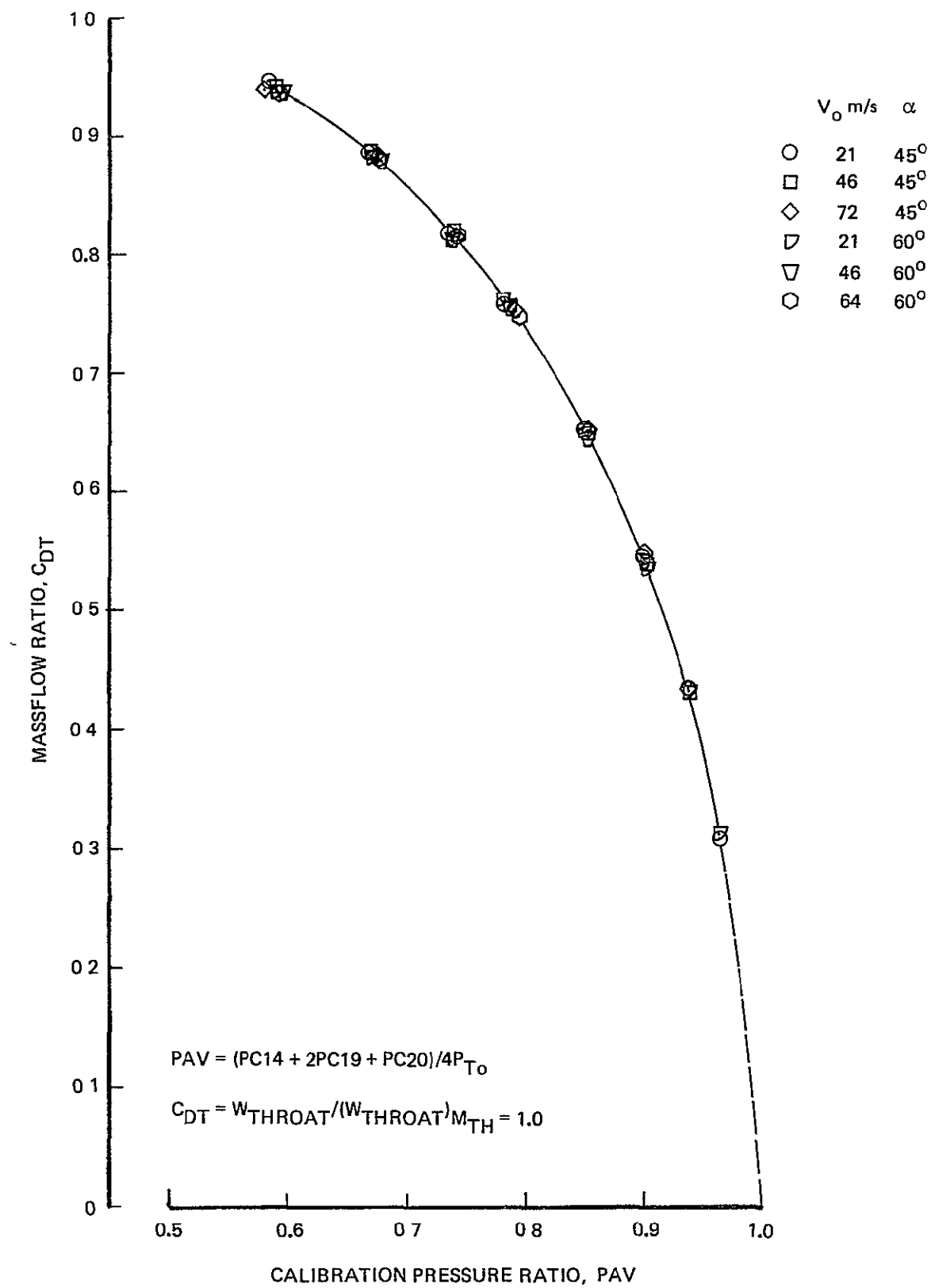


Figure 24 1/4 Scale LCF Inlet Flow Calibration

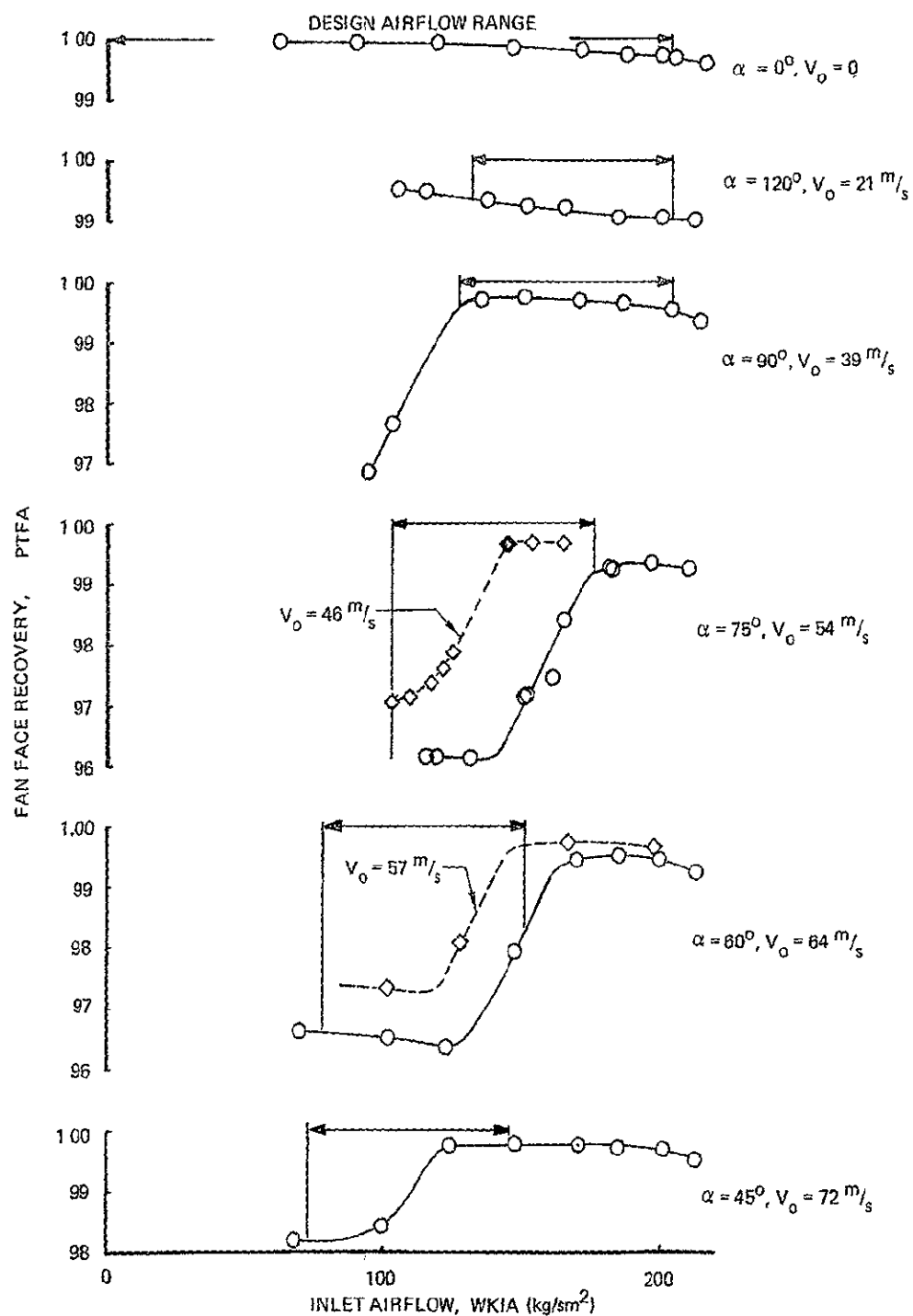


Figure 25 1/4 Scale LCF Inlet Recovery



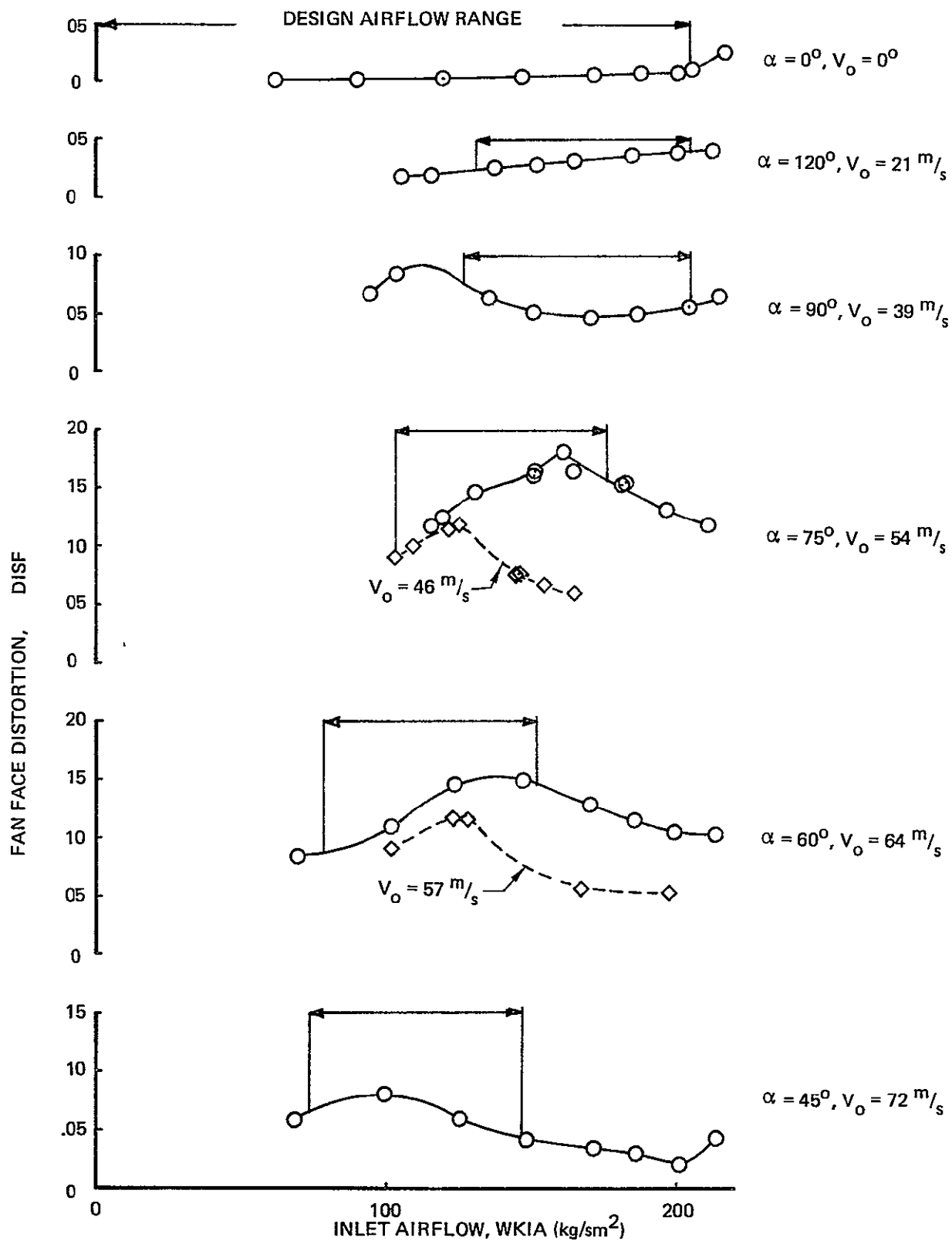


Figure 26. 1/4 Scale LCF Inlet Distortion

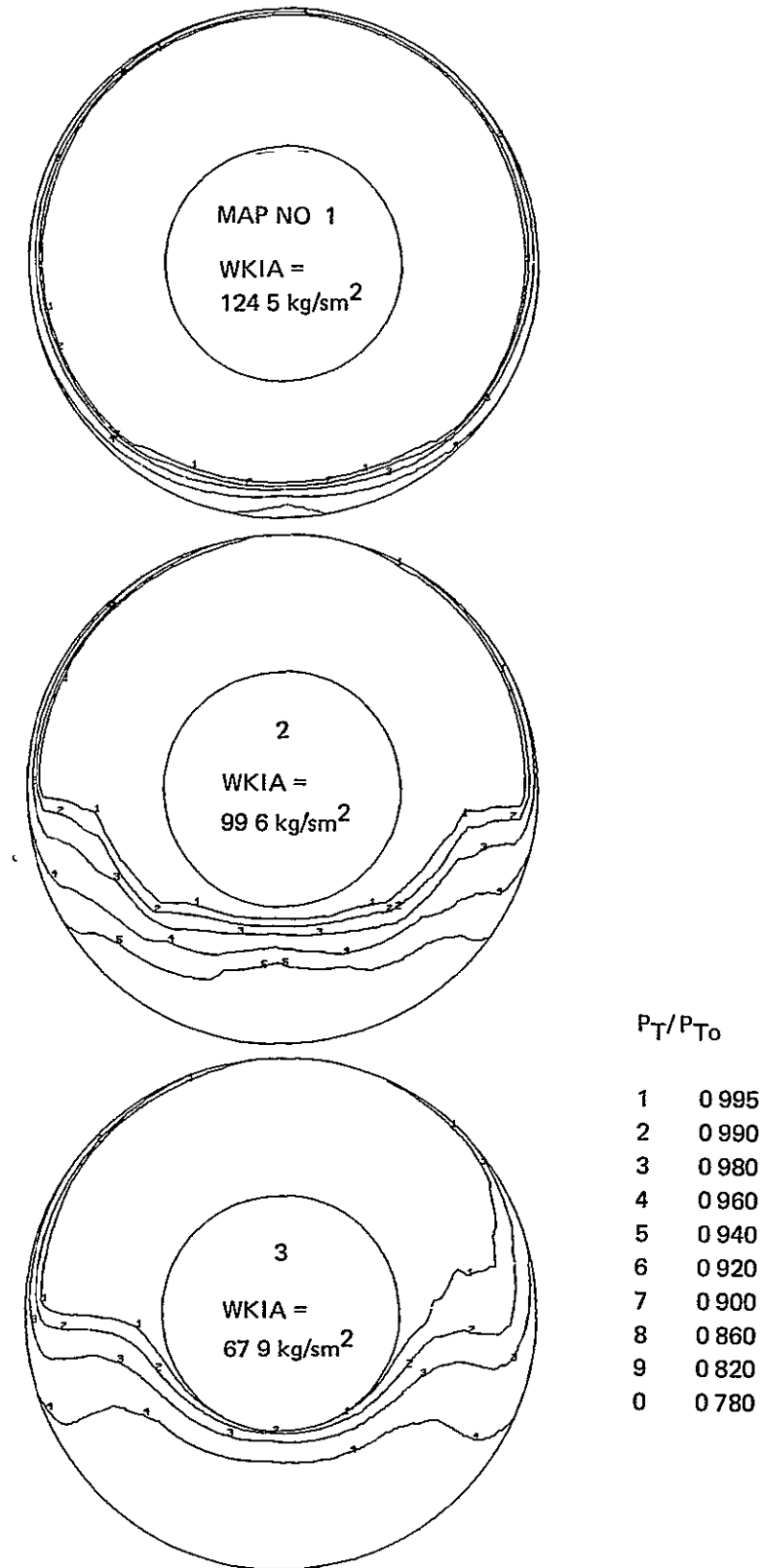
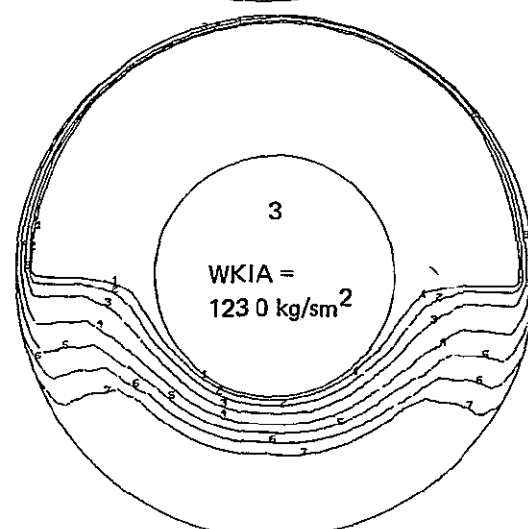
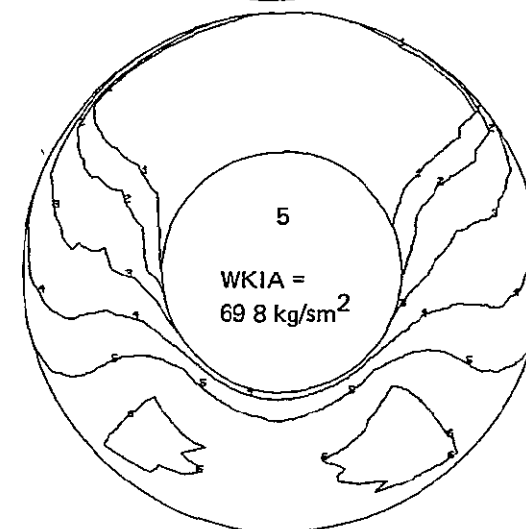
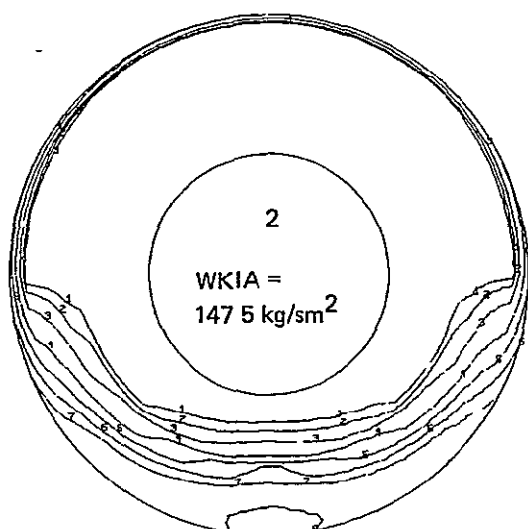
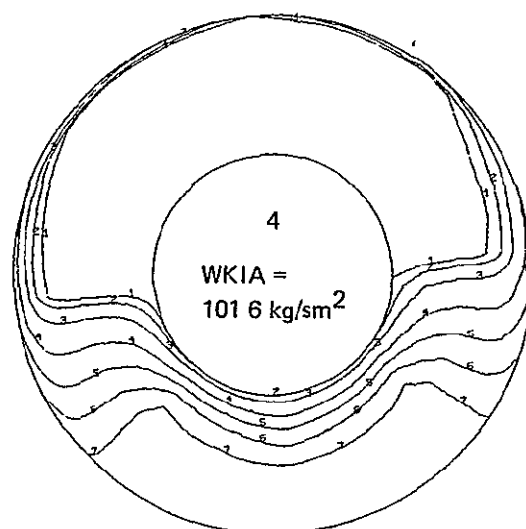
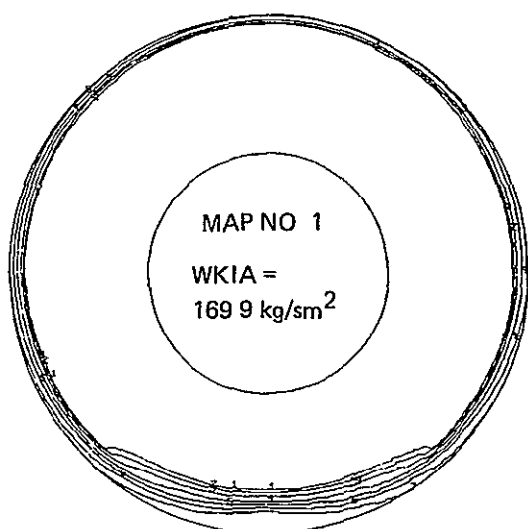


Figure 27 1/4 Scale Inlet Fan Face Total Pressure Maps,  $\alpha = 45^\circ$ ,  $V = 72$  m/s



$P_T/P_{To}$

1	0.995
2	0.990
3	0.980
4	0.960
5	0.940
6	0.920
7	0.900
8	0.860
9	0.820
0	0.780

Figure 28 ¼ Scale Inlet Fan Face Total Pressure Maps,  $\alpha = 60^\circ$ ,  $V = 64$  m/s

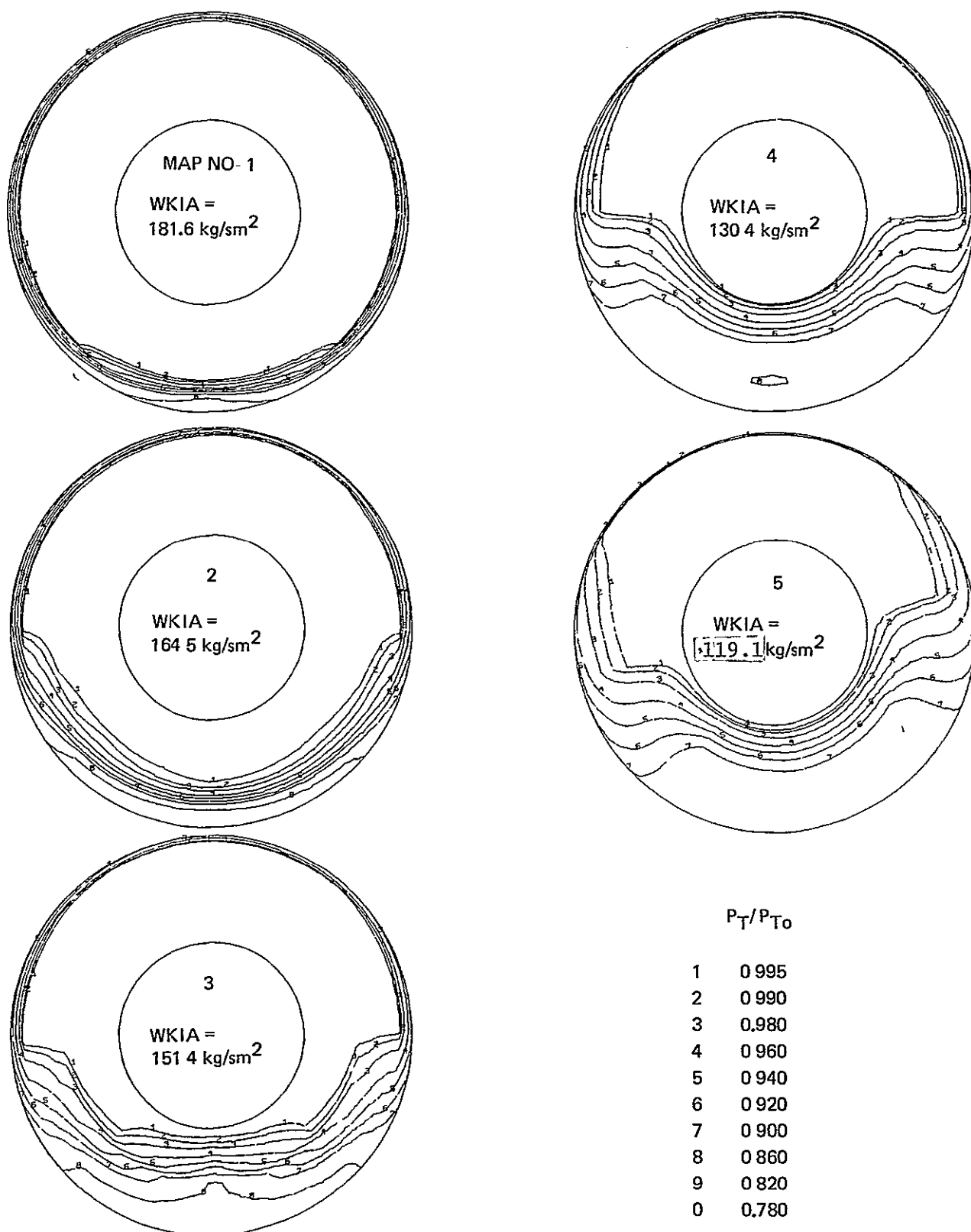


Figure 29. ¼ Scale Inlet Fan Face Total Pressure Maps,  $\alpha = 75^\circ$ ,  $V = 54$  m/s

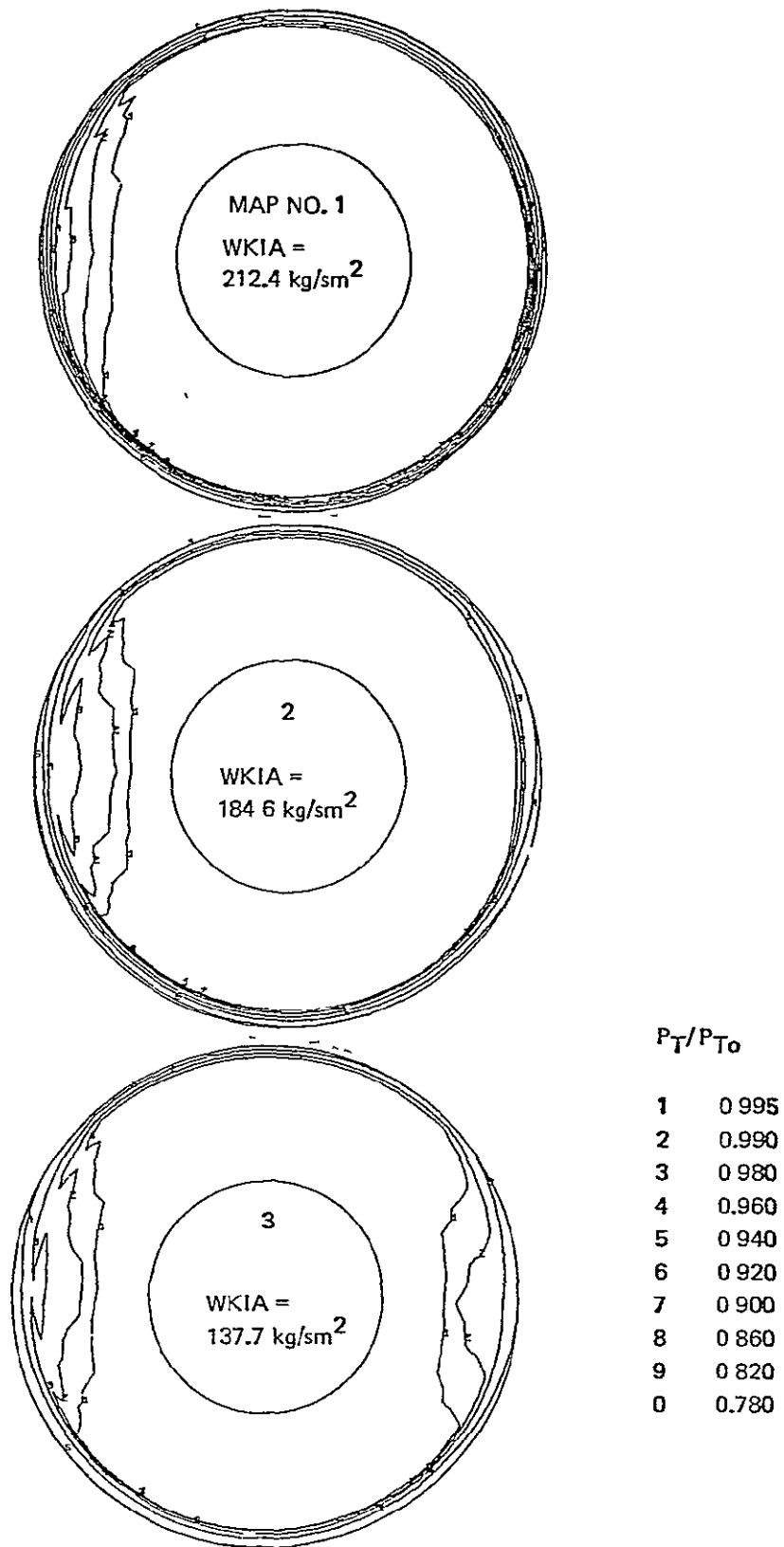


Figure 30. 1/4 Scale Inlet Fan Face Total Pressure Maps,  $\alpha=120^\circ$ ,  $V=21$  m/s

N2 \ $\beta$	39°	43°	47°	51.8°	56°
8,000	b	a	a	b	a
10,000	a	a	a	a	a
12,000	b	a	a	b	a
14,000	a	a	a	a	a
15,000	b	a	a	b	b
16,000 (MAX.)	b	a	a	b	

a: Test points without ground plane. RUNS 2-7

b: Test points with and without ground plane. RUNS 8-20

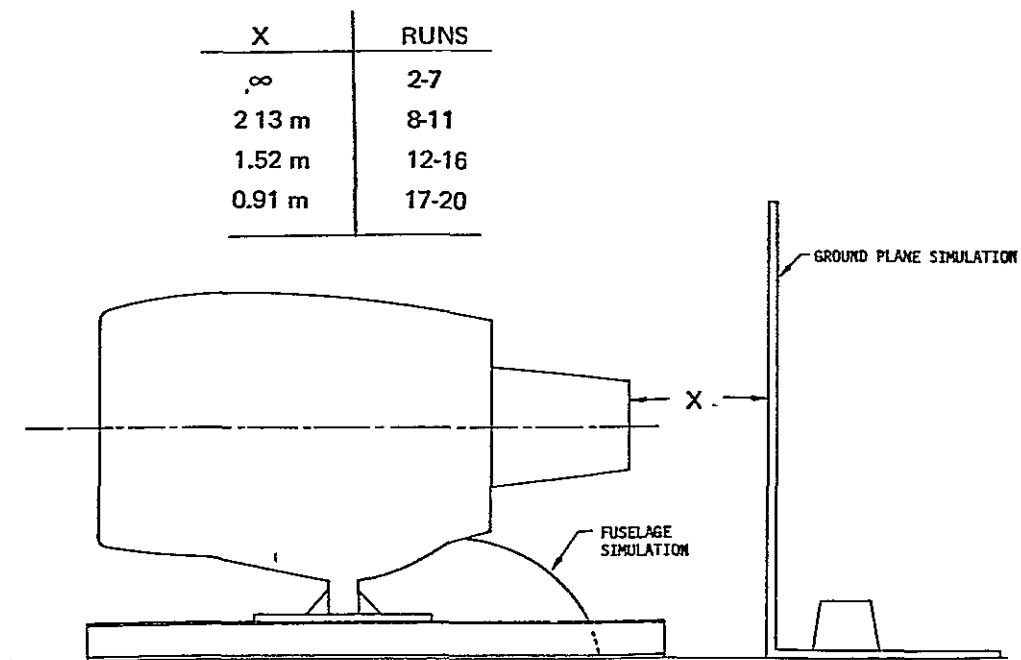


Figure 31. Test Matrix for Static Testing

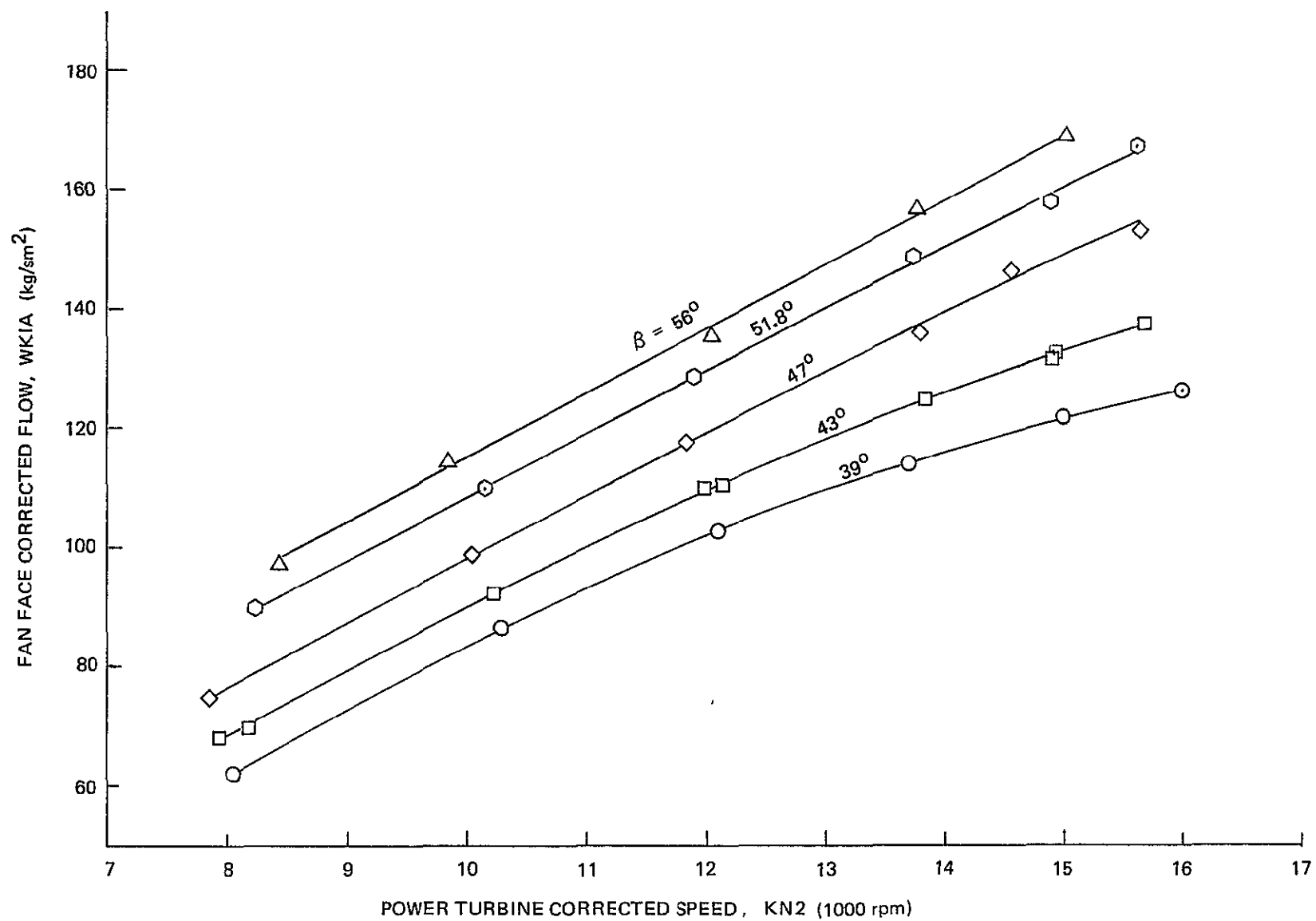


Figure 32 Inlet Airflow vs. Turbine Speed and Fan Blade Angle

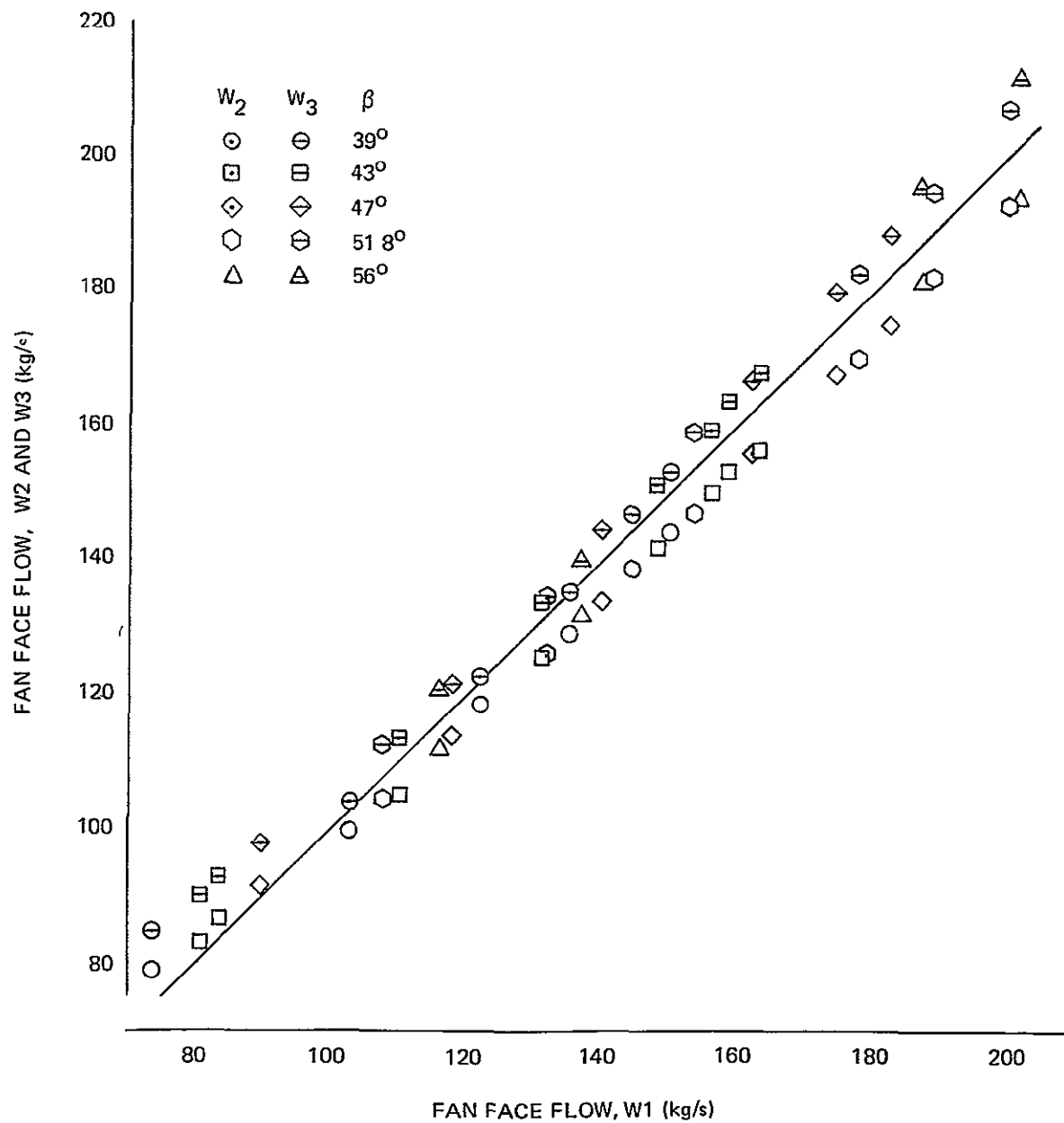


Figure 33 Comparison of Inlet Airflow Measurement Methods



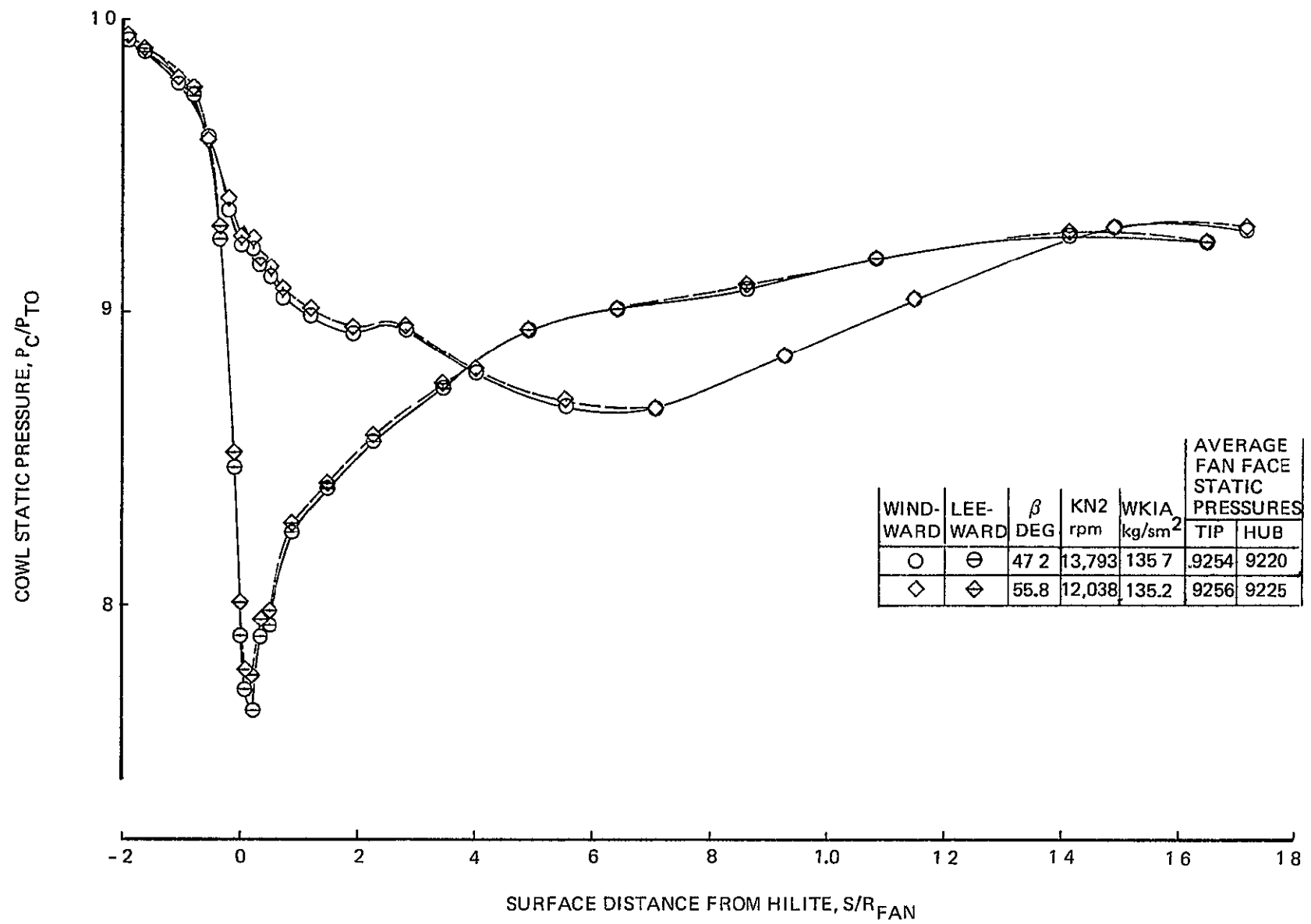


Figure 34 Comparison of Cowl Static Pressure Distributions

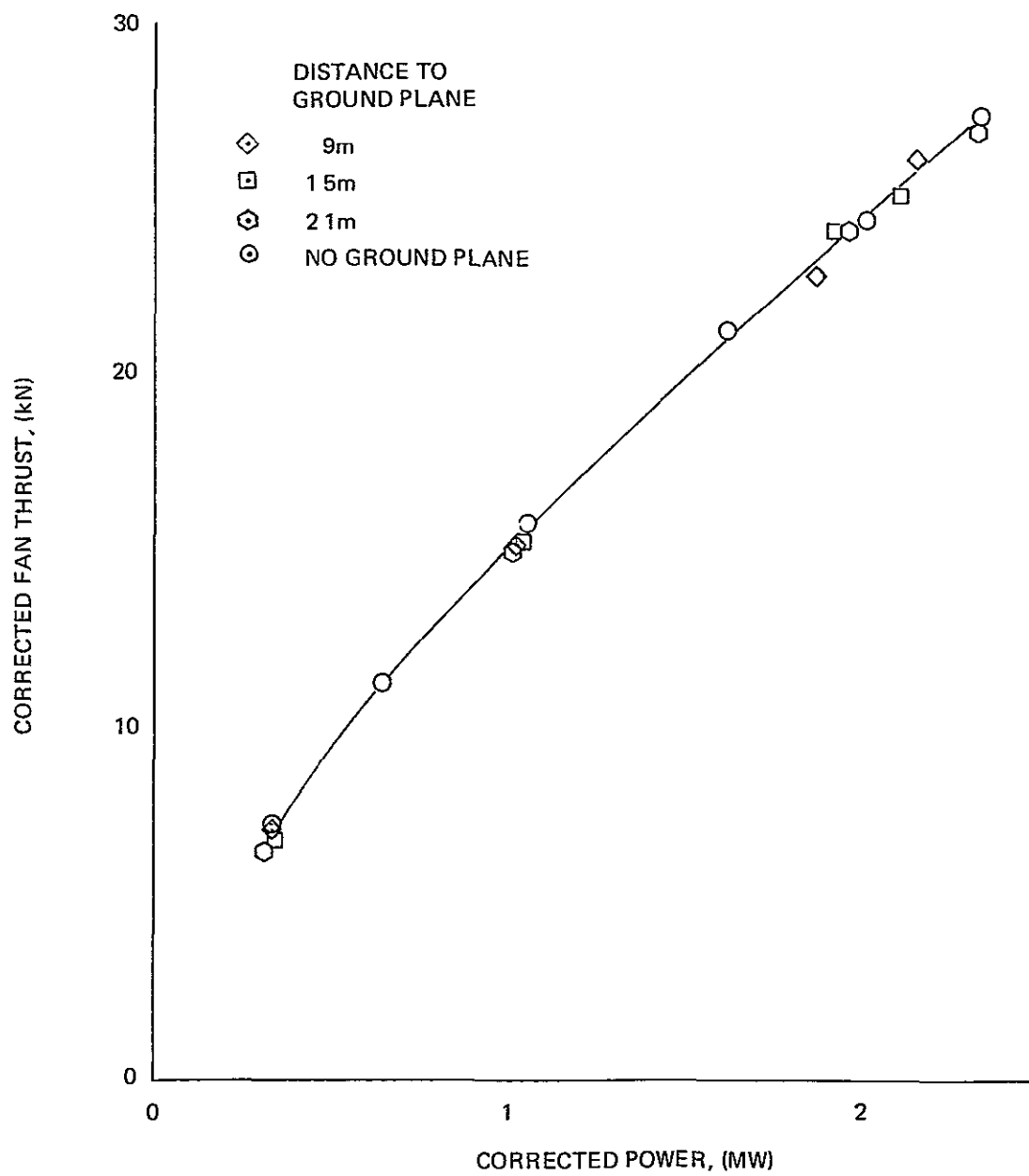


Figure 35 Fan Thrust Vs. Power,  $\beta = 51.8^\circ$  Static Test

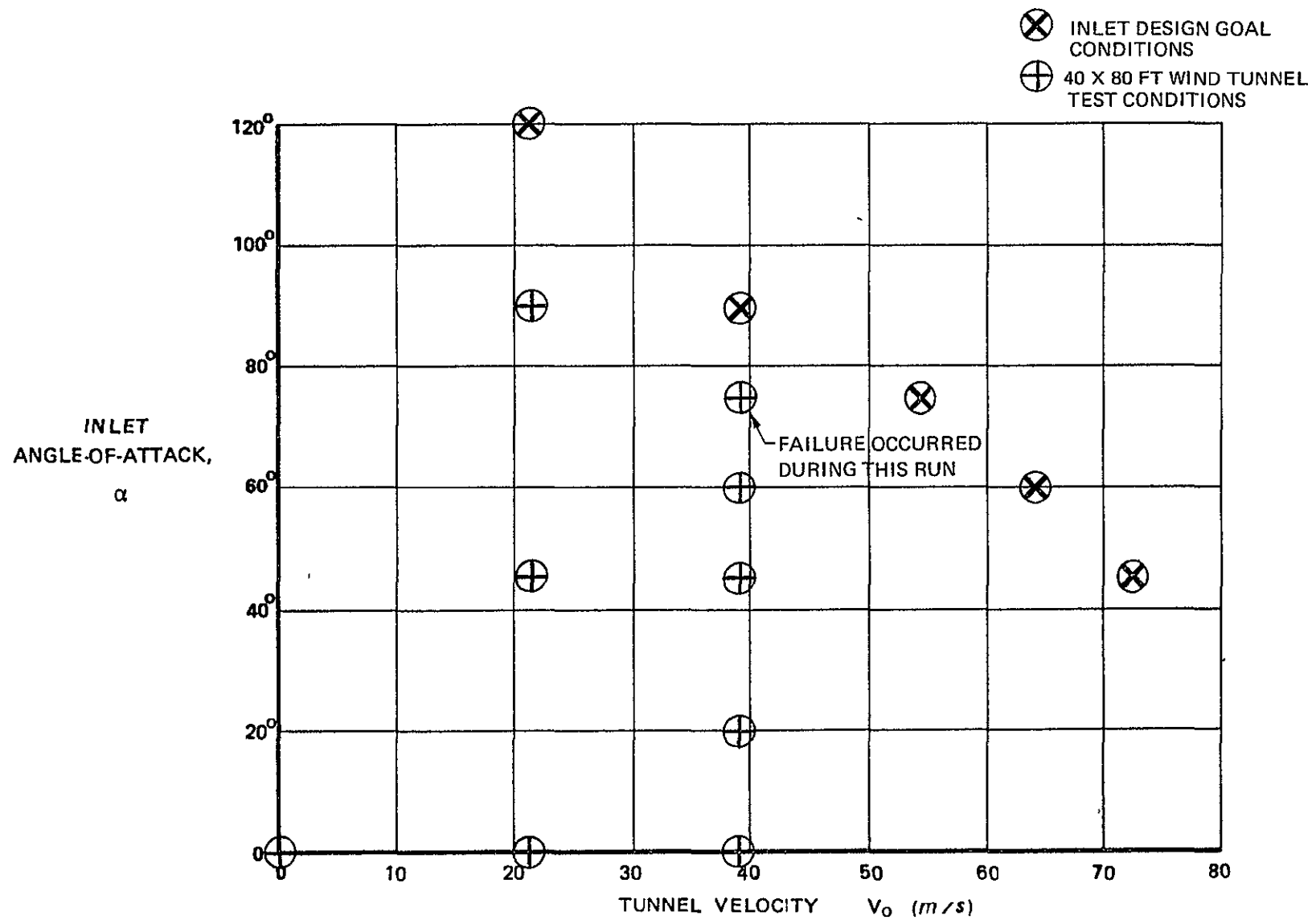


Figure 36 Design and Test Conditions

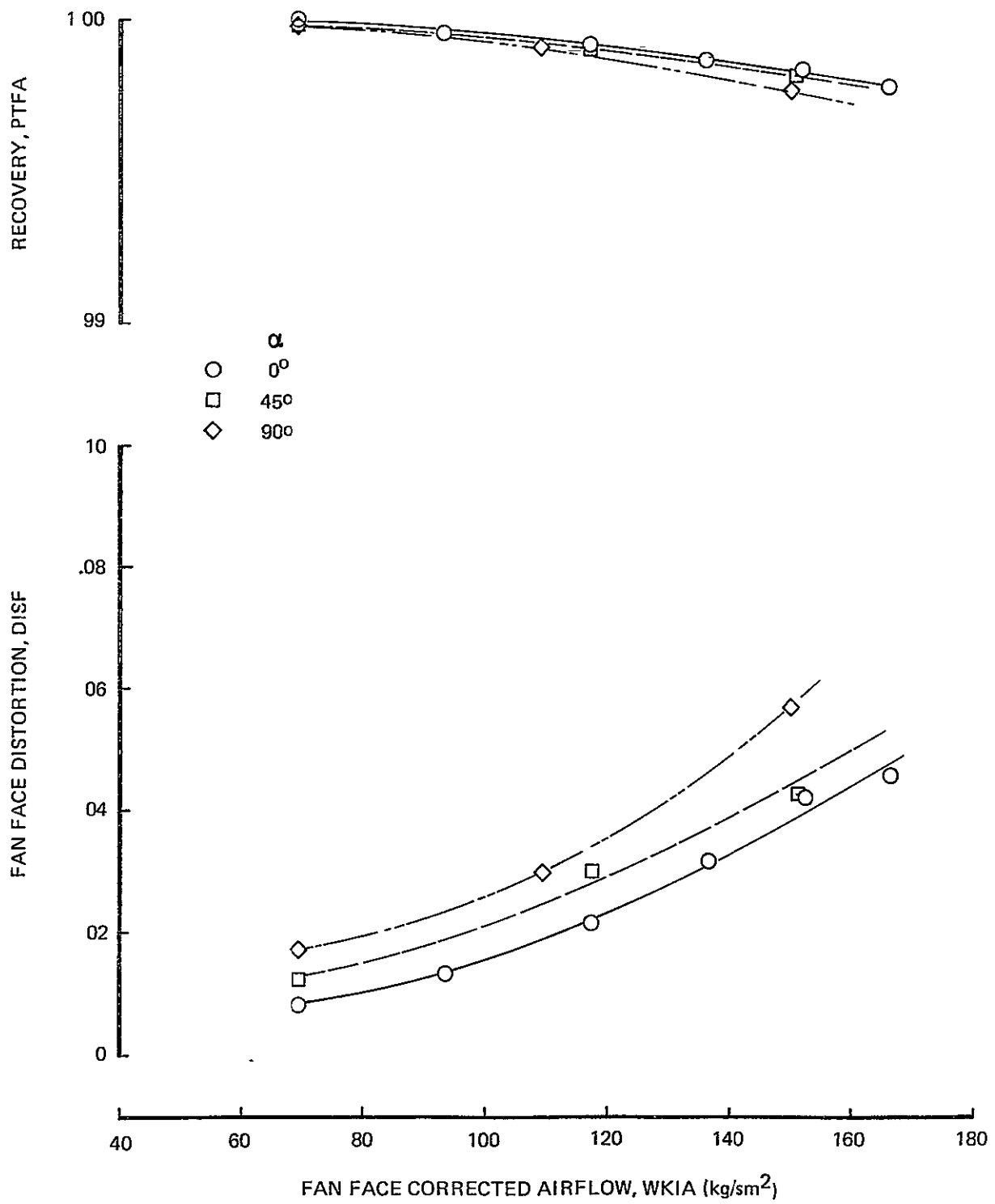


Figure 37 LCF Inlet Performance  $V_0 = 21 \text{ m/s}$

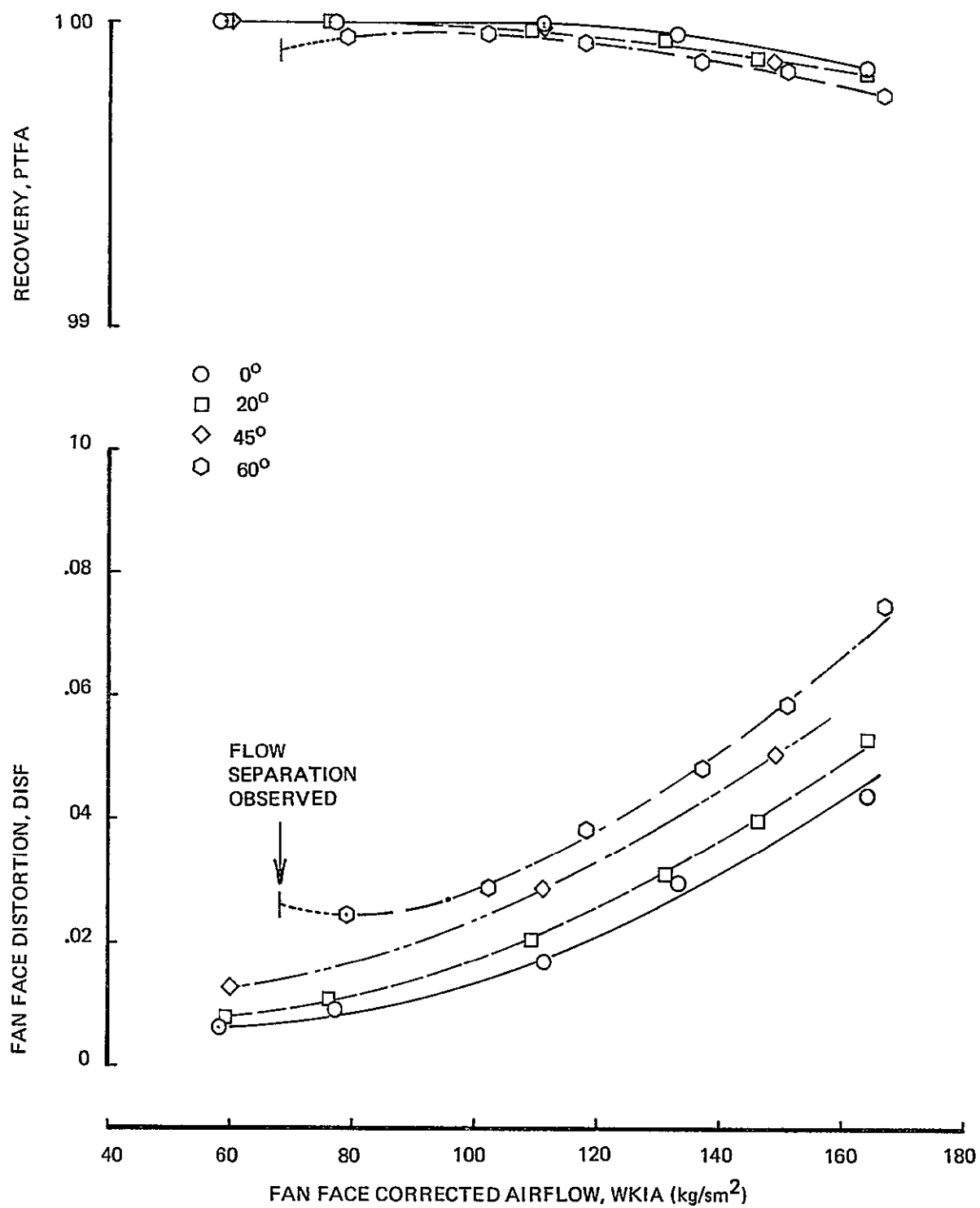


Figure 38. LCF Inlet Performance  $V_0 = 39 \text{ m/s}$

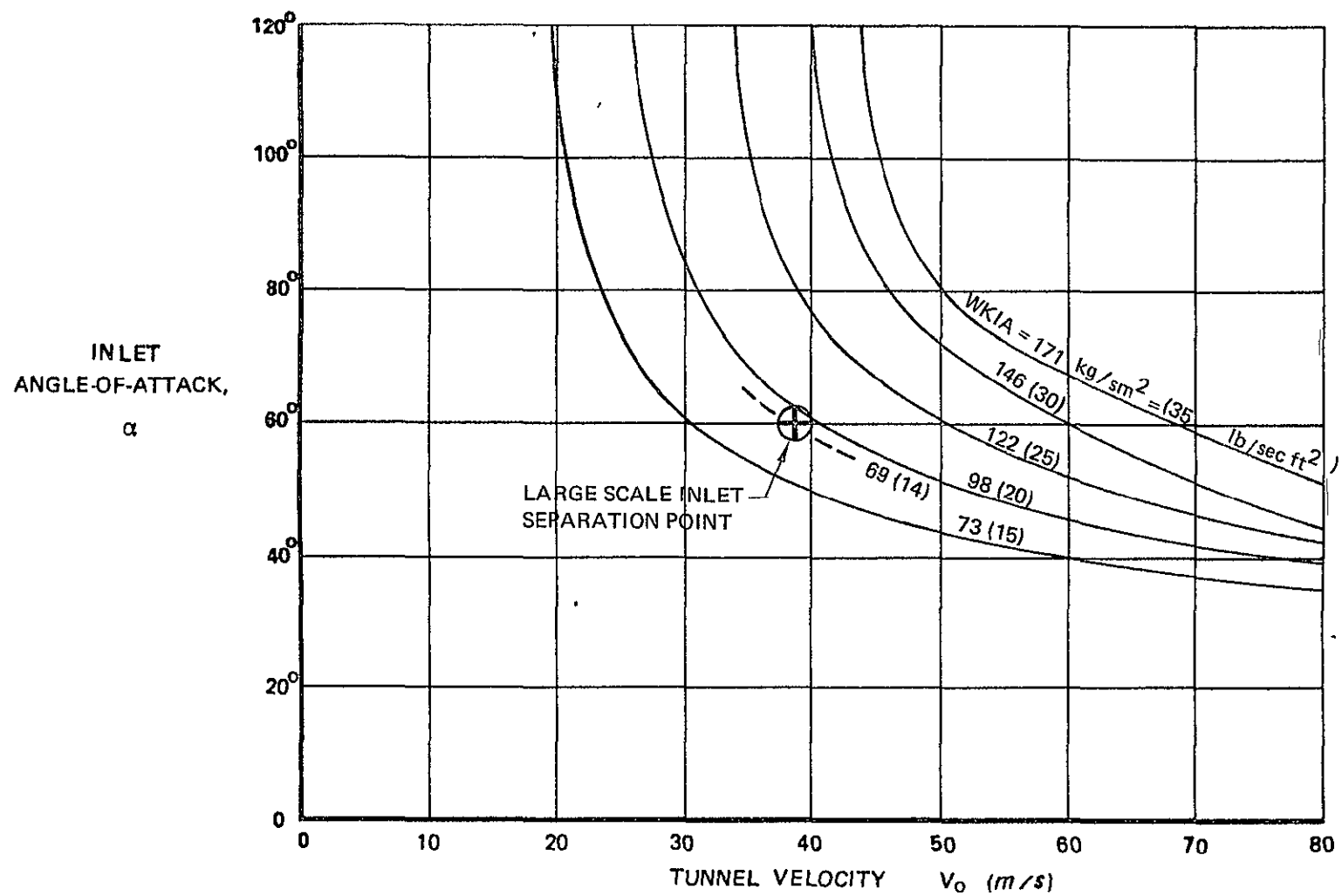


Figure 39. Separation Boundaries for Small Scale Inlet

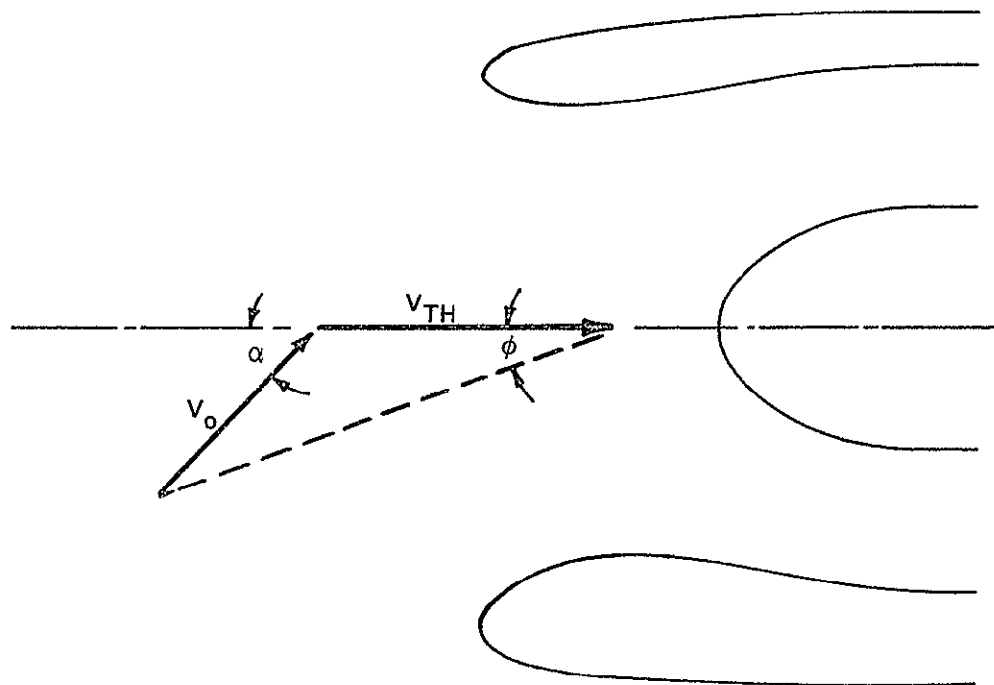


Figure 40. Empirical Separation Index

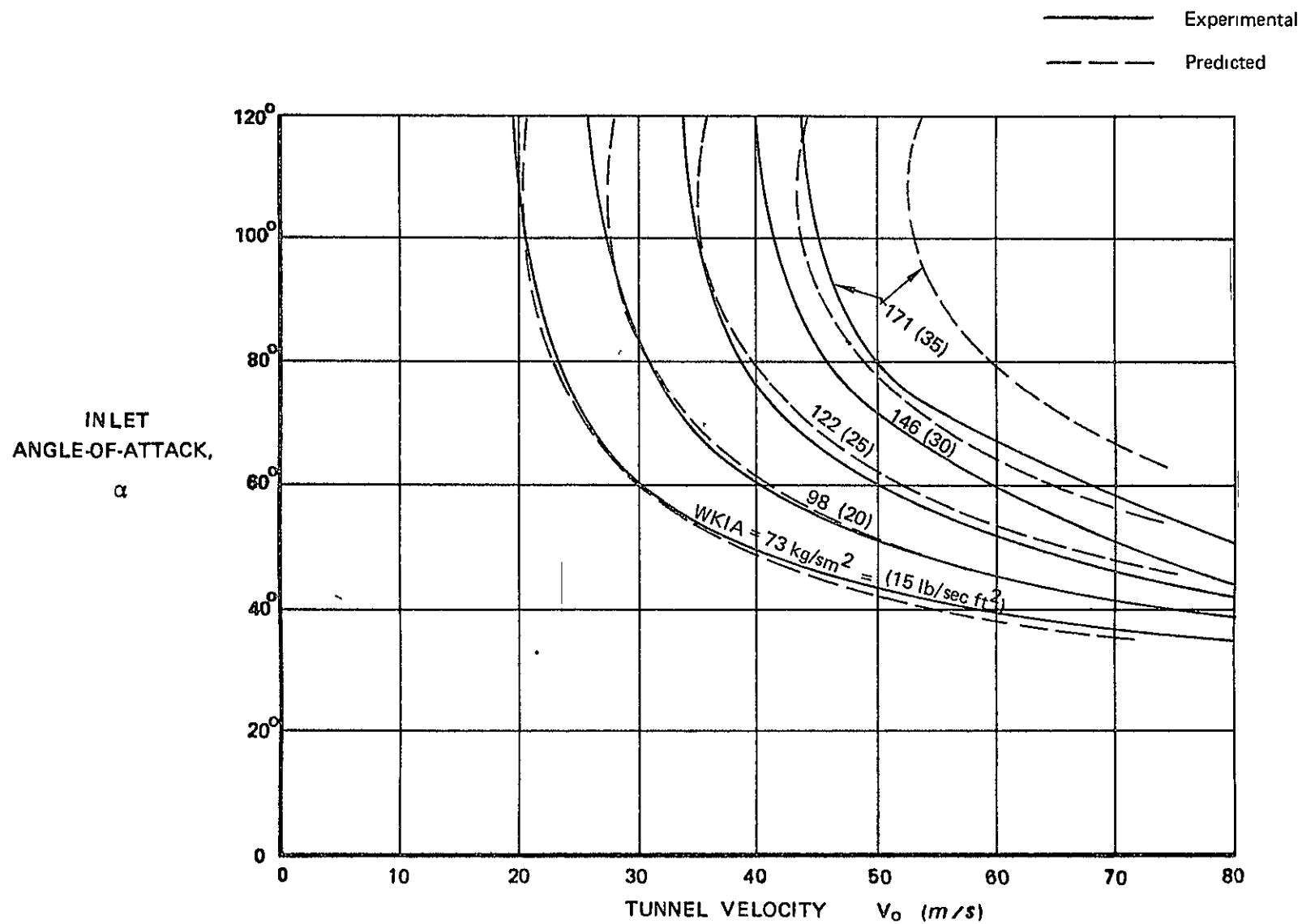


Figure 41 Experimental Separation Boundaries for 1/4 Scale Inlet and Predicted Separation Boundaries Using  $\phi = 18.2^\circ$



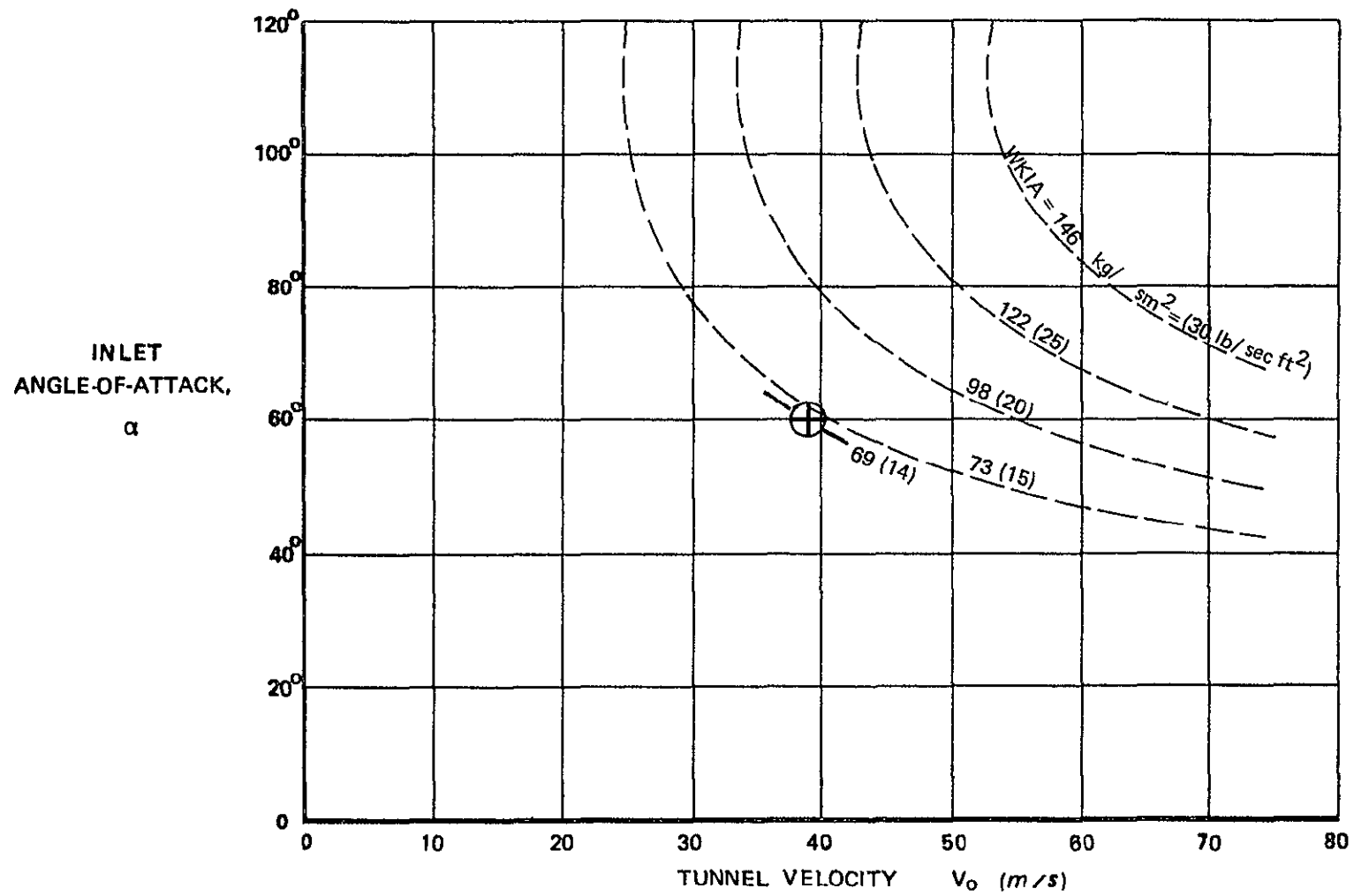


Figure 42 Predicted Separation Boundaries for Large Scale Inlet,  $\phi = 22.4^\circ$

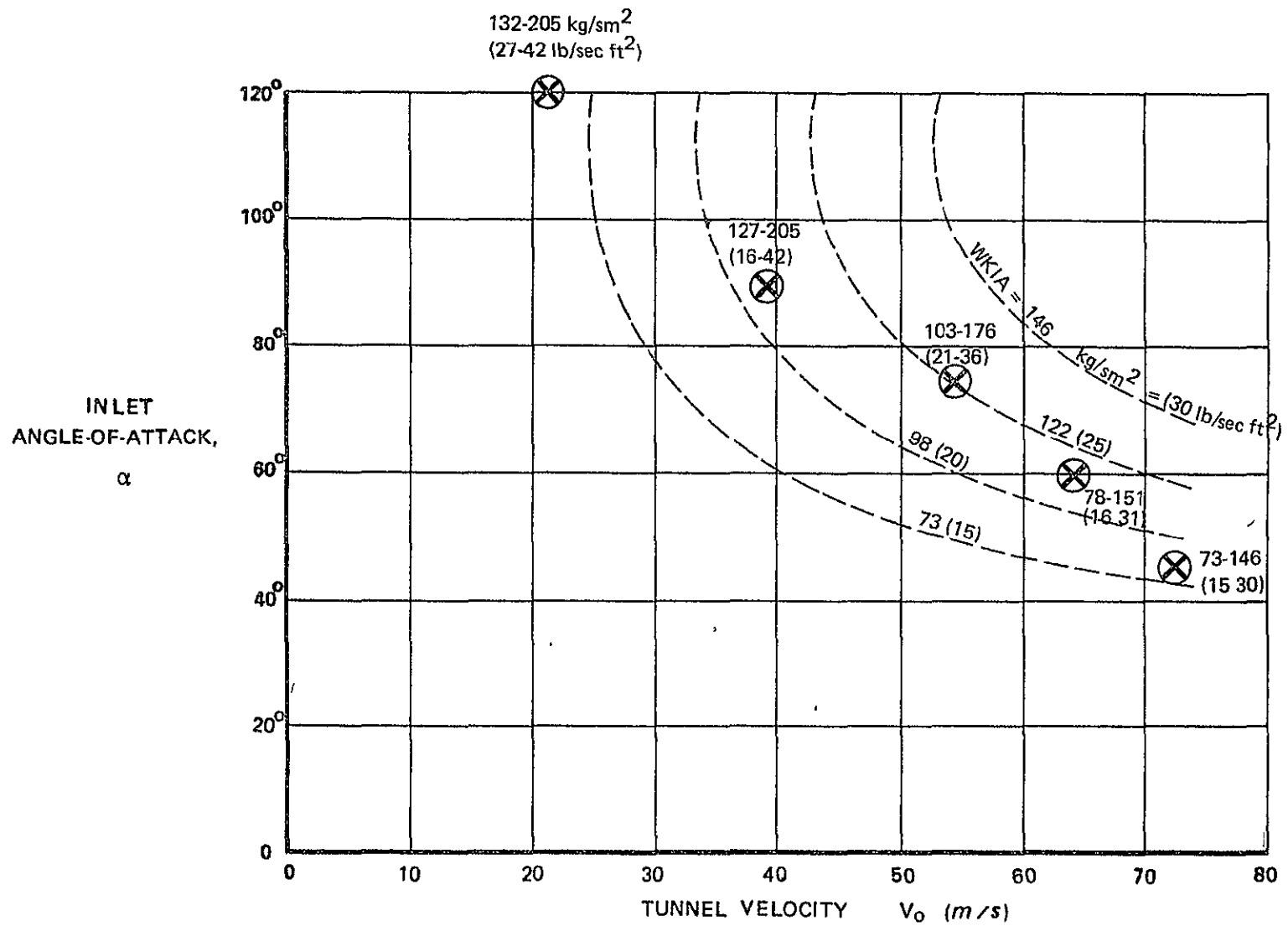


Figure 43 Large Scale Inlet Separation Boundaries and Design Conditions

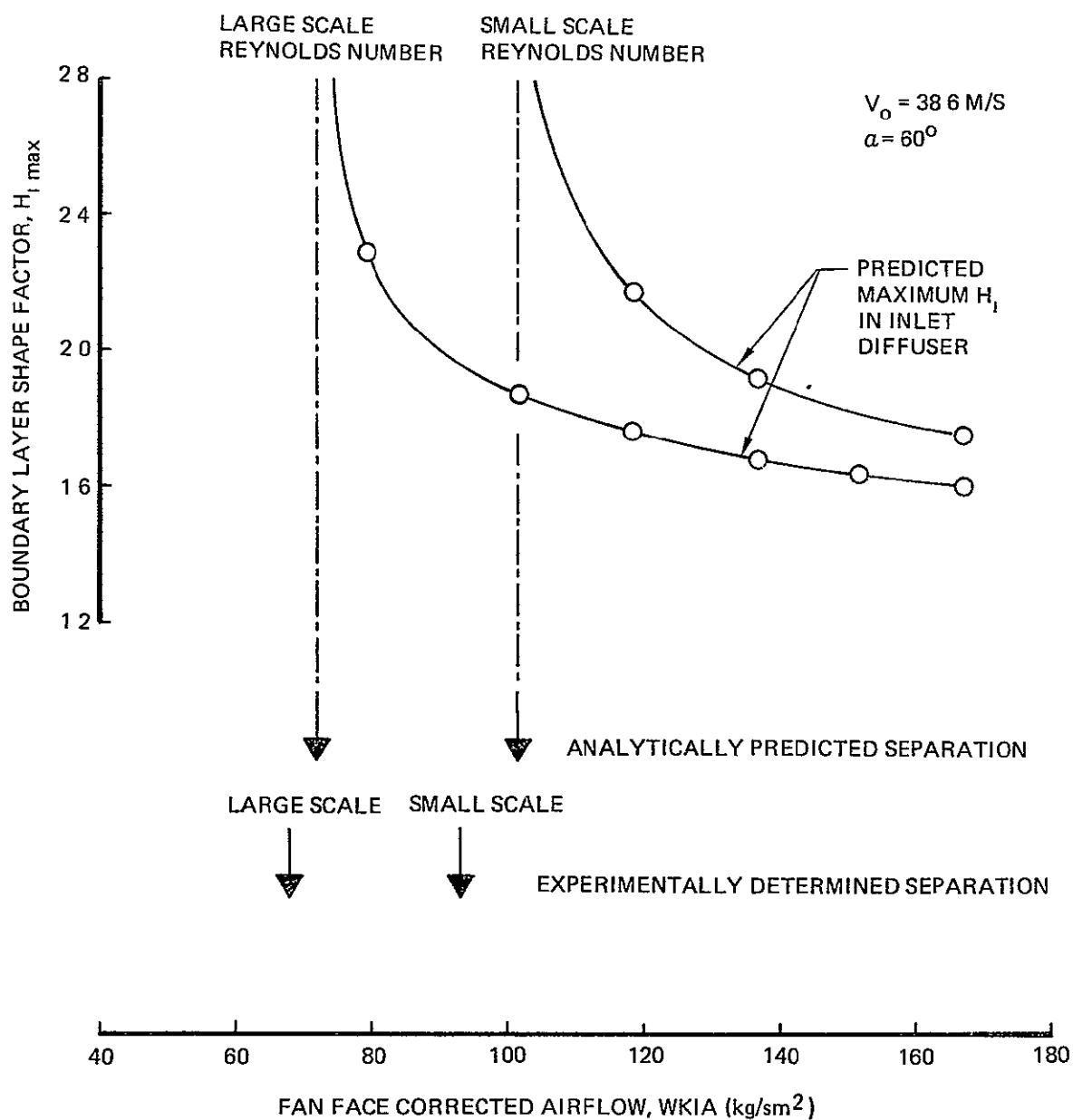


Figure 44 Experimental and Analytically Predicted Separation Points for Small and Large Scale Inlets

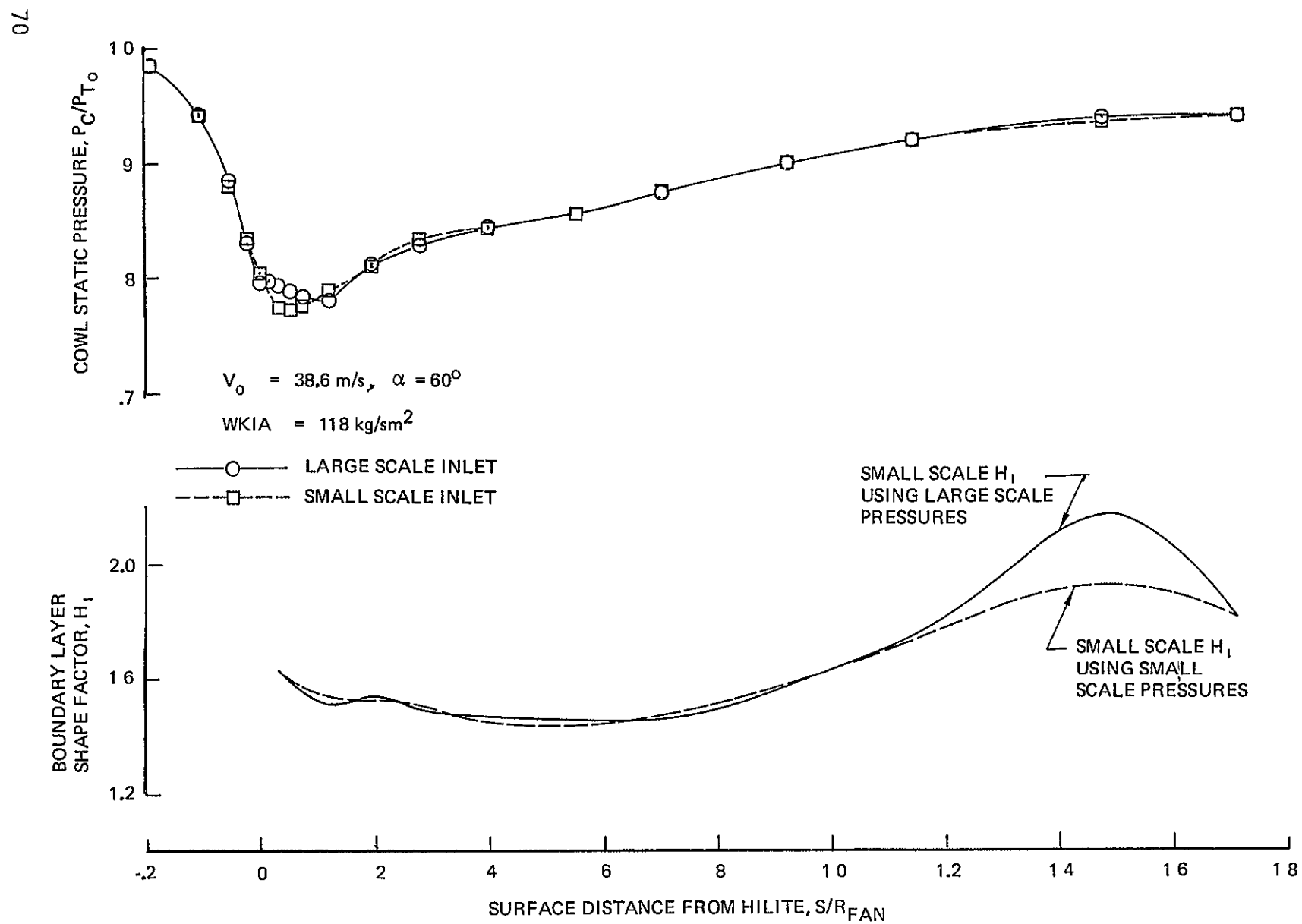


Figure 45 Comparison of Experimental Static Pressure Profiles and Computed  $H_1$  Profiles

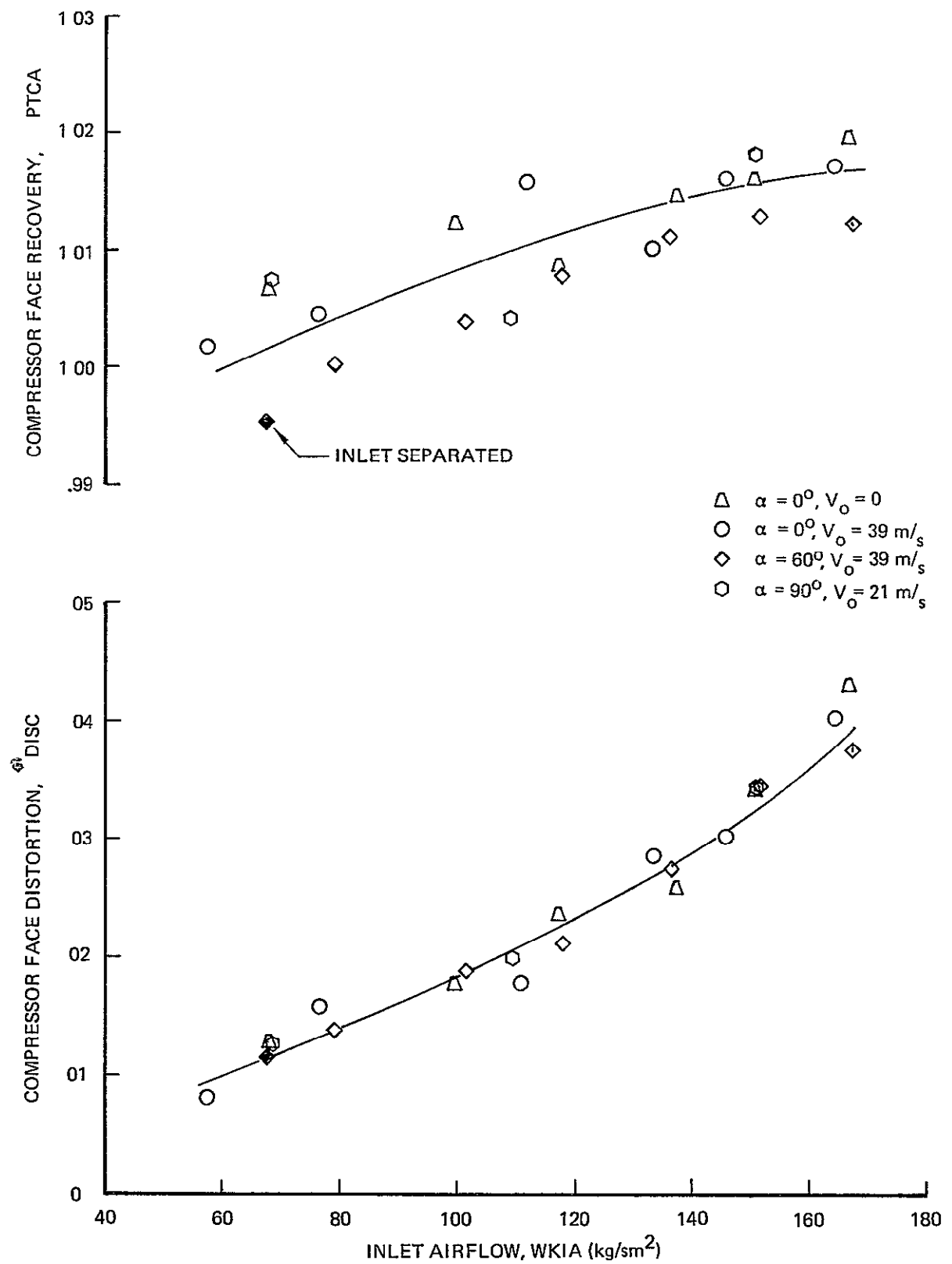


Figure 46 Core Engine Compressor Face Performance

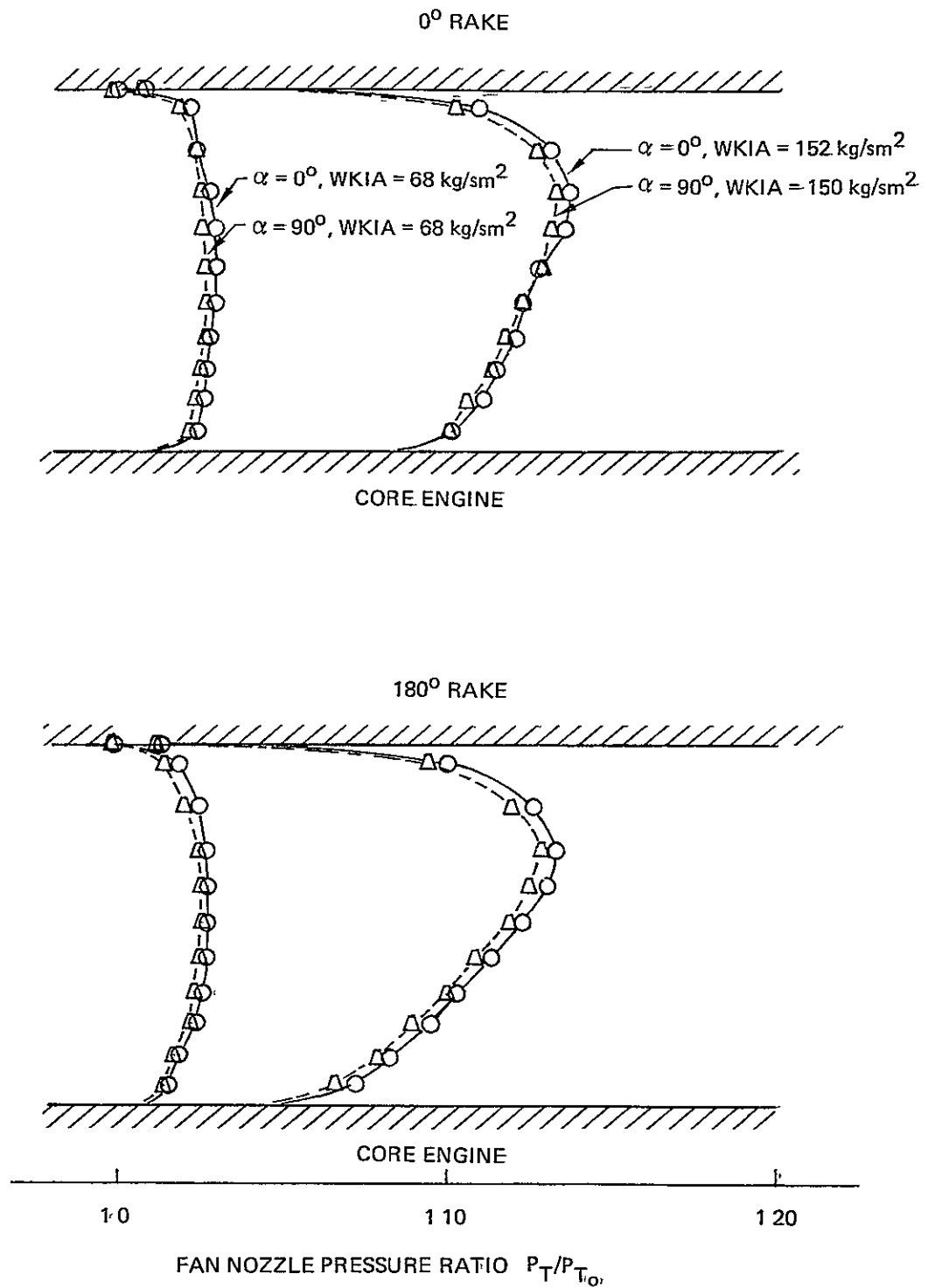


Figure 47 Fan Nozzle Total Pressure Profiles,  $V_0 = 21$  m/s,  $\alpha = 0^\circ$  and  $90^\circ$

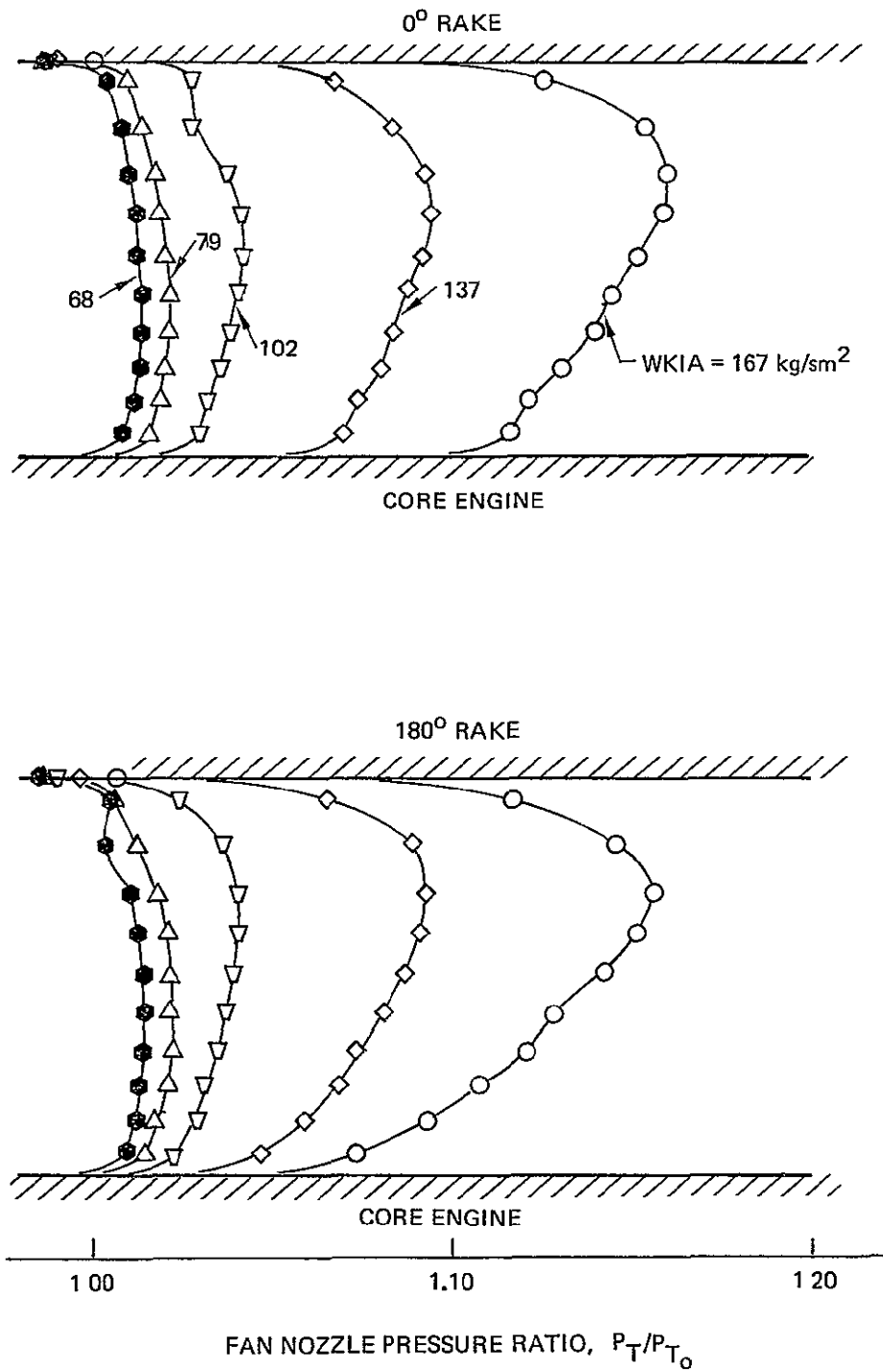


Figure 48 Fan Nozzle Total Pressure Profiles,  $V_0 = 39 \text{ m/s}$ ,  $\alpha = 60^\circ$

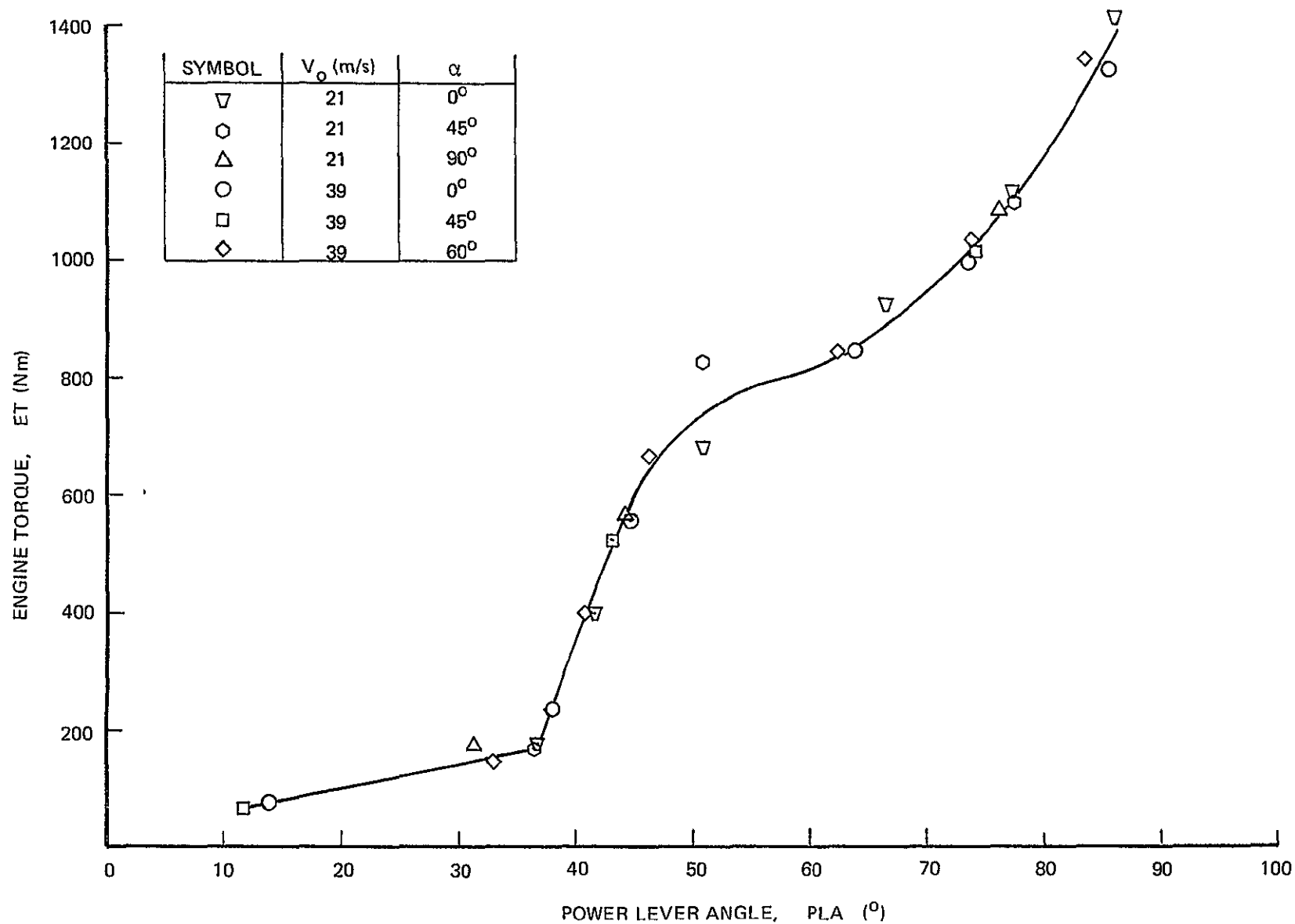


Figure 49 Engine Torque vs Power Lever Angle



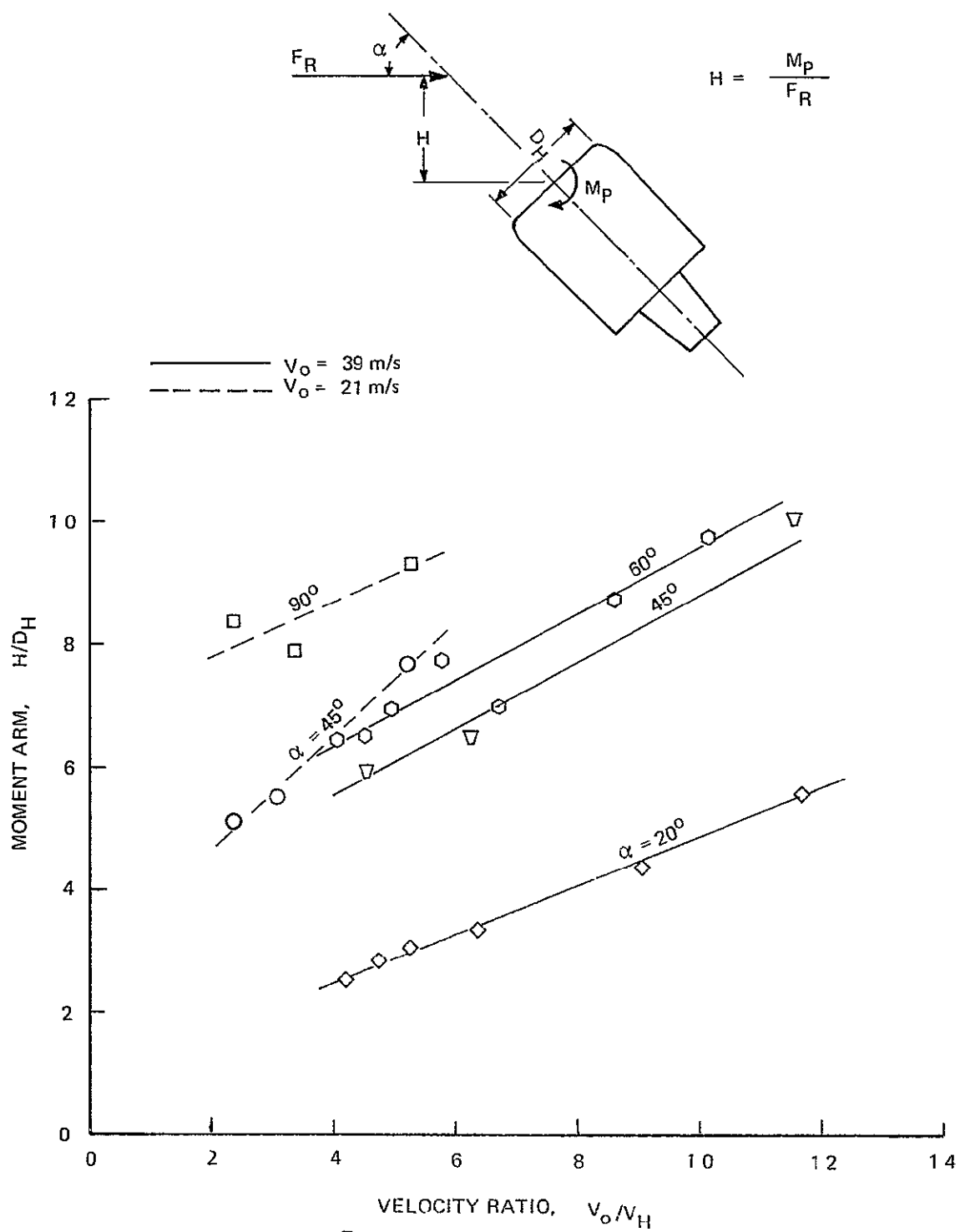


Figure 50 Nacelle Pitching Moment